ADVANCED MAGNETIC RESONANCE IMAGING OF EXTRACELLULAR VOLUME FOR GUIDING LEFT VENTRICULAR ASSIST DEVICE THERAPY

by

KyungPyo Hong

A dissertation submitted to the faculty of
The University of Utah
in partial fulfillment of the requirements for the degree of

Doctor of Philosophy

Department of Bioengineering

The University of Utah

December 2016

The University of Utah Graduate School

STATEMENT OF DISSERTATION APPROVAL

The dissertation of **KyungPyo Hong**

has been approved by the following supervisory committee members:

Daniel Kim	, Chair	**08/04/2016** Date Approved
Orly Alter	, Member	**09/08/2016** Date Approved
Edward Victor Rebok DiBella	, Member	**08/04/2016** Date Approved
Edward W. Hsu	, Member	**08/04/2016** Date Approved
Evgueni Gennadiy Kholmovski	, Member	**08/04/2016** Date Approved
Robert S. MacLeod	, Member	**08/04/2016** Date Approved

and by **Patrick A. Tresco** , Chair/Dean of

the Department/College/School of **Bioengineering**

and by David B. Kieda, Dean of The Graduate School.

ABSTRACT

Heart failure (HF) is a significant health care problem in the United States. Many patients advance towards end stage HF despite optimal medical therapy. For patients with end stage HF, unfortunately, therapeutic options are limited. While heart transplantation is the most proven treatment for improving survival, it is only performed in approximately 2,500 cases annually due to a shortage of donor hearts. Left ventricular assist device (LVAD) implantation is an FDA-approved therapy and is clinically indicated for two applications: (i) bridge-to-transplantation (BTT) for patients who are awaiting heart transplantation and (ii) destination therapy (DT) for patients who are ineligible for heart transplantation. Unexpectedly, patients in BTT and DT experience cardiac functional recovery after LVAD-induced unloading, which led to an investigational concept called bridge-to-recovery (BTR). For successful clinical translation, it is important to identify reliable predictors and discriminate responders from non-responders. Myocardial fibrosis, as a marker of adverse structural remodeling, is a proven predictor of poor outcomes. Cardiac magnetic resonance (CMR) is a proven and safe imaging modality for non-invasive assessment of myocardial fibrosis. Particularly, cardiac T_1 mapping has been widely used for assessment of diffuse myocardial fibrosis. However, current cardiac T_1 mapping techniques are unlikely to produce accurate results in LVAD candidates due to three obstacles: arrhythmia, limited breath-hold capacity, and implantable defibrillators. In response, this dissertation describes the development of new

cardiac T_1 mapping methods that overcome these obstacles. To overcome arrhythmia and limited breath-hold capacity, we developed a new arrhythmia-insensitive-rapid (AIR) cardiac T_1 mapping pulse sequence using a robust saturation radio-frequency (RF) pulse that is inherently insensitive to arrhythmia. We also made the AIR pulse sequence rapid by acquiring only one proton-density and one T_1-weighted image within a short breath-hold duration of only 2-3 heartbeats. To overcome the challenge of suppressing image artifacts induced by implantable defibrillators, we developed a new wideband AIR cardiac T_1 mapping pulse sequence by incorporating a new saturation RF pulse that extends the frequency bandwidth to off-resonant spins induced by defibrillators. The AIR and wideband AIR pulse sequences are validated extensively through in vitro and in vivo experiments.

TABLE OF CONTENTS

LIST OF TABLES

LIST OF FIGURES

LIST OF ACRONYMS

2-Ch: 2-chamber

2D: 2 dimension

3D: 3 dimension

4-Ch: 4-chamber

ACCF: American College of Cardiology Foundation

AFib: atrial fibrillation

AHA: American Heart Association

AIR: arrhythmia insensitive rapid

b-SSFP: balanced steady-state free precession

BTR: bridge-to-recovery

BTT: bridge-to-transplantation

BW: bandwidth

CMR: cardiac magnetic resonance

CRT: cardiac resynchronization therapy

DT: destination therapy

ECG: electrocardiogram

ECV: extracellular volume fraction

EF: ejection fraction

FA: flip angle

FID: free-induction decay

FLASH: fast low angle short

FOV: field of view

GBCA: gadolinium-based contrast agent

Gd: gadolinium

GRAPPA: generalized autocalibrating partially parallel acquisitions

GRE: gradient echo

HF: heart failure

ICD: implantable cardioverter defibrillator

INTERMACS: the Interagency Registry for Mechanically Assisted Circulatory Support

IR: inversion recovery

LAX: long axis

LGE: late gadolinium enhancement

LV: left ventricle

LVAD: left ventricular assist device

LVEF: left ventricular ejection fraction

$\mathbf{M_0}$: thermal equilibrium state of magnetization

MOLLI: modified Look-Locker inversion recovery

MR: magnetic resonance

MRI: magnetic resonance imaging

$\mathbf{M_z}$: magnetization

NIH: National Institutes of Health

NMR: nuclear magnetic resonance

PD: proton density

R_1: longitudinal relaxation rate

RF: radio frequency

ROI: region of interest

SAX: short axis

SR: saturation recovery

T_1: longitudinal relaxation time

T_{1w}: T_1-weighted

TD: delay time

TE: echo time

TI: inversion time

TR: repetition time

ACKNOWLEDGEMENTS

I would like to greatly thank my advisor, Dr. Daniel Kim, for his patient and thoughtful advice that enabled me to complete the long journey towards my doctoral degree. My invaluable experience, knowledge, and technical ability accumulated under his supervision will form the basis and driving force behind my growth as an independent scientist. I would also like to thank my committee members, Drs. Orly Alter, Edward V. R. DiBella, Edward W. Hsu, Evgueni G. Kholmovski, and Rob S. MacLeod, for advising me about my research and helping me to finish my doctoral degree.

I cannot help but to express a big thank you to my family. My mother and two brothers with their families have always supported me and taken an interest in my life and studies in the U.S.A. Furthermore, I would like to thank my classmate and lab-mate, Christopher Conlin, for paying kind attention to the miscellaneous issues that arose during my doctoral studies. Finally, I would like to thank all colleagues and friends not mentioned above for their invaluable help.

CHAPTER 1

INTRODUCTION

This chapter describes background on heart failure and treatment options, imaging biomarkers and magnetic resonance imaging, and the objective of this dissertation. It concludes with an overview of the entire dissertation.

1.1 Heart Failure

1.1.1 What is heart failure?

Heart failure (HF) is a clinical syndrome that describes structural and/or functional ventricular impairments, resulting in poor blood circulation through the body. Various etiologies can lead to HF, including hypertensive ventricular hypertrophy, arrhythmia, cardiomyopathy, valvular disease, pulmonary hypertension, and/or etc. The common symptoms of HF include shortness of breath, chronic coughing, fatigue, nausea, increased heart rate, and swelling in the legs and abdomen. Unfortunately, no cure exists for HF. As a consequence, the National Institutes of Health (NIH) and American Heart Association (AHA) recommend life style changes, medicines, and medical procedures that focus on halting the worsening of symptoms.

1.1.2 Prevalence and economics of HF in the US

Approximately 5.7 million Americans are struggling with HF (1-9), where approximately 1 million HF patients are admitted to hospitals at the cost of $17.5 billion annually (10). Re-hospitalization rate within 30 to 90 days post-discharge is 15% to 50%, respectively (11,12). Absolute mortality rate is as high as 50% within 5 years after first hospitalization (13). Furthermore, patients who do not respond to advanced medical treatments progress towards end-stage HF and have 1-year mortality rates as high as 48% (14). The total cost for HF care will increase to $69.7 billion by 2030 (8).

1.1.3 Classification and treatment of HF

According to the 2013 ACCF/AHA guideline (13), HF can be classified into four stages (i.e., stage A, B, C, and D) with progressively worst symptoms as summarized in Table 1.1. Particularly, patients who are determined to implant a left ventricular assist device (LVAD) are classified as stage D. This dissertation mainly focuses on stage D HF.

1.1.4 End-stage HF

End-stage HF (i.e., stage D, advanced, or refractory heart failure) is described as a persistent deterioration of cardiac function despite maximal medical treatment. Patients with end-stage HF also suffer from various symptoms, including fatigue, dyspnea, and nausea, even at rest. They have limited treatment options: heart transplantation, LVAD implantation, and experimental surgery for active treatment, and palliative care and hospice for end-of-life care. For the active treatment, heart transplantation is the gold standard for improving the quality of life and mortality, but it does not meet the needs of

all patients due to a lack of donor hearts. Approximately 2,500 heart transplantations are performed annually in the US (15). As an alternative, LVAD implantation is clinically indicated for bridge-to-transplantation (temporary) and destination (permanent) therapy. LVAD has been shown to improve survival in this cohort of patients (16). Despite its high cost (17), LVAD therapy is emerging as an adjunct treatment to heart transplantation. Experimental surgery (including those with stem cell delivery) is investigational at present. For palliative care, patients will decide on how to balance pain management and survival. This dissertation, particularly, will focus on LVAD therapy.

1.1.5 LVAD implantation

LVAD is a mechanical pump to help blood circulation by propelling blood from the left ventricle directly to the aorta (see Figure 1.1). LVAD implantation is an FDA-approved therapy and clinically indicated for two applications: i) bridge-to-transplantation (BTT) for patients who are awaiting heart transplantation, and ii) destination therapy (DT) for patients who are ineligible for heart transplantation. The development of this therapy has progressed over decades and is widely accepted as a clinical treatment option (13,18).

1.1.6 LVAD for bridge-to-recovery

Remarkably, patients in BTT and DT experience myocardial functional recovery after LVAD-induced mechanical unloading. This unexpected discovery has led to an investigational concept called bridge-to-recovery (BTR). In the latest INTERMACS registry which was designed for BTT and DT (not BTR), myocardial functional recovery

rate was reported as approximately 1% (19). On the other hand, Dr. Stavros Drakos' prospective evaluation of 77 non-ischemic cardiomyopathy patients in BTT or DT at the University of Utah indicates a much higher recovery rate (~21%) than INTERMACS report. The discrepancy between these results may derive from inconsistent measures. Nevertheless, there are no measurable predictors for identifying patients who will respond to BTR, although possible candidates have been suggested, including age, history of HF, etiology, and myocardial fibrosis (20). Of these, myocardial fibrosis is a promising predictor to discriminate responders from non-responders. This dissertation will seek to develop a new cardiac MRI method for assessment of myocardial fibrosis in patients who are scheduled for LVAD implantation (i.e., LVAD candidates). For successful clinical translation, this may be an important first step towards testing whether pre-existing myocardial fibrosis predicts poor outcome following LVAD implantation.

1.2 Imaging Biomarkers

1.2.1 Left ventricular ejection fraction

Left ventricular ejection fraction (LVEF) is an important functional measurement in cardiovascular medicine to discriminate HF from other heart diseases and is widely used for classification of heart failure. Despite its importance in cardiology, LVEF may be a poor predictor of outcomes.

1.2.2 Diffuse myocardial fibrosis

Myocardial fibrosis is an emerging biomarker of adverse structural remodeling in various heart diseases. Fibrosis is formed by the excessive deposition of fibrous

extracellular matrix and is related to tissue stiffness. Increased myocardial fibrosis impedes myocardial contraction and relaxation and eventually deteriorates the pumping ability of the heart. Focal myocardial fibrosis (i.e., myocardial infarct or scar) is typically caused by ischemic heart disease such as coronary artery disease (21), whereas diffuse myocardial fibrosis associated with the expansion of extracellular matrix (i.e., myocardial interstitial fibrosis) results from various non-ischemic insults (22-26). Aging also affects the development of diffuse myocardial fibrosis (27).

1.3 Tests for Measuring Myocardial Fibrosis

1.3.1 Myocardial biopsy

Myocardial biopsy is the gold standard method for direct assessment of myocardial fibrosis. The procedure is performed invasively by sampling endomyocardial tissues through either the internal jugular vein or femoral artery to access the right or left ventricles, respectively (28). However, endomyocardial biopsy is rarely indicated for clinical purpose, because it is invasive, sensitive to sampling errors, and has complication risks.

1.3.2 Blood analysis

Many molecules in blood serum or plasma have been proposed as biomarkers for the quantification of myocardial fibrosis; for example, serum carboxy-terminal telopeptide of procollagen type I, amino-terminal propeptide of procollagen type III, MMP-1, -2, and -9, and TIMP-1 (29). Although these biomarkers are likely useful for the assessment of myocardial fibrosis through blood sampling, most of them provide insufficient

information and are weakly associated with histology (30).

1.3.3 Imaging modalities for direct and indirect assessment of myocardial fibrosis

Various imaging modalities have been introduced for non-invasive assessment of myocardial fibrosis, including echocardiography and magnetic resonance imaging. Echocardiography can indirectly measure myocardial fibrosis by measuring acoustic properties and tissue deformation. Because myocardial collagen changes ultrasound scattering and attenuation, the measurement of peak and cyclic backscatter variation may reflect the degree of myocardial fibrosis. Alternatively, because myocardial strain is related to collagen deposition, the measurement of tissue Doppler (31) or speckling tracking (32) may indirectly represent the degree of myocardial fibrosis. In summary, echocardiography is capable of measuring some metrics that indirectly reflect myocardial fibrosis.

Magnetic resonance imaging is emerging as a promising modality for direct assessment of myocardial fibrosis. Indeed, it is a hot topic of basic and clinical research. More details are explained in the next section.

1.4 Cardiac MRI

Cardiac magnetic resonance (CMR) is a proven and safe imaging modality for non-invasively characterizing myocardial fibrosis with advanced techniques such as late gadolinium enhancement (LGE)(33), cardiac T_1 (longitudinal relaxation time of magnetization) mapping (34), and extracellular volume (ECV) fraction calculation (35). Leveraging these advantages, various pre-clinical and clinical studies have been

performed to validate CMR against histology (33,36-45).

1.4.1 LGE imaging

LGE imaging is the gold standard method for non-invasive assessment of focal myocardial viability in ischemic cardiomyopathy and is based on gadolinium-based contrast agent (GBCA) kinetic differences between infarcted (i.e., focal fibrosis) and normal myocardium (21,33). Fibrosis has a slower wash-in/out rate of fluid than normal tissues, thus allowing for higher accumulation of contrast agent at delayed imaging time. This difference in contrast agent concentration can be exploited to create a signal contrast between focal fibrosis (bright) and normal myocardium (dark) with T_1-weighting. However, LGE is ineffective for imaging diffuse myocardial fibrosis, because normal and fibrous tissues are distributed spatially (refer to Chapter 2).

1.4.2 Cardiac T_1 mapping and ECV

Cardiac T_1 mapping and ECV calculation from myocardial and blood T_1 values are emerging as alternatives for the absolute quantification of diffuse myocardial fibrosis, where physiological and structural changes in tissue are correspondingly reflected in changes of T_1. Post-contrast cardiac T_1 mapping technique can directly assess diffuse myocardial fibrosis after administration of GBCA, and the results are highly correlated with histology (26,37). Nevertheless, the reliability of post-contrast cardiac T_1 mapping itself is controversial due to its sensitivity to a variety of confounding factors including contrast agent type and dosage, acquisition timing, renal function, hematocrit, and magnetic field strength. To address these confounding factors, ECV calculation from pre-

and post-contrast myocardial and blood T_1 values has been suggested as a robust MR surrogate for diffuse myocardial fibrosis (35). However, studies investigating cardiac T_1 mapping against ECV calculation are largely lacking (34,46). While ECV has been validated as a measure of myocardial fibrosis against histology (40,47,48), it should be noted that ECV may be confounded by the presence of edema because it is a measure of extracellular volume. For example, in patients with acute myocarditis, ECV will reflect both edema and fibrosis.

1.4.3 CMR in LVAD candidates

A variety of different cardiac T_1 mapping techniques are currently available for non-invasive assessment of diffuse myocardial fibrosis (49-54). Of these, Modified Look-Locker Inversion recovery (MOLLI) is the most widely used investigational cardiac T_1 mapping technique, which uses inversion recovery (IR) radio-frequency (RF) pulses for multiple acquisitions of various T_1-weighted images during a breath-hold of 17 heartbeats (49). However, the accuracy of the MOLLI, as well as other investigational cardiac T_1 mapping pulse sequences, will be unreliable in LVAD candidates due to these obstacles:

(a) Irregular heartbeats (arrhythmia): MOLLI cardiac T_1 mapping is designed for regular heart rhythm and normal heart rate. Synchronized with electrocardiogram, MOLLI acquires multiple T_1-weighted images at various inversion times (TI) after each of three inversion RF pulses. To maintain consistent initial inversion magnetizations, IR RF pulses must be applied after achieving full recovery of magnetization (i.e., thermal equilibrium). In irregular rhythm, however, magnetization recovery is irregular and impacts T_1 quantification which assumes regular intervals of magnetization recovery.

(b) Limited breath-hold capacity: A pixel-by-pixel high-resolution T_1 map is calculated by curve-fitting of each pixel along the TI dimension to the Bloch equation (refer to Chapter 2). Thus, image registration is an important factor for data fidelity. Patients with end-stage HF may have difficulty in holding their breath for 17 heartbeats. This will result in image misregistration and consequently T_1 miscalculation.

(c) Implantable defibrillator (e.g., implantable cardioverter defibrillator (ICD) and/or cardiac resynchronization therapy (CRT)): Many patients with end-stage HF have an implantable defibrillator as either primary or secondary prevention of sudden cardiac death. Although clinical CMR can be performed safely in the presence of an implantable defibrillator in a 1.5 T MR system (55), most patients do not undergo CMR due to significant image artifacts induced by the defibrillator. Image artifacts are largely induced by the generator which shifts a center resonance frequency (i.e., off-resonance) as shown in Figure 1.2. A defibrillator will induce off-resonance on the order of 2-6 kHz, when it is placed 5-10 cm away from the heart: for example, large off-resonance occurs near the device (56). A conventional magnetization preparation RF pulse such as a hyperbolic adiabatic inversion pulse has a frequency bandwidth of approximately 1 kHz. In the presence of an implantable defibrillator, the inversion pulse cannot uniformly tip all spins, because some of the off-resonant spins (Δf) are out of the frequency bandwidth depending on the distance from the device (Figure 1.2B). We adopted the approach proposed by the UCLA group (56) and made our RF pulses wider in RF bandwidth, in order to uniformly tip the magnetization without regard to devices (Figure 1.2C).

1.5 Objective

This dissertation is aimed at developing new CMR T_1 mapping pulse sequences for assessment of diffuse myocardial fibrosis in patients who are scheduled for LVAD implantation, addressing three major obstacles for successful imaging: arrhythmia, limited breath-hold capacity, and implantable defibrillators.

1.6 Organization of the Dissertation

Chapter 2 provides the requisite background on magnetic resonance imaging for understanding the rest of this dissertation. Specifically, the measurement of longitudinal relaxation time (i.e., T_1 mapping) and the role of gadolinium-based contrast agents in CMR will be explained.

Chapter 3 describes a new arrhythmia-insensitive rapid (AIR) cardiac T_1 mapping pulse sequence, which also serves as the framework for wideband cardiac T_1 mapping pulse sequence (Chapter 6). The performance of the sequence is evaluated in phantom, human, and animal experiments with various heart rhythm and rate conditions.

Chapter 4 validates the AIR cardiac T_1 mapping pulse sequence against histology in a longitudinal canine study. Particularly, post-contrast myocardial T_1 and ECV measurements are acquired in canines to investigate which metric is more strongly correlated with histological quantification of diffuse myocardial fibrosis.

Chapter 5 compares the AIR cardiac T_1 mapping pulse sequence against MOLLI in a cross-sectional canine study. T_1 and ECV measurements acquired by these methods are compared to investigate any systematic differences between them.

Chapter 6 describes a new wideband AIR cardiac T_1 mapping pulse sequence for

assessment of myocardial fibrosis in patients with an implantable defibrillator. As a follow-up, this new method is preliminarily tested in subjects implanted with a device.

Chapter 7 summarizes this dissertation and provides suggestions on future directions.

1.7 References

1. Kochanek KD, Xu J, Murphy SL, Minino AM, Kung HC. Deaths: preliminary data for 2009. Natl Vital Stat Rep 2011;59(4):1-51.

2. Heron M. Deaths: leading causes for 2009. Natl Vital Stat Rep 2012;61(7):1-94.

3. Murphy SL, Xu J, Kochanek KD. Deaths: preliminary data for 2010. Natl Vital Stat Rep 2012;60(4).

4. Hoyert DL, Xu J. Deaths: preliminary data for 2011. Natl Vital Stat Rep 2012;61(6):1-51.

5. Xu J, Kochanek KD, Murphy SL, Arias E. Mortality in the United States, 2012. NCHS data brief 2014(168):1-8.

6. Kochanek KD, Murphy SL, Xu J, Arias E. Mortality in the United States, 2013. NCHS data brief 2014(178):1-8.

7. Go AS, Mozaffarian D, Roger VL, Benjamin EJ, Berry JD, Borden WB, Bravata DM, Dai S, Ford ES, Fox CS, Franco S, Fullerton HJ, Gillespie C, Hailpern SM, Heit JA, Howard VJ, Huffman MD, Kissela BM, Kittner SJ, Lackland DT, Lichtman JH, Lisabeth LD, Magid D, Marcus GM, Marelli A, Matchar DB, McGuire DK, Mohler ER, Moy CS, Mussolino ME, Nichol G, Paynter NP, Schreiner PJ, Sorlie PD, Stein J, Turan TN, Virani SS, Wong ND, Woo D, Turner MB. Heart disease and stroke statistics--2013 update: a report from the American Heart Association. Circulation 2013;127(1):e6-e245.

8. Go AS, Mozaffarian D, Roger VL, Benjamin EJ, Berry JD, Blaha MJ, Dai S, Ford ES, Fox CS, Franco S, Fullerton HJ, Gillespie C, Hailpern SM, Heit JA, Howard VJ, Huffman MD, Judd SE, Kissela BM, Kittner SJ, Lackland DT, Lichtman JH, Lisabeth LD, Mackey RH, Magid DJ, Marcus GM, Marelli A, Matchar DB, McGuire DK, Mohler ER, 3rd, Moy CS, Mussolino ME, Neumar RW, Nichol G, Pandey DK, Paynter NP, Reeves MJ, Sorlie PD, Stein J, Towfighi A, Turan TN, Virani SS, Wong ND, Woo D, Turner MB. Heart disease and stroke statistics--2014 update: a report from the American Heart Association. Circulation 2014;129(3):e28-e292.

9. Mozaffarian D, Benjamin EJ, Go AS, Arnett DK, Blaha MJ, Cushman M, de Ferranti S, Despres JP, Fullerton HJ, Howard VJ, Huffman MD, Judd SE, Kissela BM, Lackland DT, Lichtman JH, Lisabeth LD, Liu S, Mackey RH, Matchar DB, McGuire DK, Mohler ER, 3rd, Moy CS, Muntner P, Mussolino ME, Nasir K, Neumar RW, Nichol G, Palaniappan L, Pandey DK, Reeves MJ, Rodriguez CJ, Sorlie PD, Stein J, Towfighi A, Turan TN, Virani SS, Willey JZ, Woo D, Yeh RW, Turner MB. Heart disease and stroke statistics--2015 update: a report from the American Heart Association. Circulation 2015;131(4):e29-322.

10. Gheorghiade M, Vaduganathan M, Fonarow GC, Bonow RO. Rehospitalization for heart failure: problems and perspectives. J Am Coll Cardiol 2013;61(4):391-403.

11. Gheorghiade M, Pang PS. Acute heart failure syndromes. J Am Coll Cardiol 2009;53(7):557-573.

12. Butler J, Fonarow GC, Gheorghiade M. Strategies and opportunities for drug development in heart failure. JAMA 2013;309(15):1593-1594.

13. Yancy CW, Jessup M, Bozkurt B, Butler J, Casey DE, Jr., Drazner MH, Fonarow GC, Geraci SA, Horwich T, Januzzi JL, Johnson MR, Kasper EK, Levy WC, Masoudi FA, McBride PE, McMurray JJ, Mitchell JE, Peterson PN, Riegel B, Sam F, Stevenson LW, Tang WH, Tsai EJ, Wilkoff BL. 2013 ACCF/AHA guideline for the management of heart failure: a report of the American College of Cardiology Foundation/American Heart Association Task Force on Practice Guidelines. J Am Coll Cardiol 2013;62(16):e147-239.

14. Lietz K, Long JW, Kfoury AG, Slaughter MS, Silver MA, Milano CA, Rogers JG, Naka Y, Mancini D, Miller LW. Outcomes of left ventricular assist device implantation as destination therapy in the post-REMATCH era: implications for patient selection. Circulation 2007;116(5):497-505.

15. Taylor DO, Edwards LB, Aurora P, Christie JD, Dobbels F, Kirk R, Rahmel AO, Kucheryavaya AY, Hertz MI. Registry of the International Society for Heart and Lung Transplantation: twenty-fifth official adult heart transplant report--2008. J Heart Lung Transplant 2008;27(9):943-956.

16. Stewart GC, Givertz MM. Mechanical circulatory support for advanced heart failure: patients and technology in evolution. Circulation 2012;125(10):1304-1315.

17. Digiorgi PL, Reel MS, Thornton B, Burton E, Naka Y, Oz MC. Heart transplant and left ventricular assist device costs. J Heart Lung Transplant 2005;24(2):200-204.

18. Rose EA, Gelijns AC, Moskowitz AJ, Heitjan DF, Stevenson LW, Dembitsky W, Long JW, Ascheim DD, Tierney AR, Levitan RG, Watson JT, Meier P, Ronan NS, Shapiro PA, Lazar RM, Miller LW, Gupta L, Frazier OH, Desvigne-Nickens P, Oz MC, Poirier VL. Long-term use of a left ventricular assist device for end-stage heart failure. N Engl J Med 2001;345(20):1435-1443.

19. Kirklin JK, Naftel DC, Pagani FD, Kormos RL, Stevenson LW, Blume ED, Miller MA, Baldwin JT, Young JB. Sixth INTERMACS annual report: a 10,000-patient database. J Heart Lung Transplant 2014;33(6):555-564.

20. Mano A, Nakatani T, Oda N, Kato T, Niwaya K, Tagusari O, Nakajima H, Funatsu T, Hashimoto S, Komamura K, Hanatani A, Ueda IH, Kitakaze M, Kobayashi J, Yagihara T, Kitamura S. Which factors predict the recovery of natural heart function after insertion of a left ventricular assist system? J Heart Lung Transplant 2008;27(8):869-874.

21. Kim RJ, Wu E, Rafael A, Chen EL, Parker MA, Simonetti O, Klocke FJ, Bonow RO, Judd RM. The use of contrast-enhanced magnetic resonance imaging to identify reversible myocardial dysfunction. N Engl J Med 2000;343(20):1445-1453.

22. Kellman P, Wilson JR, Xue H, Bandettini WP, Shanbhag SM, Druey KM, Ugander M, Arai AE. Extracellular volume fraction mapping in the myocardium, part 2: initial clinical experience. J Cardiovasc Magn Reson 2012;14:64.

23. Ellims AH, Iles LM, Ling L, Hare JL, Kaye DM, Taylor AJ. Diffuse myocardial fibrosis in hypertrophic cardiomyopathy can be identified by cardiovascular magnetic resonance, and is associated with left ventricular diastolic dysfunction. J Cardiovasc Magn Reson 2012;14(1):76.

24. aus dem Siepen F, Buss SJ, Messroghli D, Andre F, Lossnitzer D, Seitz S, Keller M, Schnabel PA, Giannitsis E, Korosoglou G, Katus HA, Steen H. T1 mapping in dilated cardiomyopathy with cardiac magnetic resonance: quantification of diffuse myocardial fibrosis and comparison with endomyocardial biopsy. European Heart Journal Cardiovascular Imaging 2015;16(2):210-216.

25. Flett AS, Sado DM, Quarta G, Mirabel M, Pellerin D, Herrey AS, Hausenloy DJ, Ariti C, Yap J, Kolvekar S, Taylor AM, Moon JC. Diffuse myocardial fibrosis in severe aortic stenosis: an equilibrium contrast cardiovascular magnetic resonance study. European Heart Journal Cardiovascular Imaging 2012;13(10):819-826.

26. Iles L, Pfluger H, Phrommintikul A, Cherayath J, Aksit P, Gupta SN, Kaye DM, Taylor AJ. Evaluation of diffuse myocardial fibrosis in heart failure with cardiac magnetic resonance contrast-enhanced T1 mapping. J Am Coll Cardiol 2008;52(19):1574-1580.

27. Liu CY, Liu YC, Wu C, Armstrong A, Volpe GJ, van der Geest RJ, Liu Y, Hundley WG, Gomes AS, Liu S, Nacif M, Bluemke DA, Lima JA. Evaluation of age-related interstitial myocardial fibrosis with cardiac magnetic resonance contrast-enhanced T1 mapping: MESA (Multi-Ethnic Study of Atherosclerosis). J Am Coll Cardiol 2013;62(14):1280-1287.

28. Cooper LT, Baughman KL, Feldman AM, Frustaci A, Jessup M, Kuhl U, Levine GN, Narula J, Starling RC, Towbin J, Virmani R. The role of endomyocardial biopsy in the management of cardiovascular disease: a scientific statement from the American Heart Association, the American College of Cardiology, and the European Society of Cardiology. Endorsed by the Heart Failure Society of America and the Heart Failure Association of the European Society of Cardiology. J Am Coll Cardiol 2007;50(19):1914-1931.

29. Leong DP, Madsen PL, Selvanayagam JB. Non-invasive evaluation of myocardial fibrosis: implications for the clinician. Heart 2010;96(24):2016-2024.

30. Lopez B, Gonzalez A, Ravassa S, Beaumont J, Moreno MU, San Jose G, Querejeta R, Diez J. Circulating biomarkers of myocardial fibrosis: the need for a reappraisal. J Am Coll Cardiol 2015;65(22):2449-2456.

31. Yu CM, Sanderson JE, Marwick TH, Oh JK. Tissue Doppler imaging a new prognosticator for cardiovascular diseases. J Am Coll Cardiol 2007;49(19):1903-1914.

32. Blessberger H, Binder T. NON-invasive imaging: Two dimensional speckle tracking echocardiography: basic principles. Heart 2010;96(9):716-722.

33. Kim RJ, Fieno DS, Parrish TB, Harris K, Chen EL, Simonetti O, Bundy J, Finn JP, Klocke FJ, Judd RM. Relationship of MRI delayed contrast enhancement to irreversible injury, infarct age, and contractile function. Circulation 1999;100(19):1992-2002.

34. Flett AS, Hayward MP, Ashworth MT, Hansen MS, Taylor AM, Elliott PM, McGregor C, Moon JC. Equilibrium contrast cardiovascular magnetic resonance for the measurement of diffuse myocardial fibrosis: preliminary validation in humans. Circulation 2010;122(2):138-144.

35. Ugander M, Oki AJ, Hsu LY, Kellman P, Greiser A, Aletras AH, Sibley CT, Chen MY, Bandettini WP, Arai AE. Extracellular volume imaging by magnetic resonance imaging provides insights into overt and sub-clinical myocardial pathology. Eur Heart J 2012;33(10):1268-1278.

36. Mahrholdt H, Goedecke C, Wagner A, Meinhardt G, Athanasiadis A, Vogelsberg H, Fritz P, Klingel K, Kandolf R, Sechtem U. Cardiovascular magnetic resonance

assessment of human myocarditis a comparison to histology and molecular pathology. Circulation 2004;109(10):1250-1258.

37. Sibley CT, Noureldin RA, Gai N, Nacif MS, Liu S, Turkbey EB, Mudd JO, van der Geest RJ, Lima JA, Halushka MK, Bluemke DA. T1 mapping in cardiomyopathy at cardiac MR: comparison with endomyocardial biopsy. Radiology 2012;265(3):724-732.

38. Bull S, White SK, Piechnik SK, Flett AS, Ferreira VM, Loudon M, Francis JM, Karamitsos TD, Prendergast BD, Robson MD. Human non-contrast T1 values and correlation with histology in diffuse fibrosis. Heart 2013:heartjnl-2012-303052.

39. Mavrogeni S, Spargias K, Markussis V, Kolovou G, Demerouti E, Papadopoulou E, Stavridis G, Kaklamanis L, Douskou M, Constantoulakis P. Myocardial inflammation in autoimmune diseases: investigation by cardiovascular magnetic resonance and endomyocardial biopsy. Inflammation & Allergy-Drug Targets 2009;8(5):390-397.

40. White SK, Sado DM, Fontana M, Banypersad SM, Maestrini V, Flett AS, Piechnik SK, Robson MD, Hausenloy DJ, Sheikh AM, Hawkins PN, Moon JC. T1 mapping for myocardial extracellular volume measurement by CMR: bolus only versus primed infusion technique. JACC Cardiovascular Imaging 2013;6(9):955-962.

41. Ibanez B, Prat-González S, Speidl WS, Vilahur G, Pinero A, Cimmino G, García MJ, Fuster V, Sanz J, Badimon JJ. Early metoprolol administration before coronary reperfusion results in increased myocardial salvage analysis of ischemic myocardium at risk using cardiac magnetic resonance. Circulation 2007;115(23):2909-2916.

42. Fontana M, White SK, Banypersad SM, Sado DM, Maestrini V, Flett AS, Piechnik SK, Neubauer S, Roberts N, Moon JC. Comparison of T1 mapping techniques for ECV quantification. Histological validation and reproducibility of ShMOLLI versus multibreath-hold T1 quantification equilibrium contrast CMR. J Cardiovasc Magn Reson 2012;14:88.

43. Chen J, Song S-K, Liu W, McLean M, Allen JS, Tan J, Wickline SA, Yu X. Remodeling of cardiac fiber structure after infarction in rats quantified with diffusion tensor MRI. American Journal of Physiology-Heart and Circulatory Physiology 2003;285(3):H946-H954.

44. Hoffmann U, Globits S, Schima W, Loewe C, Puig S, Oberhuber G, Frank H. Usefulness of magnetic resonance imaging of cardiac and paracardiac masses. The American Journal of Cardiology 2003;92(7):890-895.

45. Johnson GA, Cofer GP, Gewalt SL, Hedlund LW. Morphologic phenotyping with MR microscopy: the visible mouse 1. Radiology 2002;222(3):789-793.

46. Miller CA, Naish JH, Bishop P, Coutts G, Clark D, Zhao S, Ray SG, Yonan N, Williams SG, Flett AS, Moon JC, Greiser A, Parker GJ, Schmitt M. Comprehensive validation of cardiovascular magnetic resonance techniques for the assessment of myocardial extracellular volume. Circ Cardiovasc Imaging 2013;6(3):373-383.

47. Neilan TG, Coelho-Filho OR, Shah RV, Abbasi SA, Heydari B, Watanabe E, Chen Y, Mandry D, Pierre-Mongeon F, Blankstein R, Kwong RY, Jerosch-Herold M. Myocardial extracellular volume fraction from T1 measurements in healthy volunteers and mice: relationship to aging and cardiac dimensions. JACC Cardiovascular Imaging 2013;6(6):672-683.

48. Messroghli DR, Nordmeyer S, Dietrich T, Dirsch O, Kaschina E, Savvatis K, D Oh-I, Klein C, Berger F, Kuehne T. Assessment of diffuse myocardial fibrosis in rats using small-animal Look-Locker inversion recovery T1 mapping. Circ Cardiovasc Imaging 2011;4(6):636-640.

49. Messroghli DR, Radjenovic A, Kozerke S, Higgins DM, Sivananthan MU, Ridgway JP. Modified Look-Locker inversion recovery (MOLLI) for high-resolution T1 mapping of the heart. Magn Reson Med 2004;52(1):141-146.

50. Piechnik SK, Ferreira VM, Dall'Armellina E, Cochlin LE, Greiser A, Neubauer S, Robson MD. Shortened Modified Look-Locker Inversion recovery (ShMOLLI) for clinical myocardial T1-mapping at 1.5 and 3 T within a 9 heartbeat breathhold. J Cardiovasc Magn Reson 2010;12:69.

51. Song T, Stainsby JA, Ho VB, Hood MN, Slavin GS. Flexible cardiac T1 mapping using a modified Look-Locker acquisition with saturation recovery. Magn Reson Med 2012;67(3):622-627.

52. Slavin G, Stainsby J. True T1 mapping with SMART1Map (saturation method using adaptive recovery times for cardiac T1 mapping): a comparison with MOLLI. J Cardiovasc Magn Reson 2013;15(Suppl 1):P3.

53. Chow K, Flewitt JA, Green JD, Pagano JJ, Friedrich MG, Thompson RB. Saturation recovery single-shot acquisition (SASHA) for myocardial T(1) mapping. Magn Reson Med 2014;71(6):2082-2095.

54. Weingartner S, Akcakaya M, Basha T, Kissinger KV, Goddu B, Berg S, Manning WJ, Nezafat R. Combined saturation/inversion recovery sequences for improved evaluation of scar and diffuse fibrosis in patients with arrhythmia or heart rate variability. Magn Reson Med 2014;71(3):1024-1034.

55. Nazarian S, Roguin A, Zviman MM, Lardo AC, Dickfeld TL, Calkins H, Weiss RG, Berger RD, Bluemke DA, Halperin HR. Clinical utility and safety of a protocol for noncardiac and cardiac magnetic resonance imaging of patients with permanent pacemakers and implantable-cardioverter defibrillators at 1.5 tesla. Circulation 2006;114(12):1277-1284.

56. Rashid S, Rapacchi S, Vaseghi M, Tung R, Shivkumar K, Finn JP, Hu P. Improved late gadolinium enhancement MR imaging for patients with implanted cardiac devices. Radiology 2014;270(1):269-274.

Table 1.1. AHA classification of HF with treatments. Summarized from Yancy CW et al., *JACC* 2013. ICD, implantable cardioverter defibrillator; CRT, cardiac resynchronization therapy; LVAD, left ventricular assist device.

At risk for heart failure		Heart failure	
Stage A	**Stage B**	**Stage C**	**Stage D**
At high risk for HF but without structural heart disease or symptoms of HF	Structural heart disease but without signs or symptoms of HF	Structural heart disease with prior or current symptoms of HF	Refractory HF
▪ Drugs	▪ Drugs ▪ ICD ▪ Revascularization ▪ Valvular surgery	▪ Drugs ▪ CRT ▪ ICD ▪ Revascularization ▪ Valvular surgery	▪ Heart transplant ▪ LVAD ▪ Experimental surgery ▪ Palliative care and hospice

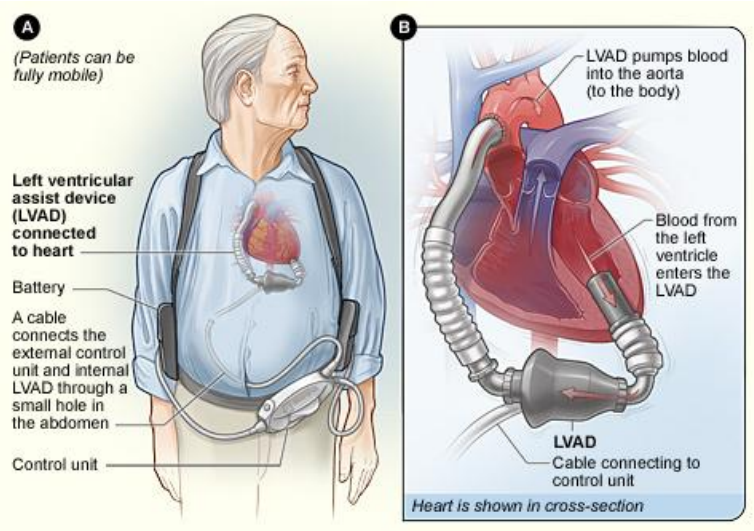

Figure 1.1 An example of LVAD installation in human. Picture from https://www.nhlbi.nih.gov/health/health-topics/topics/vad. Source: National Heart, Lung, and Blood Institute; National Institutes of Health; U.S. Department of Health and Human Services.

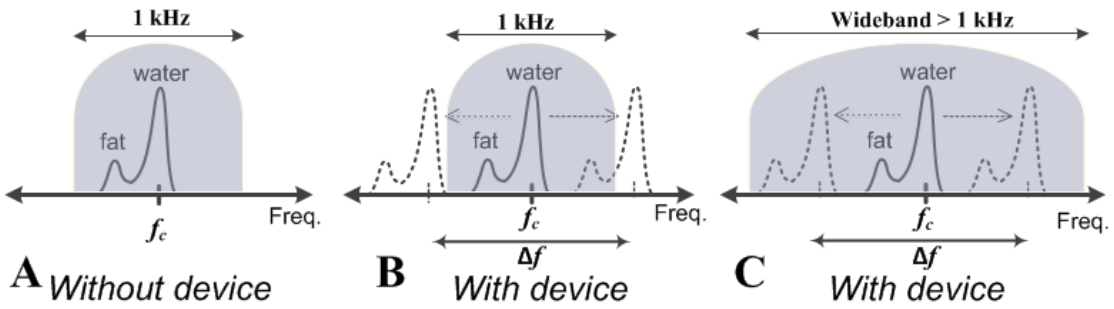

Figure 1.2. RF pulse coverage (gray dome) in the absence (A) and presence (B and C) of an implantable defibrillator. In the presence of a device, the degree of off-resonance (Δf) is inversely proportional to the distance from the device. Conventional RF pulse (1 kHz) cannot excite both on- and off-resonance of fat and water frequencies (B), whereas wideband RF pulse (> 1 kHz) can (C). f_c = center resonance frequency.

CHAPTER 2

BACKGROUND ON CARDIAC MRI

This chapter provides background on magnetic resonance imaging (MRI). For more details, the readers are referred to the literature.

2.1 Introduction

MRI is a safe imaging modality that is used routinely in clinical radiology. It is based on nuclear magnetic resonance (NMR) of nuclei placed in a static magnetic field. The main concept of MRI is to generate, manipulate, and detect the transverse magnetization of spins in the tissues of interest by encoding spatial information (i.e., spatial resonance frequency) and then reconstructing images through Fourier transformation of the detected signals.

2.2 Nuclear Magnetic Resonance

2.2.1 Nuclear spin

Spin is an angular momentum ($\vec{\boldsymbol{J}}$) observed in nuclei of atoms which have odd atomic weights and/or odd atomic numbers. A nucleus has a magnetic dipole moment ($\vec{\boldsymbol{\mu}}$) if it possesses a non-zero spin (e.g., ^{1}H, ^{13}C, ^{19}F, and ^{31}P). The relation between spin angular momentum and the magnetic dipole moment is expressed as $\vec{\boldsymbol{\mu}} = \gamma\vec{\boldsymbol{J}}$ where γ is the

gyromagnetic ratio. The magnitude of $\vec{\boldsymbol{\mu}}$ is $\gamma\hbar\sqrt{I(I+1)}$ where $\hbar$ is Plank's constant h ($6.6 \times 10^{-34}\ J \cdot s$) divided by 2π and I is the spin quantum number (e.g., $I = 1/2$ for ^{1}H, ^{13}C, ^{19}F, and ^{31}P). For this dissertation, proton (^{1}H) will be focused on, because the human and animal body are mostly made up of water (H_2O) and hydrocarbon compounds.

2.2.2 Magnetization in static magnetic field ($\overrightarrow{B_0}$)

Once spins are placed in a strong static magnetic field ($\overrightarrow{\boldsymbol{B_0}}$), they are aligned in the same direction as the magnetic field and expressed as magnetization ($\vec{\boldsymbol{M}}$) which is a vector field representing comprehensive spins: $\vec{\boldsymbol{M}} = \sum \vec{\boldsymbol{\mu}}$ (refer to Figure 2.1). In the magnetic field, the spins precess at a resonance frequency (ω_0) known as the Larmor frequency:

$$\omega_0 = \gamma B_0.$$

The gyromagnetic ratio (γ) is specified by the nuclei. For example, $\gamma/2\pi$ for the protons (^{1}H) is 42.58 MHz/T. Magnetization at the thermal equilibrium state in the magnetic field is expressed as:

$$\left|\vec{\boldsymbol{M}}\right| = \boldsymbol{M}_{z,0} = \boldsymbol{M}_0 = \frac{\gamma^2\hbar^2 B_0 N_s I(I+1)}{3kT_s}$$

where N_s is the total number of spins, T_s is absolute temperature, and k is Boltzmann's constant ($1.38 \times 10^{-23}\ J/K$). Practically, the magnitude of $M_{z,0}$ can be controlled by the strength of the magnetic field ($\overrightarrow{\boldsymbol{B_0}}$) and temperature ($T_s$).

2.2.3 Radio-frequency pulse

A radio-frequency (RF) pulse generates an RF field ($\overrightarrow{\boldsymbol{B_1}}$) to rotate the longitudinal magnetization onto the transverse plane for signal detection as illustrated in Figures 2.1 and 2.2. Its frequency is tuned to the resonance frequency of the spins (i.e., resonance condition, $\omega_{rf} = \omega_0$):

$$\overrightarrow{\boldsymbol{B_1}}(t) = B_1^e(t)e^{-i\omega_{rf}t}$$

where $B_1^e(t)$ is a pulse envelope function. A $\overrightarrow{\boldsymbol{B_1}}$ (transverse plane) is perpendicular to the $\overrightarrow{\boldsymbol{B_0}}$ (longitudinal). An RF pulse can be applied to spins with a certain flip angle (α) and at a certain location (see Section 2.3.1). Flip angle is determined by the duration (τ) and the magnitude of $\overrightarrow{\boldsymbol{B_1}}$: $\alpha = \int_0^\tau \gamma B_1^e(t)dt$. Therefore, the strength of an RF pulse (i.e., RF energy) is associated with both the magnitude of the $\overrightarrow{\boldsymbol{B_1}}$ and the duration of the RF pulse. Specific absorption rate (SAR) is a measure of energy deposition rate in the human body by an RF pulse and is an important factor of MR safety, in that RF energy transferred directly to a subject causes increasing temperature in the tissues. According to FDA guidelines, the normal SAR limit is less than 2.0 W/kg whole-body or a core temperature increase of 0.5 ˚C.

When no RF pulse is applied, magnetization is maintained at the thermal equilibrium state ($\overrightarrow{\boldsymbol{M}} = \overrightarrow{\boldsymbol{M_0}}$), and its direction is identical to that of $\overrightarrow{\boldsymbol{B_0}}$. Once an RF pulse is applied, the magnetization points to the other direction and begins to recover back to the initial state (or thermal equilibrium) while precessing at the Larmor frequency about $\overrightarrow{\boldsymbol{B_0}}$, which is called free-induction decay (FID)(see Figure 2.2).

2.2.4 RF transmitter/receiver coil

An RF coil is used as an antenna for both transmitting RF energy into a subject to stimulate spins and receiving/detecting MR signals from the excited spins. Particularly, based on Faraday's law of induction (i.e., electromagnetic induction), the recordable MR signals are generated mostly from the transverse magnetization relaxation (M_{xy}) of a FID.

2.2.5 Longitudinal relaxation time (T_1)

Longitudinal relaxation time (T_1) is a time constant describing the recovery rate of longitudinal magnetization (M_z) back to thermal equilibrium after the magnetization has been rotated onto the transverse plane. Because the time constant T_1 is highly associated with the surrounding environment (spin-lattice relaxation), tissues with different compositions have different T_1 values. The spin-lattice relaxation is explained by the energy exchange or dissipation between spins and their surroundings.

The Bloch equation (1) describes the longitudinal relaxation mechanism through mathematics (refer to Figure 2.3):

$$\frac{dM_z}{dt} = -\frac{M_z - M_{z,0}}{T_1}$$

$$\rightarrow \overrightarrow{\boldsymbol{M_z}}(t) = M_{z,0}\left(1 - e^{-t/T_1}\right) + \overrightarrow{\boldsymbol{M_z}}(0)e^{-t/T_1}$$

For example, when an inversion recovery (IR) RF pulse (magnetization is flipped by 180˚) is applied, $\overrightarrow{\boldsymbol{M_z}}(0)$ is $-M_{z,0}$ and $\overrightarrow{\boldsymbol{M_z}}(t)$ becomes $M_{z,0}\left(1 - 2 \times e^{-t/T_1}\right)$. On the other hand, when a saturation recovery (SR) RF pulse (magnetization is flipped by 90˚) is applied, $\overrightarrow{\boldsymbol{M_z}}(0)$ is 0 and $\overrightarrow{\boldsymbol{M_z}}(t)$ becomes $M_{z,0}\left(1 - e^{-t/T_1}\right)$. After one time constant (T_1),

$\overrightarrow{\boldsymbol{M_z}}$ after SR RF excitation recovers to 63% of the thermal equilibrium state, $M_{z,0}$.

2.2.6 Transverse relaxation time (T_2)

Transverse relaxation time (T_2) is a time constant describing the loss rate of phase coherence (spin-spin relaxation) of transverse magnetization ($\overrightarrow{\boldsymbol{M_{xy}}}$) after RF excitation. As mentioned in Section 2.2.4, the transverse magnetization is the recordable source of an MR signal, and its amplitude depends on the degree of coherence of isochromates. As spins are dephasing, the intensity of the transverse signal accordingly goes down (i.e., highest when in phase, lowest when out of phase). The time constant T_2 is largely independent of the strength of the magnetic field.

The Bloch equation also describes the transverse relaxation mechanism through mathematics (refer to Figure 2.3):

$$\frac{dM_{xy}}{dt} = -\frac{M_{xy}}{T_2}$$

$$\rightarrow \overrightarrow{\boldsymbol{M_{xy}}}(t) = \overrightarrow{\boldsymbol{M_{xy}}}(0)e^{-t/T_2}$$

After one time constant (T_2), $\overrightarrow{\boldsymbol{M_{xy}}}$ decays to 37% of $\overrightarrow{\boldsymbol{M_{xy}}}(0)$.

2.3 MR Imaging

Utilizing the fundamental properties of NMR phenomena, MR signals can be non-invasively detected from the inside of a living subject in a strong magnetic field. However, the reconstruction of a visible image from the detected signals is not simple, because there is no localizing information in the main magnetic field. For example, all spins in a spatially homogeneous subject precess at an identical Larmor frequency in a

homogenous magnetic field. After RF excitation of all spins, the detected MR signals have a single resonance frequency: i.e., it is impossible to distinguish where the signals came from. Thus, after the development of signal localization, MRI has been an invaluable technique for non-invasively exploring arbitrary cross-sections in living subjects.

2.3.1 Localization of MR signals

Localization is achieved by using a gradient field ($\vec{\boldsymbol{G}}$) generated by gradient coils (refer to Figure 2.1). For 3-dimensional localization, slice selection and spatial encoding (phase and frequency encoding) are performed. First, slice selection is determined by a linear gradient field with the bandwidth of a transmitting RF pulse. For example, a slice perpendicular to z-direction can be selected by a modified magnetic field with an extra gradient field: $\vec{\boldsymbol{B}}(z) = B_0 + G_z \times z$, where z is the location of the slice in z-direction and G_z is the magnitude of z-gradient field. Correspondingly, the resonance frequency in the slice is modified along z-direction: $\omega(z) = \gamma B(z) = \gamma(B_0 + G_z \times z)$. Note that the slice thickness can be determined by the range of z (e.g., from z_1 to z_2), and the bandwidth (BW) of an RF pulse is: $BW = \omega(z_2) - \omega(z_1) = \gamma G_z(z_2 - z_1) = \gamma G_z \Delta z$. By incorporating these two into an RF pulse and applying it to a subject, spins in the selected slice are ready for MR imaging.

Frequency and phase encoding enable the localization of 2-dimensional (2D) information in the slice selected by the z-gradient. When recoding MR signals (FID) in the x-y plane, the application of a linear gradient field along the x-direction, like slice selection, enables identification of the magnetization along the x-direction: $\omega(x) =$

$\gamma B(x) = \gamma(B_0 + G_x \times x)$. Each location can have a slightly different resonance frequency. For y-direction encoding, a certain degree of phase shift can identify the location of the magnetization by applying a linear gradient field along the y-direction before frequency encoding. The combination of these two encoding techniques can localize the magnetization in the 2D imaging slice selected by the z-gradient field. Figure 2.4 shows an example of the localization scheme to generate spatial MR signals in a spin echo pulse sequence. First, a z-gradient is applied with an RF pulse (90˚) to select an imaging slice, and then after phase encoding followed by another z-gradient and RF pulse (180˚), the MR signal (FID or echo) is recorded with frequency encoding at an echo time (TE). To sweep over the y-direction, this process is repeated periodically after the repetition time (TR). These MR signals, $S(t)$, are stored in a *k*-space for image reconstruction after Fourier transformation.

2.3.2 Image reconstruction

k-space, $S(\vec{k})$, is a spatial frequency domain filled with the Fourier transformation of measured MR signals, $S(t)$, and its values are complex numbers with the unit of cycle per millimeter. For a 2D image such as in the x-y plane, the fundamental imaging equation associated with $S(\vec{k})$ is:

$$S\left(k_x(t), k_y(t)\right) = \int_{-\infty}^{\infty}\int_{-\infty}^{\infty} I(x,y)e^{-i2\pi\left(k_x(t)x + k_y(t)y\right)}dx\,dy$$

where $I(x,y)$ is an expected image, $k_x(t) = \frac{\gamma}{2\pi}\int_0^t G_x(\tau)d\tau$, and $k_y(t) = \frac{\gamma}{2\pi}\int_0^t G_y(\tau)d\tau$. Thus, the inverse Fourier transform of $S(\vec{k})$ yields the image $I(x,y)$ encoded by the MRI pulse sequence.

2.3.3 T_1-weighted imaging

T_1-weighted imaging is one of the basic MRI techniques and utilizes the difference in T_1 relaxation times of different tissues. By setting a short TR and TE in a MR pulse sequence, the intensity difference (image contrast) between different tissues is achieved in the T_1-weighted image. The short TR maximizes the contrast between tissues, and the short TE minimizes T_2 effects (refer to Figure 2.3). Because T_1-weighted imaging techniques mostly acquire the degree of T_1 relaxation with minimized T_2 effects, it is typically used to explore T_1 times. On the other hand, T_2-weighted imaging uses a relatively long TR and TE. The long TR minimizes T_1 effects, and the long TE maximizes image contrast between tissues (refer to Figure 2.3). This can be used to investigate T_2 times.

2.4 Cardiac T_1 Mapping

The conventional method for measuring T_1 relaxation time is to trace the change in intensity along the relaxation of longitudinal magnetization (M_z) at different inversion times (TI) after IR or SR RF excitation, using a T_1-weighted imaging technique. Then the T_1 can be calculated through curve fitting to the Bloch equation describing an IR or SR experiment.

As MR techniques advance, a variety of high-resolution pixel-by-pixel T_1 mapping methods for cardiovascular MRI are available within a single breath-hold (2-7). From a clinical perspective, T_1 mapping enables tissue characterization and observation of physiological changes, because the unique composition of different tissues is directly associated with their T_1 values. For instance, normal T_1 values of liver, heart, blood, and

kidney at 3 Tesla are approximately 812, 1471, 1932, and 1194 ms, respectively (8). The widely used investigational cardiac T_1 mapping pulse sequence is MOLLI using IR RF pulses (2), which acquires multiple single-shot T_1-weighted images (11 images) at different TIs within a single breath-hold (17 heartbeats). For calculation of a pixel-by-pixel T_1 map, MOLLI utilizes a three parameter non-linear curve fitting method in each pixel; $M_z(t) = A - B \times exp(-t/T_1)$ (2).

2.5 MRI Contrast Agents and Extracellular Volume Fraction

MRI contrast agents are utilized to improve image contrast during MR acquisitions and can be made of gadolinium-based (Gd, paramagnetic) compounds that mainly shorten the T_1 relaxation time. For clinical purposes, Gd contrast agents (or GBCA)(e.g., gadobenate (MultiHance) and gadoteridol (ProHance)) are administrated intravenously, and then they distribute to the extracellular space: i.e., they are extracellular contrast agents.

2.5.1 Decreasing native longitudinal relaxation time

Gd contrast agents decrease the native longitudinal relaxation time (T_1) by accelerating the energy transfer between interacting, 7 unpaired Gd electrons and surrounding protons. According to the kinetics of Gd contrast agents (9,10), the difference between the post- and pre-contrast longitudinal relaxation rate ($R_1 = 1/T_1$) is linearly proportional to the concentration of Gd:

$$\Delta R_1 = \frac{1}{T_{1,post}} - \frac{1}{T_{1,pre}} = \gamma \cdot [Gd]$$

where γ is the relaxivity of the contrast agent and $[Gd]$ is the concentration. In other words, MR properties are changed in tissues before and after the administration of Gd contrast agents. As a result, new image contrast mechanisms are available. A representative technique is called late gadolinium enhanced (LGE) imaging (see Section 2.5.2). Also, the quantification of the extracellular spaces in the myocardium can be estimated after administration of Gd (see Section 2.5.3).

2.5.2 Late gadolinium enhanced imaging

LGE MR imaging is a gold standard technique for non-invasive assessment of tissue viability after Gd injection (11,12). LGE utilizes the T_1-weighted imaging technique, based on changed longitudinal relaxation times in tissues. Damaged or infarcted tissues have different contrast agent kinetics compared to normal tissues; the wash-in/out rate of contrast agent may be slow in the damaged tissues. This difference in Gd kinetics can change post-contrast T_1 times in tissues and enable acquisition of enhanced contrast images between normal and damaged tissues. The signals from damaged tissues can be relatively maximized by acquiring a T_1-weighed image at the zero-crossing moment of normal myocardial T_1 relaxation after applying an IR pulse. As a result, the image intensity in normal tissues can be null (dark) as a reference, whereas that in damaged tissues becomes bright because damaged tissues have faster T_1 relaxation times than normal tissues (i.e., a higher concentration of Gd in damaged tissues). Therefore, LGE imaging enables visual discrimination between normal and damaged tissues.

2.5.3 Extracellular volume fraction

Based on Gd kinetics, extracellular volume fraction (ECV) can be measured non-invasively through cardiac T_1 measurements. At the equilibrium state of concentration after Gd injection (i.e., identical molar concentration per unit volume in tissues), the ratio of the concentration in myocardium to the concentration in blood is expressed as (13-15):

$$\frac{[Gd]_{myocardium}}{[Gd]_{blood}} = \frac{\Delta R_{1,myocardium}}{\Delta R_{1,blood}} = \frac{ECV}{(1 - hematocrit)}$$

where $\gamma \cdot [Gd] = \Delta R_1$. Note that Gd contrast agents can permeate into extracellular spaces due to their small molecular size relative to the capillary wall pore. Therefore, ECV in myocardium can be non-invasively calculated from pre- and post-contrast myocardial and blood T_1 values with hematocrit correction at the equilibrium state of Gd in tissues. ECV measurement is highly associated with the observation of structural remodeling in the myocardium such as from the accumulation of fibrosis or the expansion of extracellular space.

2.6 References

1. Bloch F. Nuclear induction. Physical Review 1946;70(7-8):460-474.

2. Messroghli DR, Radjenovic A, Kozerke S, Higgins DM, Sivananthan MU, Ridgway JP. Modified Look-Locker inversion recovery (MOLLI) for high-resolution T1 mapping of the heart. Magn Reson Med 2004;52(1):141-146.

3. Piechnik SK, Ferreira VM, Dall'Armellina E, Cochlin LE, Greiser A, Neubauer S, Robson MD. Shortened Modified Look-Locker Inversion recovery (ShMOLLI) for clinical myocardial T1-mapping at 1.5 and 3 T within a 9 heartbeat breathhold. J Cardiovasc Magn Reson 2010;12:69.

4. Song T, Stainsby JA, Ho VB, Hood MN, Slavin GS. Flexible cardiac T1 mapping using a modified Look-Locker acquisition with saturation recovery. Magn Reson Med 2012;67(3):622-627.

5. Slavin GS, Stainsby JA. True T1 mapping with SMART1Map (saturation method using adaptive recovery times for cardiac T1 mapping): a comparison with MOLLI. J Cardiovasc Magn Reson 2013;15(1):P3.

6. Chow K, Flewitt JA, Green JD, Pagano JJ, Friedrich MG, Thompson RB. Saturation recovery single-shot acquisition (SASHA) for myocardial T(1) mapping. Magn Reson Med 2014;71(6):2082-2095.

7. Weingartner S, Akcakaya M, Basha T, Kissinger KV, Goddu B, Berg S, Manning WJ, Nezafat R. Combined saturation/inversion recovery sequences for improved evaluation of scar and diffuse fibrosis in patients with arrhythmia or heart rate variability. Magn Reson Med 2014;71(3):1024-1034.

8. Stanisz GJ, Odrobina EE, Pun J, Escaravage M, Graham SJ, Bronskill MJ, Henkelman RM. T1, T2 relaxation and magnetization transfer in tissue at 3T. Magn Reson Med 2005;54(3):507-512.

9. Weinmann HJ, Brasch RC, Press WR, Wesbey GE. Characteristics of gadolinium-DTPA complex: a potential NMR contrast agent. AJR Am J Roentgenol 1984;142(3):619-624.

10. Rohrer M, Bauer H, Mintorovitch J, Requardt M, Weinmann HJ. Comparison of magnetic properties of MRI contrast media solutions at different magnetic field strengths. Invest Radiol 2005;40(11):715-724.

11. Kim RJ, Wu E, Rafael A, Chen EL, Parker MA, Simonetti O, Klocke FJ, Bonow RO, Judd RM. The use of contrast-enhanced magnetic resonance imaging to identify reversible myocardial dysfunction. N Engl J Med 2000;343(20):1445-1453.

12. Kim RJ, Fieno DS, Parrish TB, Harris K, Chen EL, Simonetti O, Bundy J, Finn JP, Klocke FJ, Judd RM. Relationship of MRI delayed contrast enhancement to irreversible injury, infarct age, and contractile function. Circulation 1999;100(19):1992-2002.

13. Schelbert EB, Fonarow GC, Bonow RO, Butler J, Gheorghiade M. Therapeutic targets in heart failure: refocusing on the myocardial interstitium. J Am Coll Cardiol 2014;63(21):2188-2198.

14. Pereira RS, Prato FS, Wisenberg G, Sykes J. The determination of myocardial viability using Gd-DTPA in a canine model of acute myocardial ischemia and reperfusion. Magn Reson Med 1996;36(5):684-693.

15. Arheden H, Saeed M, Higgins CB, Gao DW, Bremerich J, Wyttenbach R, Dae MW, Wendland MF. Measurement of the distribution volume of gadopentetate dimeglumine at echo-planar MR imaging to quantify myocardial infarction:

comparison with 99mTc-DTPA autoradiography in rats. Radiology 1999;211(3):698-708.

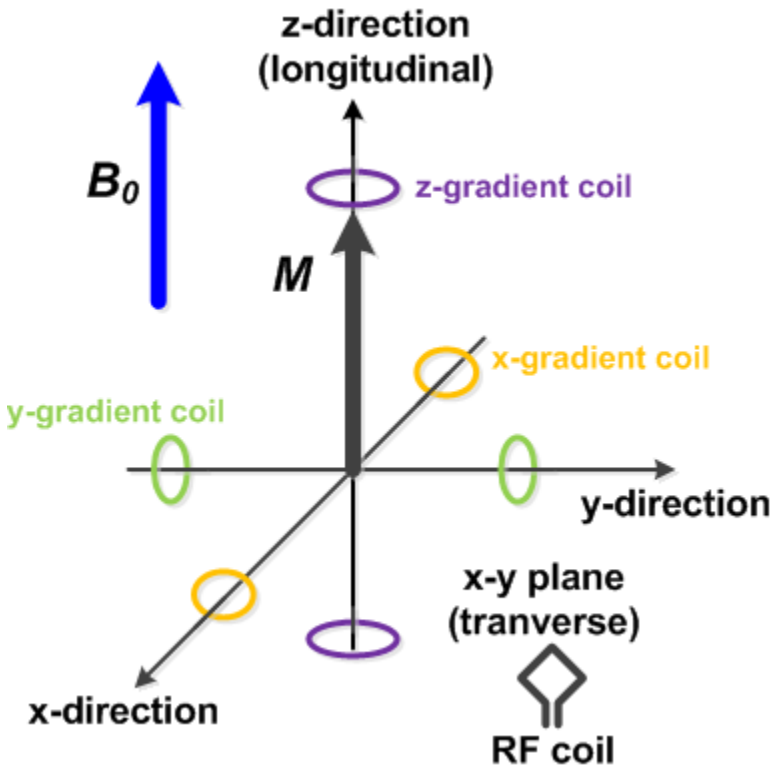

Figure 2.1. Simplified MRI system and net magnetization ($\vec{M}$) in a static magnetic field ($\vec{B_0}$).

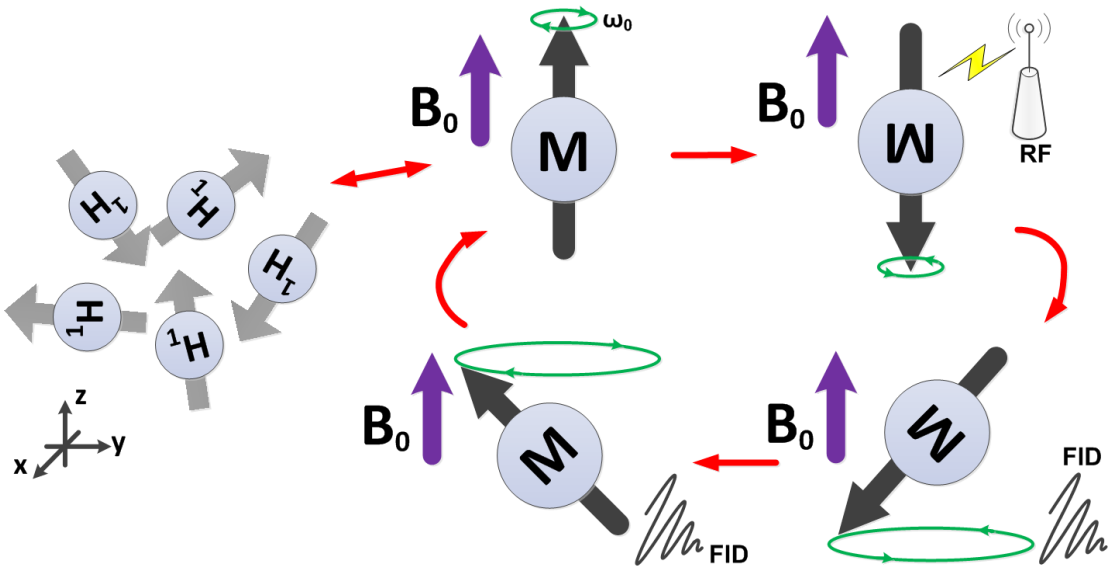

Figure 2.2. Process of MR signal (FID) generation. M = net magnetization; ω_0 = resonance frequency; RF = radio-frequency; FID = free-induction decay.

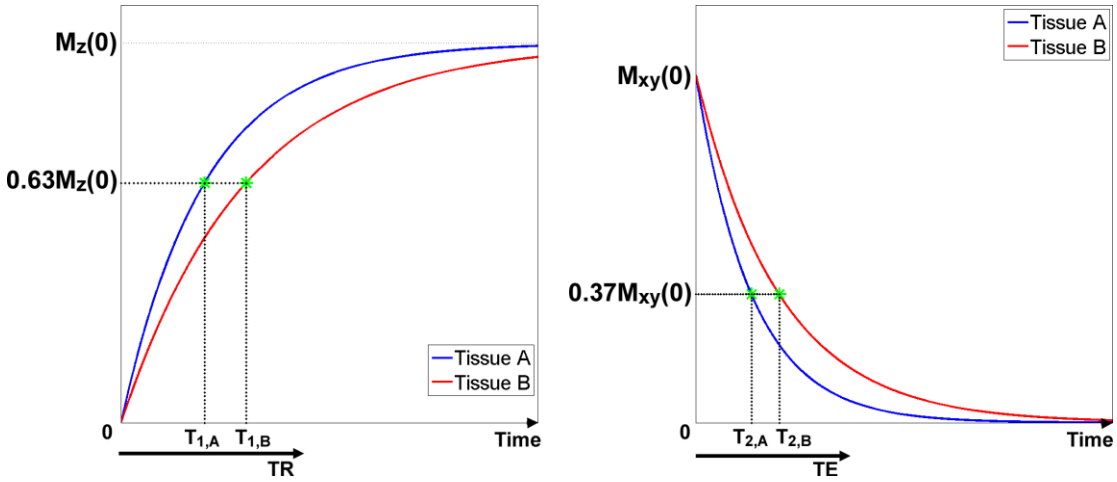

Figure 2.3. Behavior of longitudinal relaxation $\overrightarrow{M_z}$ (left) after SR RF excitation and transverse relaxation $\overrightarrow{M_{xy}}$ (right) in two different tissues. TR = repetition time; TE = echo time.

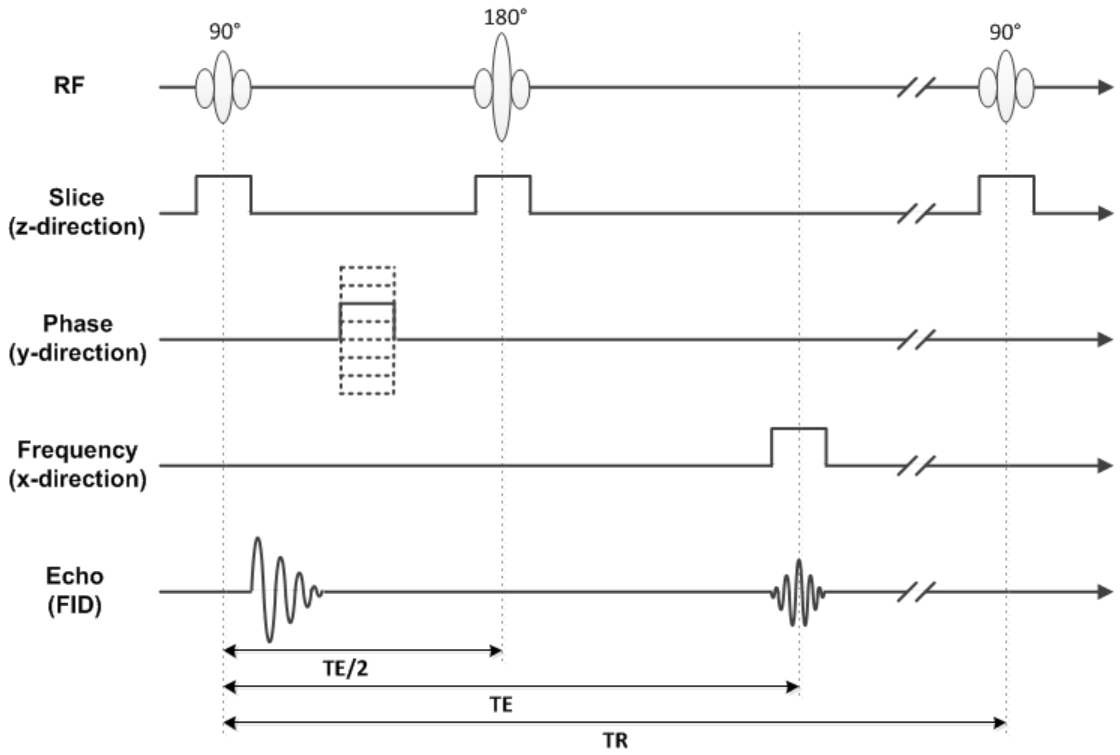

Figure 2.4. Spin echo pulse sequence diagram. TE = echo time; TR = repetition time.

CHAPTER 3

ARRHYTHMIA-INSENSITIVE RAPID (AIR) CARDIAC T_1 MAPPING PULSE SEQUENCE

This chapter describes the development of Arrhythmia-Insensitive Rapid (AIR) cardiac T_1 mapping pulse sequence, which is based on use of a robust saturation RF pulse to achieve uniform T_1 weighting, without regard to B_0 and B_1 inhomogeneities. The AIR method is inherently insensitive to irregular heart rhythms and acquires a T_1 map within 2-3 heartbeats, depending on heart rate. This work was published in *"Arrhythmia-Insensitive Rapid Cardiac T_1 mapping Pulse Sequence" Magnetic Resonance in Medicine 2013, Volume 70, Issue 5, Pages 1274-1282*. Reprinted with permission from Wiley Periodicals, Inc.

3.1 Introduction

Cardiovascular magnetic resonance (CMR) is a rapidly evolving modality for non-invasive assessment of myocardial viability. In particular, late gadolinium enhancement (LGE) MRI (1,2) is now considered the gold standard for imaging myocardial viability. The LGE mechanism is largely based on delayed washout of the contrast agent in enlarged extracellular space containing scarred and/or fibrotic myocardium compared with normal tissue. LGE MRI at approximately 10-15 min after contrast agent

administration will exhibit “hyper-enhancement” of scarred or fibrotic myocardium. While the LGE MRI method allows for accurate assessment of focal fibrosis, it is less reliable for assessment of diffuse fibrosis (3), because it requires a normal reference tissue to distinguish the fibrosis. Another inherent limitation with LGE MRI is that its data acquisition is typically performed with surface radio-frequency (RF) receiver coils. As such, LGE MRI signal is contaminated with surface coil effects (e.g., signal inhomogeneity unrelated to LGE). This inherent limitation hinders accurate identification of “border” or “gray” zones in myocardial infarction.

This study was motivated by a clinical need for developing a rapid non-invasive method to quantify diffuse fibrosis, which can arise from a number of cardiomyopathies (3) including: arrhythmias such as atrial fibrillation (AF), hypertension, diabetes mellitus, chronic renal insufficiency, myocarditis and other inflammatory diseases (4-15). LGE T_1 mapping overcomes the limitations of conventional LGE MRI because the measured T_1 is directly correlated with the contrast agent concentration in the enlarged extracellular space containing fibrosis. Therefore, LGE T_1 mapping provides a means to detect diffuse fibrosis and quantify its severity.

The most widely used cardiac T_1 mapping pulse sequence is the modified Look-Locker (LL) inversion recovery (MOLLI)(16). This pulse sequence acquires 11 single-shot images with different inversion times (TI) within a single breath-hold of 17 heartbeats (16,17). While MOLLI has been an important development in CMR, it has several known limitations. First, MOLLI uses an inversion-recovery (IR) pulse, which is inherently sensitive to heart rate and rhythm (18,19). Second, MOLLI is susceptible to T_2 effects due to the LL approach with a balanced steady-state free precession (b-SSFP)

readout (18,19). Third, MOLLI requires long breath-hold duration (~17 s), which is not conducive for whole heart imaging in a clinical setting.

Other cardiac T_1 mapping methods have been presented to partially overcome the limitations of MOLLI. Piechnik et al. proposed a shortened MOLLI (shMOLLI) sequence (20) which acquires 7 single-shot images with different TI values in a single breath-hold duration of 9 heart beats. However, shMOLLI, as a LL method, is still sensitive to T_2 effects, and it may be desirable to further decrease the scan time for higher clinical throughput. A modified LL acquisition with saturation recovery (MLLSR) technique uses an saturation-recovery (SR) pulse instead of an IR pulse to make the pulse sequence insensitive to heart rate and rhythm (17). However, MLLSR, as a LL method, is sensitive to T_2 effects, and has a relatively long scan time. A non-LL method based on SR magnetization preparation acquires multiple single-shot images with different SR time delays (TD), where each image acquisition is preceded by an SR pulse to minimize the sensitivity to T_2 effects (18,21). However, this method has a relatively long scan time.

We present a rapid cardiac T_1 mapping pulse sequence based on two single-shot image acquisitions (22): i) "proton density-weighted" (PD) image and ii) T_1-weighted (T_1w) image with recovery time on the order of T_1. This radio-frequency field (B_1) insensitive T_1 mapping approach with only two image acquisitions has been demonstrated in hip cartilage (23) and cardiac (22) applications at 3T. This study expands upon our prior work (22) with b-SSFP readout for increased signal-to-noise ratio (SNR). The proposed pulse sequence is inherently insensitive to heart rate and rhythm conditions, due to SR magnetization preparation, and T_2 effects, due to T_1 calculation from a ratio of T_1w and PD images (i.e., residual T_2 effects from readout and dummy

ramp-up RF pulses are similar for both PD and T_1w images and cancel out during T_1 calculation), and permits whole heart coverage in a clinically acceptable scan time. The purposes of this study were to develop an arrhythmia-insensitive, rapid (AIR) T_1 mapping pulse sequence and evaluate its performance against MOLLI and reference T_1 mapping method in in vitro and in vivo experiments.

3.2 Materials and Methods

3.2.1 IR vs. SR for cardiac T_1 mapping

The MOLLI T_1 mapping method based on IR T_1 weighting is sensitive to heart rate and rhythm, because the longitudinal magnetization (M_z) immediately after the IR pulse depends on the prior history of M_z recovery affected by heart rate and rhythm. In contrast, AIR T_1 mapping based on SR T_1 weighting is insensitive to heart rate and rhythm, because the M_z immediately after the SR pulse is always zero. This assumption is only valid when using a robust SR pulse (see below for more details). Figure 3.1 shows plots of M_z curves of the IR and SR pulses for three irregular heartbeats which illustrate this concept. Note that T_1 is calculated based on these curves. Another advantage of an SR pulse over an IR pulse for cardiac T_1 mapping is that it is more adaptable for rapid T_1 mapping (e.g., T_1 calculation based on two single-shot images), because the M_z is always positive. Note that for an IR acquisition, several IR image acquisitions are typically needed to resolve the sign of M_z.

3.2.2 Cardiac T_1 measurement based on two single-shot image acquisitions

We propose to acquire two single-shot b-SSFP images, where T_1 is calculated from a ratio of T_1w and PD images to cancel T_2 effects. We elected to use TD = 600 ms, based on our prior experience with LGE cardiac T_1 on the order of 600-800 ms, to achieve a good balance between T_1 sensitivity and SNR for the T_1w acquisition (24), as illustrated in Figure 3.2. The theoretical sensitivity analysis (Fig. 3.2B) shows that the signal (M_z/M_0) is sensitive to clinically relevant T_1 ranging from 263-2000 ms, where M_0 is the equilibrium magnetization. In the proposed T_1w acquisition with TD = 600 ms, tissues with short T_1 values (< 300 ms) are susceptible to noise, due to near complete recovery of M_z (i.e., $M_z/M_0 > 0.86$), whereas tissues with long T_1 values (>2400 ms) are susceptible to noise, due to insufficient recovery of M_z (i.e., $M_z/M_0 < 0.22$). With TD = 600 ms and temporal resolution of b-SSFP readout = 217 ms, our total scan time per image is 832 ms (see 3.2.5 Pulse Sequence for details). As such, for heart rates ≤ 73 beats per min (bpm), we acquired the single-shot PD and T_1w images at late diastole in two heart beats. For heart rates > 73 bpm, we acquired the PD and T_1w images at late diastole in three heart beats, as shown in Figure 3.3. For efficiency, we acquired PD images first, to ensure that initial M_z is equal to M_0, and T_1w images second, since initial M_z for the T_1w image is determined by the SR pulse and TD only (i.e., initial M_z prior to the SR pulse is irrelevant).

With these conditions, T_1 can be calculated pixel-wise by dividing the T_1w image, I_{T1W}, by the PD image, I_{PD}, to correct for the unknown M_0 and then solving the Bloch equation governing T_1 relaxation describing the ideal SR experiment:

$$\frac{I_{T_1W}=M_0\left(1-e^{-TD/T_1}\right)}{I_{PD}=M_0} = \left(1 - e^{-TD/T_1}\right) \qquad [3.1]$$

$$T_1 = \frac{-TD}{ln\left(1-\frac{I_{T1w}}{I_{PD}}\right)} \quad [3.2]$$

3.2.3 Effects of dummy RF pulses on T_1 calculation

We used 30 dummy ramp-up RF pulses with flip angles ramping from 0.2 to 34.7 (i.e., Kaiser Bessel) to minimize the oscillation of magnetization prior to b-SSFP imaging. These dummy RF pulses introduce additional T_1 and T_2 weighting onto both "PD" and T_1w images. We determined their effects by performing a numerical simulation using the Bloch equations governing T_1 and T_2 relaxations. For the simulation, we used the following conditions to achieve clinically relevant T_1 and T_2 values: pre-contrast myocardial T_1 = 1471 ms (25) and T_2 = 47 ms (26), longitudinal relaxivity (r_1) = 5.5 L/mmol/s (27), transverse relaxivity (r_2) = 11.0 L/mmol/s (27), $R_1 = R_{1,0} + r_1 \times [Gd]$, and $R_2 = R_{2,0} + r_2 \times [Gd]$, where $R_{1,0}$ is pre-contrast longitudinal relaxation rate, $R_{2,0}$ is pre-contrast transverse relaxation rate, and [Gd] is the concentration of Gd-BOPTA (MultiHance)(Bracco Diagnostics Inc., Princeton, NJ). We varied [Gd] from 0 to 0.3 mM to achieve clinically relevant T_1 ranging from 429 to 1471 ms, with matching T_2 ranging from 41 to 47 ms. For each T_1-T_2 pair, we calculated M_z immediately prior to PD and T_1w images. We then took divided the ratio of $Mz,_{T1}/M_{z,PD}$ (including ramp-up pulses) by the ideal ratio of $Mz,_{T1}/M_{z,PD}$ (without ramp-up pulses). Using Eq. [3.2], we also calculated the T_1 using the ratio of $Mz,_{T1}/M_{z,PD}$ including ramp-up pulses, and divided this calculated T_1 by the true T_1.

3.2.4 MRI hardware

Both MOLLI and AIR pulse sequences were implemented on two 3T whole-body MRI scanners (Tim Trio and Verio, Siemens Healthcare, Erlangen, Germany) equipped with a gradient system capable of achieving a maximum gradient strength of 45 mT/m and a slew rate of 200 T/m/s. The RF excitation was performed using the body coil. For phantom and goat MRI experiments conducted on the Tim Trio system, a 6-element body matrix coil array and a spine coil array (with only 6 elements on) were employed for signal reception. For canine and human experiments conducted on the Verio system, a 32-element cardiac coil (RAPID MR International, Columbus, OH) was used for signal reception.

3.2.5 Pulse sequence

The following parameters were used for both MOLLI and AIR in vivo data acquisitions: TR = 2.7 ms, TE = 1.1 ms, acquisition matrix = 192 (readout) × 144, slice thickness = 8 mm, flip angle = 35º , field of view (FOV) = 340 mm (readout) × 255 mm, GRAPPA parallel imaging factor R = 1.8, receiver bandwidth = 930 Hz/pixel, and temporal resolution = 217 ms. The MOLLI acquisition was performed in a breath-hold of 17 heart beats, using TI values as specified by Messroghli et al. (16) and linear k-space ordering. The AIR image acquisition was performed in a breath-hold of 2-3 heart beats (see Figure 3.3), depending on the heart rate, with TD = 600 ms, centric k-space ordering, and 30 dummy ramp-up RF pulses. Note that centric k-space ordering minimizes sensitivity to flip angle variation (28-30).

For B_1 insensitive T_1 weighting, we used a robust SR pulse (31) to achieve uniform

T_1 weighting within the heart at 3T, which has been shown to yield residual $M_z < 2\%$ of M_0 (31). The hybrid adiabatic-rectangular pulse train is comprised of three non-selective RF pulses: non-selective rectangular 140° pulse, non-selective rectangular 90° pulse, and non-selective adiabatic half-passage pulse. The crusher gradients inserted between RF pulses are cycled to eliminate stimulated echoes. Spoiler gradients are applied before the first RF pulse and after the third RF pulse to dephase the transverse magnetization. This B_1-insensitive SR pulse has been utilized for several applications at 3T, including cardiac T_1 mapping (28), hip cartilage T_1 mapping (23), cardiac B_1+ mapping (29), and quantitative, cardiac first-pass perfusion MRI (30).

3.2.6 Phantom studies

We made nine distilled water phantoms with different concentrations of manganese(II) chloride ranging from 0.016 - 0.183 mM, to produce a range of clinically relevant T_1 values (~500 – 2000 ms) in the heart at 3T (see Table 3.1). Manganese Chloride was chosen because it has $T_1/T_2 >> 1$. The nine phantoms were positioned inside a bath to minimize susceptibility effects. The bath contained sufficient amount of manganese chloride to minimize artifacts due to T_2 effects.

For reference T_1 measurements, an IR fast spin-echo (FSE) pulse sequence (IR-FSE) was used to acquire one PD image and 10 images with different TI values (TI = 100, 300, 500, 700, 900, 1100, 1300, 1500, 1700, 1900 ms). Relevant imaging parameters for IR-FSE include: FOV = 340 mm × 255 mm, acquisition matrix = 192 × 144, receiver bandwidth = 930 Hz/ pixel, TE = 5.1 ms, TR = 11s, and turbo factor = 7. For reference T_2 measurements, a multi-echo FSE sequence with reverse centric *k*-space ordering and

turbo factor of 2 was used (25). Relevant imaging parameters for the multi-echo FSE include: FOV = 340 mm × 255 mm, acquisition matrix = 192 × 144, TR = 1 s, receiver bandwidth = 501 Hz/ pixel, refocusing flip angle = 180°, and echo spacing = 5.1 ms, and 12 images with TE values ranging from 10.2 to 122.4 ms (10.2 ms steps).

To assess repeatability, MOLLI and AIR acquisitions were repeated 10 times at simulated heart rate and rhythm conditions of 60 bpm, 120 bpm, and arrhythmia using an electrocardiogram (ECG) triggering device. Constant heart rhythms at 60 and 120 bpm were simulated using Siemens' patient monitoring unit (PMU) simulator. For arrhythmia simulation, a customized ECG triggering device was used to generate trigger pulses at times at 0, 400, 1100, 1600, 2500, 3000, 4000, 4400, and 4900 ms, and repeated throughout to achieve an effective heart rate of 111 bpm, which were inputted to Siemens' PMU. For each heart rate and rhythm condition, the correct ECG trigger times were stamped onto the dicoms via the PMU. Using the IR-FSE as the reference, T_1 accuracy and precision were assessed by calculating normalized root-mean-square-error (NRMSE) and coefficient of variation (CV).

3.2.7 Human studies

Nine clinical patients with known history of AF (7 males and 1 female; mean age 57 ± 16 years; mean weight 80.48 ± 14.53 kg) and one healthy male subject (age = 38 years) were imaged in a mid-ventricular short-axis plane pre-contrast and 5, 10, and 15 min after administration of 0.1 mmol/kg of Gd-BOPTA. T_1 measurements were made at multiple time points after the contrast agent administration to increase the number of samples. Note that these eight AF patients were imaged during sinus rhythm, because our AF

patients are typically cardioverted immediately prior to clinical MRI examination. Image acquisition parameters for MOLLI and AIR were the same as described above, except for FOV = 350 mm × 262 mm. Image acquisition order of MOLLI and AIR was randomized to minimize bias due to their slightly different imaging time relative to the contrast agent administration time. Human imaging was performed in accordance with protocols approved by our Institutional Review Board; all subjects provided written informed consent.

3.2.8 Animal studies

Eight mongrel dogs (6 male, 2 female; mean weight 26.9 ± 4.4 kg) and nine male goats (mean weight 36.1 ± 10.4 kg) were implanted with a pacemaker in the right atrium to induce chronic AF through rapid atrial pacing. Animals were prescribed orally digoxin (0.0625 mg, once daily) and metoprolol (25-100 mg, twice daily) to control the ventricular rate to less than 150 bpm. These animals models with chronic AF were used in a longitudinal study aimed at characterizing the structural changes associated with AF. These animals were cardioverted immediately prior to MRI. MOLLI and AIR T_1 mapping pulse sequences were added to an existing animal MRI protocol. Dogs and goats were fasted for a minimum of 12 hours before MRI. Both species were anesthetized with propofol (5-8 mg/kg, IV) for intubation. Throughout MRI experiment, animals were ventilated and maintained in a surgical plane of anesthesia with 1.5-3% isoflurane. Ventilation was controlled using a ventilator (DRE Premier XP MRI-Compatible Veterinary Anesthesia Machine, DRE Veterinary, Louisville, KY). A tube was inserted into the rumen of goats to relieve gas buildup during procedures. MRI experiments were

conducted with the dogs in lateral recumbency and the goats in a sternal position. Anterior and posterior RF receiver coils were positioned to cover the heart. Heart rate, core body temperature, blood pressure, end-tidal CO_2, and oxygen saturation were continuously monitored and maintained within normal ranges. Animal imaging was performed in accordance with protocols approved by the Institutional Animal Care and Use Committee.

MOLLI and AIR T_1 mapping scans were performed using the same protocol as the human scans, except for FOV = 280 mm × 180 mm and 0.15 mmol/kg of Gd-BOPTA administration. T_1 measurements were made in a mid-ventricular short-axis plane pre-contrast and 5, 10, and 15 min after contrast agent administration. Image acquisition order of MOLLI and AIR was randomized to minimize bias due to their slightly different imaging times relative to the contrast agent administration time. To assess inter-scan variability, we repeated both MOLLI and AIR acquisitions in all 17 animals, without repositioning.

3.2.9 Image analysis

T_2 of the phantoms was calculated by non-linear least square fitting (Levenberg-Marquardt) for three parameters of the signal relaxation equation (M_0, T_2, noise) (25,32). T_1 of the phantoms was calculated by non-linear least square fitting for two parameters of the IR equation (M_0, T_1). Apparent T_1 values from the MOLLI data were calculated by non-linear least square fitting for three parameters of the LL IR equation (see (16) for more details), and the corresponding T_1 values were then derived from the apparent T_1 values based on (33). We note that MOLLI T_1 calculation was performed with motion

registration in-line on the MRI scanner (Siemens WIP # 448).

For AIR images, we used an iterative anisotropic diffusion filter to achieve a good balance between noise reduction and spatial blurring of source images (34,35). We used 15 iterations with gradient modulus threshold = 10 for the conventional anisotropic diffusion equation described in (34,35). After this pre-processing step, we performed rigid body transformation to co-register the PD and T_1w images based on a Fourier-based algorithm (36). Following these pre-processing steps, we calculated the pixel-by-pixel T_1 maps using Eq. [3.2]. Customized software in MATLAB was used to manually segment the regions of interest (ROI) (whole phantom, left ventricular myocardium, blood pool). T_1 was calculated on a pixel-by-pixel basis and averaged within the ROI.

For statistical analysis, T_1 measurements by MOLLI and AIR were compared using the Pearson's correlation and Bland-Altman analyses. Inter-scan agreements for MOLLI and AIR T_1 were assessed using the Bland-Altman analysis.

3.2.10 Theoretical noise analysis

To estimate the T_1 error due to noise, we performed a theoretical noise analysis using Eq. [3.2] as a function of true T_1 ranging from 400 to 1500 ms (5 ms steps). To estimate clinically relevant white Gaussian noise, in a 38-years-old male volunteer, we acquired one PD image acquisition with full k-space encoding and a noise map using the same pulse sequence without RF excitation. The myocardium was segmented manually, and the SNR was calculated as the ratio of the mean myocardial signal and standard deviation of noise derived from the noise map. In this subject, PD SNR was 142. Given that our proposed PD acquisition performs GRAPPA acceleration 1.8, we anticipate a PD SNR of

105. We further attenuated this value by 25% for a conservative estimate of 79. For simplicity, we let PD signal = 79 and added white Gaussian noise with standard deviation = 1 (i.e., SNR = 79). For each T_1, T_1w image signal was calculated as PD signal multiplied by the term (1-exp(-TD/T_1)). We then added the same white Gaussian noise with standard deviation =1 to the T_1w signal. Using Eq. 2, T_1 with noise was calculated with noise added PD and T_1w signals. The theoretical noise analysis was repeated 100 times (i.e., Monte Carlo). The influence of white noise on T_1 accuracy was estimated by performing linear regression analysis and calculating RMSE (T_1 with noise vs. true T_1). Reported linear regression statistics and RMSE values represent the mean ± standard deviation over 100 measurements.

3.3 Results

3.3.1 Effects of dummy RF pulses on T_1 calculation

Figure 3.4 shows plots of ratio of $Mz,_{T1}/M_{z,PD}$ with ramp-up pulses and $Mz,_{T1}/M_{z,PD}$ without ramp-up pulses and ratio of T_1 estimation with ramp-up pulses and ideal T_1 (without ramp-up pulses) as a function T_1. Our theoretical analysis confirms that 30 dummy ramp-up RF pulses have negligible effects on T_1 calculation (< 0.05%; percent error for T_1 ranging from 429 to 1471 ms).

3.3.2 Phantom studies

Figure 3.5 shows the MOLLI and AIR T_1 maps for the nine phantoms at simulated heart rate and rhythm conditions of 60 bpm, 120 bpm, and arrhythmia, as well as the corresponding bar charts summarizing the mean T_1 measured over 10 repeated acquisitions (except for IR-FSE which was acquired only once). Table 3.1 summarizes

the reference T_1 and T_2 values of the phantoms. Compared with the reference T_1 measured by IR-FSE, MOLLI and AIR had NRMSE of 8% and 3%, respectively, at 60 bpm, 28% and 3%, respectively, at 120 bpm, and 22% and 3%, respectively, at arrhythmia. In addition, MOLLI and AIR T_1 measurements had maximum CV of 1.6% and 1.1%, respectively, at 60 bpm, 5.9% and 0.6%, respectively, at 120 bpm, and 10.2% and 0.8%, respectively, at arrhythmia. These results show that AIR yields relatively accurate and precise T_1 measurements at three different heart rate and rhythm conditions.

3.3.3 In vivo studies

Figure 3.6 shows non-contrast and post-contrast (15 min) MOLLI and AIR cardiac T_1 maps for a baseline (prior to pacing) dog and a 38-year-old male volunteer. The MOLLI T_1 maps exhibited consistently lower T_1 values than the AIR T_1 maps. Table 3.2 summarizes mean non-contrast blood and myocardium T_1 values for goats, dogs, and human, as well as their mean heart rates. Compared with non-contrast myocardial T_1 measured by MOLLI (1198 ms), non-contrast myocardial T_1 measured by AIR (1501 ms) was in better agreement with a previous study which measured T_1 of an excised heart (1471 ms) using a rigorous IR pulse sequence with 35 TI values with 2 averages (26). Linear regression analysis of MOLLI and AIR T_1 values (Figure 3.7) demonstrated a strong correlation with a correlation coefficient (r) of 0.99 for combined animal and human data ($p < 0.01$). Results of the Bland-Altman analysis (Table 3.3) show that the T_1 values measured by the MOLLI and AIR methods are in poor agreement (mean difference = 162.0 ms, upper 95% limits of agreement = 348.4 ms, lower 95% limits of agreement = -24.4 ms), with a trend towards greater difference for longer T_1 values. For

inter-scan repeatability (Table 3.3), the coefficient of repeatability (CR) was 49 ms (5% of mean) for MOLLI and 79 ms (7% of mean) for AIR. Slightly larger CR for AIR can be attributed to the fact that AIR acquires only two images whereas MOLLI acquires eleven.

3.3.4 Theoretical noise analysis

For the theoretical noise analysis, mean RMSE was 24.7 ± 2.2 ms, and the calculated T_1 values with noise were strongly correlated with true T_1 values for PD SNR of 79 (see Table 3.4).

3.4 Discussion

This work demonstrates the feasibility of performing rapid cardiac T_1 mapping (e.g., 2-3 heart beats, depending on heart rate) with relatively accurate and precise T_1 values (Figs 3.5-7, Tables 3.1-3). This rapid approach is conducive for whole heart coverage in a clinical setting. Our proposed AIR T_1 mapping method has been demonstrated to be insensitive to heart rate and rhythm. While not explicitly tested in this study, our proposed AIR T_1 mapping pulse sequence is inherently insensitive to T_2 effects, because they cancel out in the ratio of T_1w and PD images acquired using centric *k*-space ordering. Our phantom studies showed that AIR yielded more accurate and precise T_1 measurements than MOLLI at three different heart rate and rhythm conditions compared with IR-FSE as the reference, suggesting that AIR may be more accurate and precise than MOLLI for cardiac T_1 mapping.

While this new pulse sequence may be clinically useful, there are several issues that warrant discussion. First, the AIR T_1 maps demonstrated good parametric map quality,

but its maps tended to be noisier than MOLLI T_1 maps. This is not surprising, since AIR and MOLLI acquire 2 and 11 images, respectively. To compensate for noise, we used an anisotropic diffusion filter to minimize the noise in the raw images, without significant spatial blurring. Another approach to increase the SNR of AIR T_1 maps is to acquire additional T_1-weighted images with different TDs, at the expense of increased scan time (18,21-23). Second, while the AIR pulse sequence is insensitive to arrhythmia in terms of T_1 weighting, the underlying cardiac phase captured by the PD and T_1w images may be mis-registered in arrhythmia. In such situation, the pixel-by-pixel T_1 calculation will lead to registration errors. One solution to this problem is to perform advanced registration methods, such as affine transformation and deformable models. Another solution is to repeat the image acquisition since it only takes 2-3 heart beats. If these solutions do not work, then one can calculate T_1 using mean myocardial signals measured from separate cardiac contour segmentation of PD and T_1w images (only valid for diffuse myocardial fibrosis). Third, some of our b-SSFP images at 3T did contain banding artifacts associated with off-resonance. We carefully excluded such regions in our image analysis, but more work (e.g., better B_0 shimming, higher receiver bandwidth, etc.) is needed to produce artifact-free b-SSFP images at 3T. We note that we routinely generate artifact free b-SSFP images at 1.5T (data not shown). Fourth, we prescribed the cutoff heart rate (73 bpm) based on the imaging parameters used in this study. For different combinations of TD and temporal resolution, different cutoff heart rates will have to be computed. Sixth, we did not use an IR spin echo pulse sequence as the gold standard for T_1 mapping in vitro. Instead, we elected to use IR FSE as the reference to accelerate the pulse sequence by a factor of 7 (e.g., turbo factor). As such, our phantom reference T_1

measurements may contain negligible errors. Seventh, we used an iterative anisotropic diffusion filter to achieve a good balance between noise reduction and spatial blurring of source images. This may lead to spatial blurring of focal fibrosis. Eighth, our phantoms had T_2 ranging from 49 to 485 ms. These values are much higher than clinically relevant T_2 values (e.g., 41 to 47 ms used in the theoretical analysis, Fig. 3.4). However, our AIR results are still valid because AIR is inherently insensitive to T_2 effects. Ninth, we used TD = 600 ms for this study because our clinical application (AF patients without myocardial infarction, LGE T_1 mapping at 15 min after administration of single dose of Gd-BOPTA at 3T) yields LGE T_1 ranging from 600-800 ms. In other clinical applications, the range of LGE T_1 will depend on a variety of factors, including contrast agent type, contrast agent dosage, specific delayed imaging time, field strength, and underlying structural heart disease. For applications where a wider range of T_1 (e.g., 200-700 ms) is expected, it is necessary to adjust the TD to be equal to the lower end of T_1, at the expense of SNR for higher end of T_1 (see Figure 3.2B). Tenth, MOLLI T_1 maps reported in this study were generated in-line with motion registration. As such, spatial blurring in MOLLI T_1 maps is due to both T_2 effects and additional spatial filtering introduced by image registration. Eleven, we elected to use the original implementation of MOLLI with linear *k*-space ordering, rather than the optimized MOLLI with centric *k*-space ordering (37). While the optimized MOLLI with centric *k*-space ordering may be superior to the original MOLLI with linear *k*-space ordering in terms of T_2 blurring, both implementations of MOLLI are sensitive to heart rate and rhythm because they are based on IR magnetization preparation.

3.5 Conclusions

Rapid cardiac T_1 mapping can be performed using our proposed AIR pulse sequence with high accuracy and precision. This rapid cardiac T_1 mapping pulse sequence may be clinically useful for assessment of diffuse myocardial fibrosis in patients, particularly in those with arrhythmia and tachycardia. It may be also useful for T_1 mapping of the whole heart.

3.6 References

1. Kim RJ, Fieno DS, Parrish TB, Harris K, Chen EL, Simonetti O, Bundy J, Finn JP, Klocke FJ, Judd RM. Relationship of MRI delayed contrast enhancement to irreversible injury, infarct age, and contractile function. Circulation 1999;100(19):1992-2002.

2. Kim RJ, Wu E, Rafael A, Chen EL, Parker MA, Simonetti O, Klocke FJ, Bonow RO, Judd RM. The use of contrast-enhanced magnetic resonance imaging to identify reversible myocardial dysfunction. N Engl J Med 2000;343(20):1445-1453.

3. Mewton N, Liu CY, Croisille P, Bluemke D, Lima JA. Assessment of myocardial fibrosis with cardiovascular magnetic resonance. J Am Coll Cardiol 2011;57(8):891-903.

4. Weber KT, Janicki JS, Shroff SG, Pick R, Chen RM, Bashey RI. Collagen remodeling of the pressure-overloaded, hypertrophied nonhuman primate myocardium. Circ Res 1988;62(4):757-765.

5. Boudina S, Abel ED. Diabetic cardiomyopathy revisited. Circulation 2007;115(25):3213-3223.

6. Factor SM, Bhan R, Minase T, Wolinsky H, Sonnenblick EH. Hypertensive-diabetic cardiomyopathy in the rat: an experimental model of human disease. Am J Pathol 1981;102(2):219-228.

7. Tanaka M, Fujiwara H, Onodera T, Wu DJ, Hamashima Y, Kawai C. Quantitative analysis of myocardial fibrosis in normals, hypertensive hearts, and hypertrophic cardiomyopathy. Br Heart J 1986;55(6):575-581.

8. Weber KT, Brilla CG. Pathological hypertrophy and cardiac interstitium. Fibrosis and renin-angiotensin-aldosterone system. Circulation 1991;83(6):1849-1865.

9. Konduracka E, Gackowski A, Rostoff P, Galicka-Latala D, Frasik W, Piwowarska W. Diabetes-specific cardiomyopathy in type 1 diabetes mellitus: no evidence for its occurrence in the era of intensive insulin therapy. Eur Heart J 2007;28(20):2465-2471.

10. Whittaker P, Boughner DR, Kloner RA. Analysis of healing after myocardial infarction using polarized light microscopy. Am J Pathol 1989;134(4):879-893.

11. Diez J, Querejeta R, Lopez B, Gonzalez A, Larman M, Martinez Ubago JL. Losartan-dependent regression of myocardial fibrosis is associated with reduction of left ventricular chamber stiffness in hypertensive patients. Circulation 2002;105(21):2512-2517.

12. Mitrofanova LB, Koval'skii GB. Myocardial morphological changes in atrial fibrillation. Arkh Patol 2011;73(6):10-14.

13. Karamitsos TD, Hudsmith LE, Selvanayagam JB, Neubauer S, Francis JM. Operator induced variability in left ventricular measurements with cardiovascular magnetic resonance is improved after training. J Cardiovasc Magn Reson 2007;9(5):777-783.

14. Mahrholdt H, Wagner A, Judd RM, Sechtem U, Kim RJ. Delayed enhancement cardiovascular magnetic resonance assessment of non-ischaemic cardiomyopathies. Eur Heart J 2005;26(15):1461-1474.

15. Bohl S, Wassmuth R, Abdel-Aty H, Rudolph A, Messroghli D, Dietz R, Schulz-Menger J. Delayed enhancement cardiac magnetic resonance imaging reveals typical patterns of myocardial injury in patients with various forms of non-ischemic heart disease. Int J Cardiovasc Imaging 2008;24(6):597-607.

16. Messroghli DR, Radjenovic A, Kozerke S, Higgins DM, Sivananthan MU, Ridgway JP. Modified Look-Locker inversion recovery (MOLLI) for high-resolution T1 mapping of the heart. Magn Reson Med 2004;52(1):141-146.

17. Song T, Stainsby JA, Ho VB, Hood MN, Slavin GS. Flexible cardiac T1 mapping using a modified Look-Locker acquisition with saturation recovery. Magn Reson Med 2012;67(3):622-627.

18. Chow K ea. MOLLI T_1 Values Have Systematic T_2 and inversion efficiency dependent errors. In Proceedings of the Annual Meeting of ISMRM, Melbourne, Australia, 2012. p. 395.

19. Gai N, Stehning C, Nacif M, Bluemke D. Modified Look-Locker T1 evaluation using Bloch simulations: human and phantom validation. Magn Reson Med 2012;DOI: 10.1002/mrm.24251.

20. Piechnik SK, Ferreira VM, Dall'Armellina E, Cochlin LE, Greiser A, Neubauer S, Robson MD. Shortened Modified Look-Locker Inversion recovery (ShMOLLI) for clinical myocardial T1-mapping at 1.5 and 3 T within a 9 heartbeat breathhold. J Cardiovasc Magn Reson 2010;12:69.

21. Slavin GS HM, Ho VB, Stainsby JA. Breath-held myocardial T1 mapping using multiple single-point saturation recovery. In Proceedings of the 20th Annual Meeting of ISMRM, Melbourne, Australia, 2012. p. 1244.

22. Breton E ea. Rapid cardiac T1 mapping within two heartbeats. In Proceedings of the SCMR/Euro CMR Joint Scientific Sessions 2011, Nice, France. O107.

23. Lattanzi R, Glaser C, Mikheev AV, Petchprapa C, Mossa DJ, Gyftopoulos S, Rusinek H, Recht M, Kim D. A B1-insensitive high resolution 2D T1 mapping pulse sequence for dGEMRIC of the HIP at 3 Tesla. Magn Reson Med 2011;66(2):348-355.

24. Haacke E, Brown R, Thompson M, Venkatesan R. Spin density, T1 and T2 quantification methods in MR imaging. Magnetic resonance imaging. New York: Wiley-Liss; 1999. p 637-667.

25. Kim D, Jensen JH, Wu E, Sheth S, Brittenham GM. Breathhold multiecho fast spin-echo pulse sequence for accurate R2 measurement in the heart and liver. Magn Reson Med 2009;62(2):300-306.

26. Stanisz GJ, Odrobina EE, Pun J, Escaravage M, Graham SJ, Bronskill MJ, Henkelman RM. T1, T2 relaxation and magnetization transfer in tissue at 3T. Magn Reson Med 2005;54(3):507-512.

27. Rohrer M, Bauer H, Mintorovitch J, Requardt M, Weinmann HJ. Comparison of magnetic properties of MRI contrast media solutions at different magnetic field strengths. Investigative Radiology 2005;40(11):715-724.

28. Breton E, Kim D, Chung S, Axel L. Rapid cardiac T1 mapping within two heartbeats. In Proceedings of the 15th Annual Meeting of SCMR/Euro CMR Joint Scientific Sessions 2011, Nice, France. O107.

29. Chung S, Kim D, Breton E, Axel L. Rapid B1+ mapping using a preconditioning RF pulse with TurboFLASH readout. Magn Reson Med 2010;64(2):439-446.

30. Breton E, Kim D, Chung S, Axel L. Quantitative contrast-enhanced first-pass cardiac perfusion MRI at 3 tesla with accurate arterial input function and myocardial wall enhancement. JMRI 2011;34(3):676-684.

31. Kim D, Oesingmann N, McGorty K. Hybrid adiabatic-rectangular pulse train for effective saturation of magnetization within the whole heart at 3 T. Magn Reson

Med 2009;62(6):1368-1378.

32. Kim D, Jensen JH, Wu EX, Feng L, Au WY, Cheung JS, Ha SY, Sheth SS, Brittenham GM. Rapid monitoring of iron-chelating therapy in thalassemia major by a new cardiovascular MR measure: the reduced transverse relaxation rate. NMR Biomed 2011;24(7):771-777.

33. Look D, Locker D. Time saving in measurement of NMR and EPR relaxation times. Rev Sci Instrum, 1970(41):250-251.

34. Perona P, Malik J. Scale-space and edge detection using anisotropic diffusion. IEEE Transactions on Pattern Analysis and Machine Intelligence, July 1990;12(7):629-639.

35. Grieg G, Kubler O, Kikinis R, Jolesz F. Nonlinear anisotropic filtering of MRI data. IEEE Transactions on Medical Imaging, June 1992;11(2):221-232.

36. Stone H, Orchard M, Chang E, Martucci S. A fast direct Fourier-based algorithm for subpixel registration of images. IEEE Transactions on Geoscience and Remote Sensing 2001;39(10):2235-2243.

37. Messroghli DR, Greiser A, Frohlich M, Dietz R, Schulz-Menger J. Optimization and validation of a fully-integrated pulse sequence for modified look-locker inversion-recovery (MOLLI) T1 mapping of the heart. JMRI 2007;26(4):1081-1086.

Table 3.1. Manganese chloride phantom concentrations, reference T_1 values measured by IR-FSE, and reference T_2 values measured by ME-FSE.

$MnCl_2$ (mM)	**0.183**	**0.120**	**0.085**	**0.063**	**0.048**	**0.036**	**0.028**	**0.021**	**0.016**
Reference T_1	535	761	982	1193	1387	1568	1754	1941	2123
T_2 (ms)	49	74	103	137	177	227	283	363	485

Table 3.2. Non-contrast left ventricular myocardial and blood pool mean T_1 values (± SD, in ms) for goat, dog, and human studies.

Tissue type	Goat HR 107 ± 15 bpm (n=9)		Dog HR 86 ± 15 bpm (n=8)		Human HR 57 ± 9 bpm (n=10)	
	MOLLI T1 (ms)	AIR T1 (ms)	MOLLI T1 (ms)	AIR T1 (ms)	MOLLI T1 (ms)	AIR T1 (ms)
Myocardium	1124 ± 36	1435 ± 79	1055 ± 26	1350 ± 59	1198 ± 46	1501 ± 69
Blood	1413 ± 74	1852 ± 182	1453 ± 66	1808 ± 124	1621 ± 125	1980 ± 123

Table 3.3. Bland-Altman and Pearson correlation analyses results for T_1 measurements in vivo.

Pair	Bland-Altman				Pearson
	Mean (ms)	Difference (ms)	Lower 95% limit (ms)	Upper 95% limit (ms)	*R*
MOLLI vs. AIR	786	162	-24.4	348.4	0.99
MOLLI vs. MOLLI (inter-scan repeatability)	899.7	6.6	-42.9	56.1	
AIR vs. AIR (inter-scan repeatability)	1126.7	4.7	-74.3	83.7	

Table 3.4. Linear regression statistics (slope, bias, R^2) and RMSE for the theoretical noise analysis repeated 100 times for PD SNR = 79. Using Eq. 2, T_1 with noise was calculated with noise added PD and T_1w signals as a function of true T_1 ranging from 400 to 1500 ms (5 ms steps). R^2 is the coefficient of determination.

Slope	Bias (ms)	R^2	RMSE (ms)
0.99 ± 0.01	-3.0 ± 4.5	0.99 ± 0.00	24.7 ± 2.2

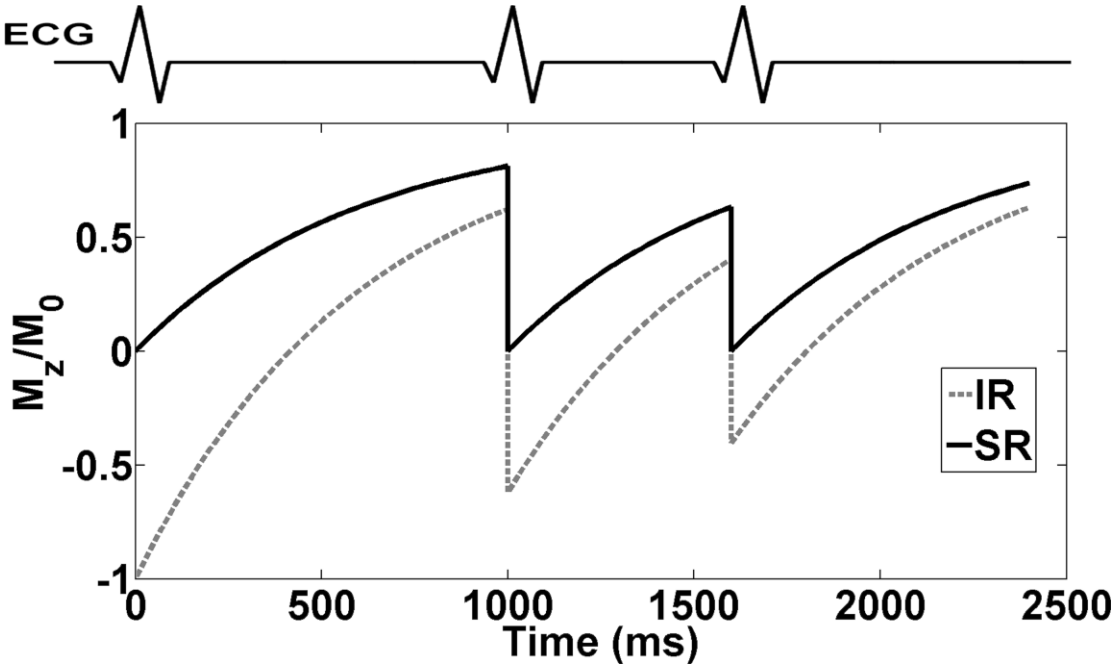

Figure 3.1. M_z curves for SR and IR acquisitions affected by heart rate and rhythm. For IR, M_z is sensitive to the prior history of recovery as a function of heart rate and rhythm, whereas, for SR, M_z is insensitive to heart rate and rhythm.

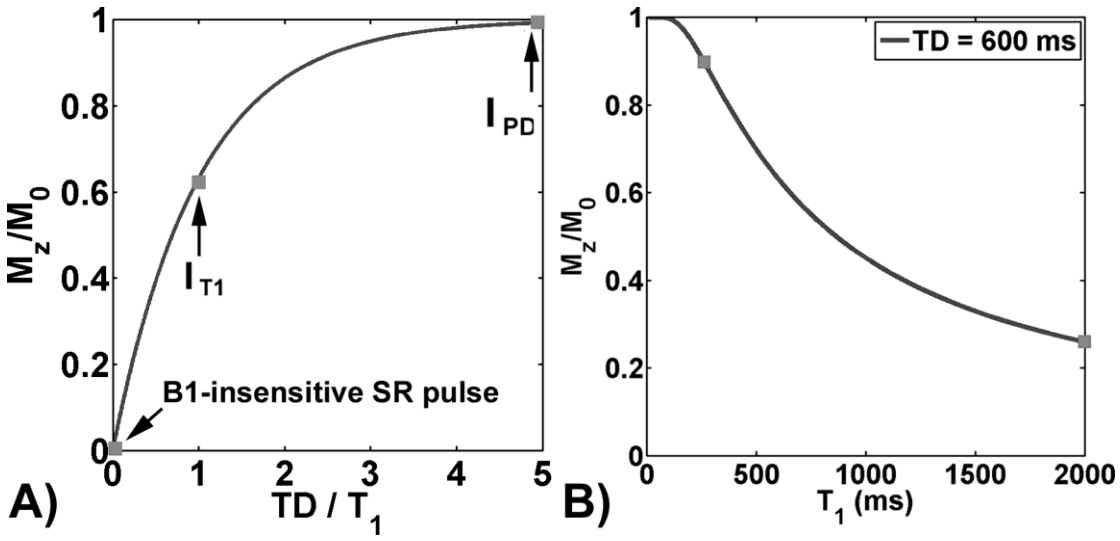

Figure 3.2. A) Theoretical M_z curve showing when T_1w image is acquired along the M_z recovery curve following B_1-insensitive T_1 weighting. Note that the PD image is acquired with the SR pulse turned off. B) Theoretical sensitivity curve illustrates that M_z/M_0 is sensitive to clinically relevant T_1 ranging from 263-2000 ms.

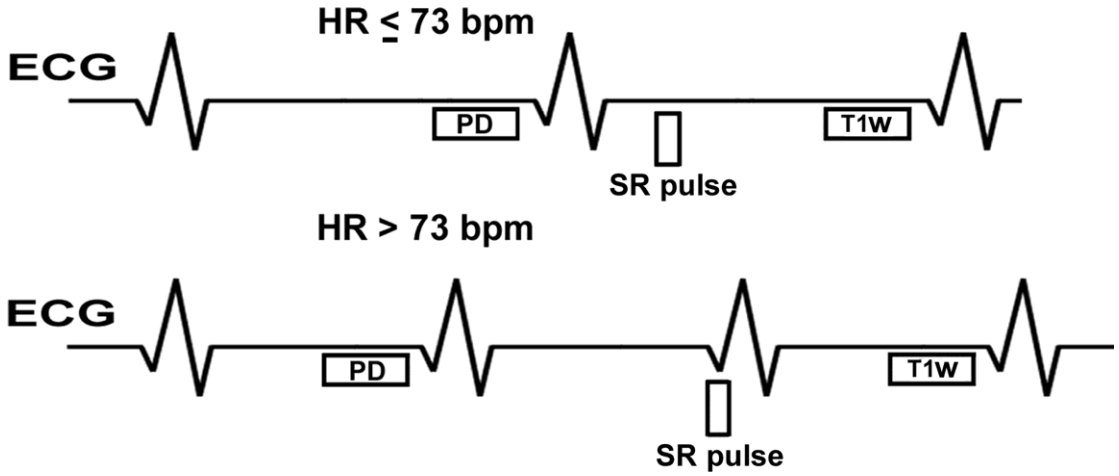

Figure 3.3. AIR pulse sequence ECG triggering schematic with TD = 600 ms, centric k-space ordering, and temporal resolution of 217 ms. For heart rates ≤ 73 bpm, PD and T_1w images are acquired in two consecutive heart beats. For heart rates > 73 bpm, PD and T_1w images are acquired in three consecutive heart beats. For efficiency, we acquire PD images first, to ensure that initial M_z is equal to M_0, and T_1w images second, since initial M_z for the T_1w image is determined by the SR pulse and TD only (i.e., initial M_z prior to the SR pulse is irrelevant).

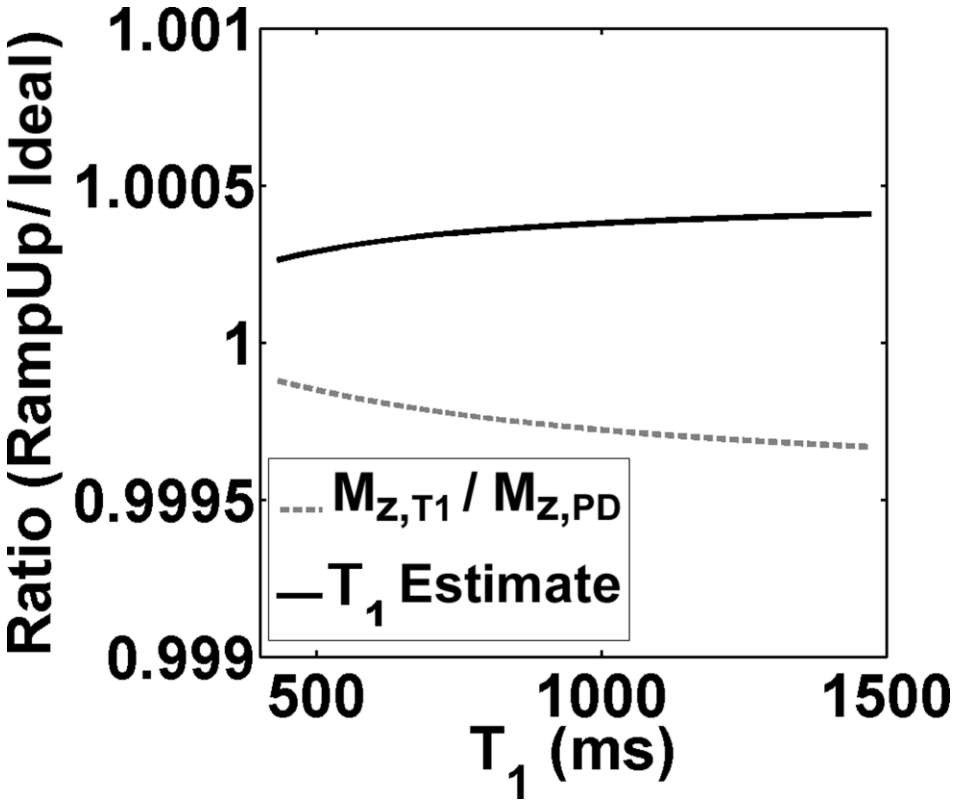

Figure 3.4. Plots of ratio of $Mz,_{T1}/M_{z,PD}$ with ramp-up pulses and $Mz,_{T1}/M_{z,PD}$ without ramp-up pulses and ratio of T_1 estimation with ramp-up pulses and ideal T_1 (without ramp-up pulses) as a function of T_1 ranging from 429 to 1471 ms. Our theoretical analysis confirms that 30 dummy ramp-up RF pulses have negligible effects on T_1 calculation (<0.05 % percent error for T_1 ranging from 429 to 1471 ms).

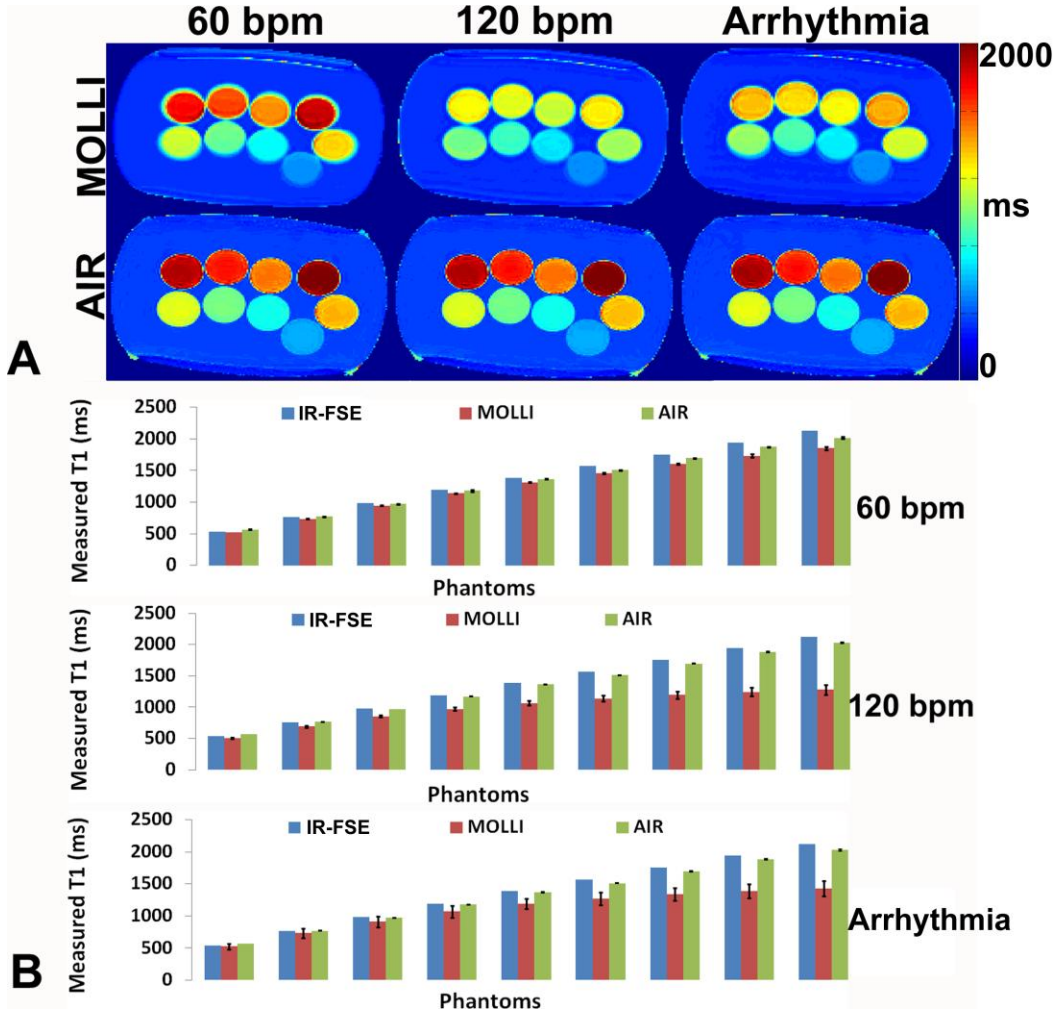

Figure 3.5. A) The top row shows MOLLI T_1 maps at (left column) 60 bpm, (middle column) 120 bpm, and (right column) simulated arrhythmia for phantoms with a range of MnCl concentrations. The middle row shows the corresponding AIR T_1 maps at 60 bpm, 120 bpm, and arrhythmia. B) The corresponding bar charts representing the mean T_1 values (n =10) for MOLLI, and AIR at 60 bpm, 120 bpm, and arrhythmia.

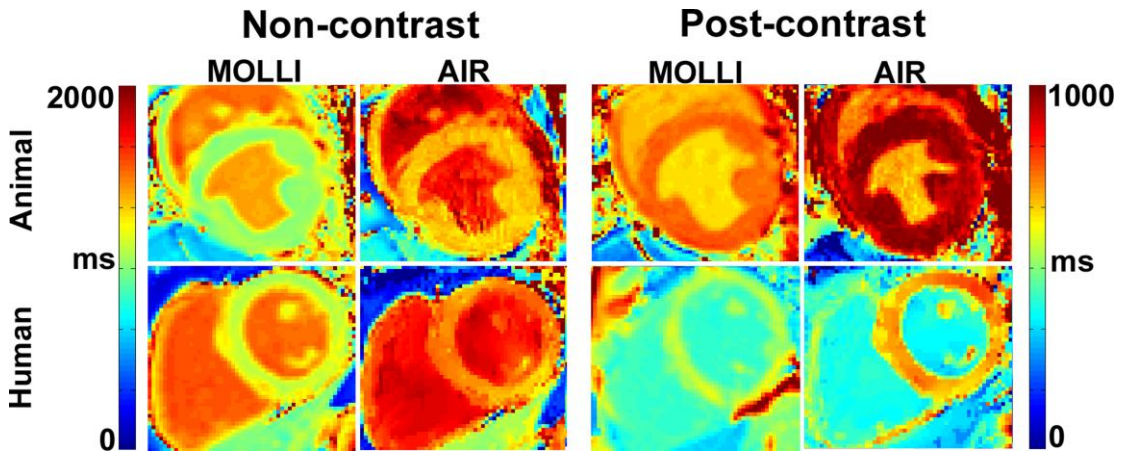

Figure 3.6. Non-contrast and post-contrast MOLLI and AIR cardiac T_1 maps for a baseline (prior to pacing) dog and a 38-year-old male volunteer. MOLLI T_1 maps show consistently lower T_1 values than AIR T_1 maps for both subjects.

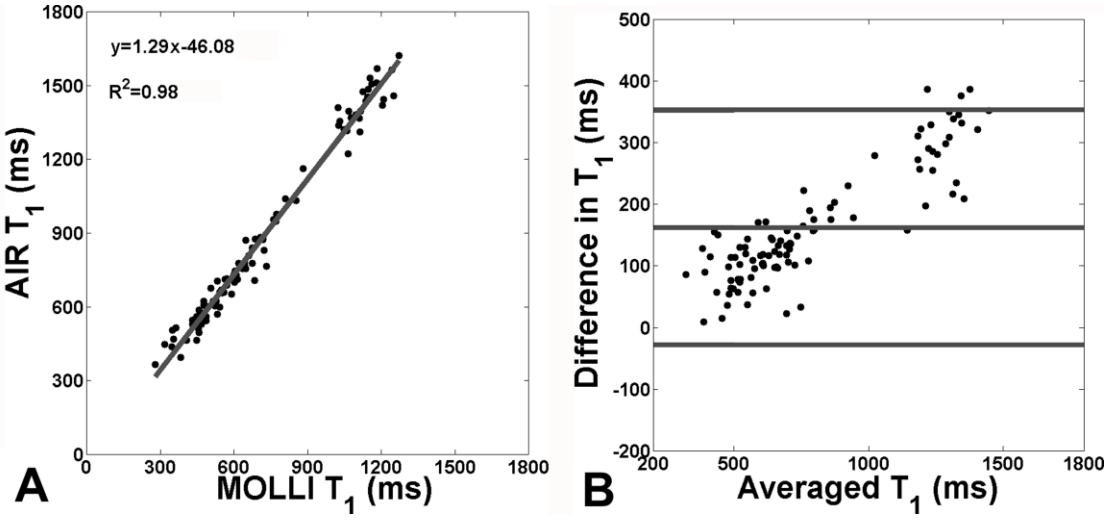

Figure 3.7. (A) Pearson's correlation and (B) Bland-Altman analyses results for MOLLI and AIR T_1 measurements in vivo.

CHAPTER 4

VALIDATION OF THE AIR CARDIAC T_1 MAPPING PULSE SEQUENCE AGAINST HISTOLOGY

This chapter describes a study that was conducted to validate the AIR cardiac T_1 mapping against histology. This work was published in *"Post-contrast myocardial T_1 and ECV disagree in a longitudinal canine study" NMR in Biomedicine 2014, Volume 27, Issue 8, Pages 988-995*. Reprinted with permission from Wiley Periodicals, Inc.

4.1 Introduction

Diffuse myocardial fibrosis is a well-established marker of adverse structural remodeling in a variety of heart diseases, including: atrial fibrillation (AF)(1), heart failure (2), hypertrophic cardiomyopathy (3,4), aortic stenosis (3,4), cardiac amyloidosis (3,4), myocardial infarction (4), diabetes (5), and congenital heart disease (6). Cardiovascular magnetic resonance (CMR) methods such as post-contrast cardiac T_1 mapping (7-9) and extracellular volume (ECV) mapping (4,9-12), derived from native and post-contrast myocardial and blood T_1 measurements, are the only validated non-invasive tests for interstitial fibrosis. The CMR field is recognizing that post-contrast myocardial T_1 measurement is sensitive to a variety of confounders, including: renal function, hematocrit, magnetic field strength, contrast agent type and dosage, and specific

delayed imaging time after administration of contrast agent. To account for these confounders, many investigators in the CMR field are migrating toward myocardial ECV as a marker of diffuse myocardial fibrosis (4,6,10-13). Despite the theoretical advantages of ECV over post-contrast myocardial T_1 (14), systematic experimental studies comparing the two measurements are largely lacking, particularly in a longitudinal setting.

Animal models provide a unique opportunity to perform a longitudinal study to monitor the temporal changes in left ventricular (LV) structural remodeling. We have established a canine model with chronic AF to study the relationship between AF and cardiac pathophysiology (15). We sought to leverage this longitudinal canine study and compare the changes in post-contrast myocardial T_1 and ECV measurements over disease duration.

4.2 Methods

4.2.1 Animal preparation for CMR at 3T

Seventeen mongrel dogs (12 females, 5 males; mean initial weight = 26 ± 4 kg) with different durations of AF induced by rapid atrial pacing (RAP)(15,16) were included in this study. These canines with chronic AF were part of a separate longitudinal study aimed at characterizing the relationship between AF and cardiac pathophysiology. For more details on the pacemaker implantation and other procedures conducted to induce AF, see reference (15). In this study, disease duration is defined as the duration since the onset of RAP, since this is the starting point at which cardiac physiology is altered. As summarized in Table 5.1, 17 dogs exhibiting different disease durations (0-22 months;

mean RAP = 205.8 ± 187 days) were included in this study, for a total of 46 CMR sessions. Canines were fasted for a minimum of 12 hours before MRI. Animals were anesthetized with propofol (5-8 mg/kg, IV) for intubation and subsequently ventilated and maintained in a surgical plane of anesthesia with 1.5-3% isoflurane. Ventilation was controlled using a ventilator (DRE Premier XP MRI-Compatible Veterinary Anesthesia Machine, DRE Veterinary, Louisville, KY). Breath-hold MRI acquisition was performed with the ventilation suspended. Each animal was electrically cardioverted approximately 30 min prior to MRI setup. Note that cardiac T_1 mapping and cine MRI methods were performed at least 1 hour after cardioversion to minimize the effects of myocardial stunning. Heart rate, core body temperature, blood pressure, end-tidal CO_2, and oxygen saturation were continuously monitored and maintained within normal ranges. Blood was drawn during the MRI exam for hematocrit calculation. Pacemaker implantation and imaging (see below) were performed in accordance with protocols approved by the Institutional Animal Care and Use Committee at the University of Utah.

4.2.2 CMR hardware

CMR was performed on two 3T whole-body MRI scanners (Tim Trio and Verio, Siemens Healthcare, Erlangen, Germany) equipped with a gradient system capable of achieving a maximum gradient strength of 45 mT/m and a slew rate of 200 T/m/s. Among a total of 46 CMR scans, 32 and 14 scans were conducted on the Verio and Tim Trio scanners, respectively. The radio-frequency excitation was performed using the body coil. For the experiments conducted on the Tim Trio system, a 6-element body matrix coil array and a spine coil array (with 6 coil elements) were employed for signal

reception. For the experiments conducted on the Verio system, a 32-element cardiac coil (RAPID MR International, Columbus, OH) was used for signal reception.

4.2.3 CMR protocol

For cardiac T_1 measurements, we used the arrhythmia-insensitive rapid (AIR) cardiac T_1 mapping pulse sequence (17). Briefly, the AIR cardiac T_1 mapping pulse sequence acquires two single-shot balanced steady-state of free precession (b-SSFP) images: 1) a proton density-weighted image and 2) a T_1-weighted image. For more details on the AIR cardiac T_1 mapping pulse sequence, see reference (17). To minimize the impact of variation in contrast agent dosage and specific delayed imaging time, we measured the weight of each animal immediately prior to MRI, administered exactly 0.15 mmol/kg of gadobenate dimeglumine (Gd-BOPTA)(MultiHance, Bracco Diagnostics Inc., Princeton, NJ), and performed cardiac T_1 mapping pre-contrast and at exactly 15 min following Gd-BOPTA administration. We assumed that 15 min after bolus injection of Gd-BOPTA is equilibrium (4,18).

The AIR cardiac T_1 mapping pulse sequence was performed with the following imaging parameters: field of view = 260 mm × 195 mm, slice thickness = 8 mm, image acquisition matrix = 192 × 144, generalized autocalibrating partially parallel acquisitions (GRAPPA)(19) acceleration factor 1.8, flip angle = 35º, saturation-recovery time delay (TD) = 600 ms, receiver bandwidth = 930 Hz/pixel, and temporal resolution = 217 ms. In this study, we also used "paired" consecutive phase-encoding steps in centric k-space ordering to minimize b-SSFP image artifacts due to eddy currents (20). We acquired 3 short-axis slices (base, mid-ventricular, apex) in a single breath-hold duration of 6-9 heart

beats (depending on heart rate). Using cardiac long-axis views as guides, for each CMR session, we defined the mid-ventricular short-axis plane as the mid-point between the mitral valve plane and apical cap, the basal short-axis plane as the mid-point between the mid-ventricular plane and mitral valve plane, and the apical short-axis plane as the mid-point between the mid-ventricular plane and apical cap.

As a secondary analysis, we also quantified LV functional parameters from retrospective ECG-gated breath-hold cine MR data acquired with b-SSFP readout (21,22). We imaged the whole heart with a stack of short-axis planes with the following imaging parameters: field of view = 260 mm × 195 mm, image acquisition matrix = 192 × 144, GRAPPA parallel imaging acceleration factor = 1.8, slice thickness = 7 mm, flip angle = 40-45º, receiver bandwidth = 1000 Hz/pixel, echo time (TE) = 1.3 ms, repetition time (TR) = 3 ms, 12-14 short-axis slices (with zero gap), spatial resolution = 1.4 mm × 1.4 mm, number of k-space lines per cardiac phase = 7, temporal resolution = 21 ms, and reconstructed cardiac frames = 25.

4.2.4 CMR image analysis

For cardiac T_1 quantification, we calculated the pixel-by-pixel T_1 map by dividing the T_1-weighted image, I_{T1W}, by the proton-density-weighted image, I_{PD}, to correct for the unknown equilibrium magnetization, M_0, and then solving the Bloch equation governing T_1 relaxation describing the ideal saturation-recovery experiment (17):

$$\frac{I_{T1w}}{I_{PD}} = \frac{M_0\left(1 - e^{-TD/T_1}\right)}{M_0} = \left(1 - e^{-TD/T_1}\right)$$

$$T_1 = \frac{-TD}{ln\left(1 - \frac{I_{T1w}}{I_{PD}}\right)}$$

Customized software in MATLAB was used to manually segment the myocardial contours and LV blood pool for each image (i.e., independent contour tracings for native and post-contrast T_1 maps per imaging plane per animal per CMR session). Care was taken to avoid partial volume averaging for each contour tracing. AIR cardiac T_1 data were randomized for analysis by the first reader (KH), who was blinded to the cine MR and histology results. Myocardial and blood T_1s were averaged within their respective contours for each of three LV locations (base, mid, apex). Myocardial ECV was calculated according to (13): $(1 - hematocrit) \times \left(\Delta R_{1,m}/\Delta R_{1,b}\right) \times 100\%$, where $R_{1,m}$ is $1/T_1$ of myocardium, and $R_{1,b}$ is $1/T_1$ of blood, and Δ is the difference between post-contrast and native.

For cardiac functional assessment, short-axis cine MR images were analyzed using Argus software (Siemens Healthcare, Erlangen, Germany). Another reader (MK), who was blinded to the T_1 and histology results, manually segmented the endocardial and epicardial LV contours in end-diastole and end-systole to calculate the following LV functional parameters: end diastolic volume (EDV), end systolic volume (ESV), stroke volume (SV), LV ejection fraction (LVEF), and LV mass. We note that papillary muscle was excluded for volume measurements, whereas it was included for mass measurement. The interventricular septum was included as part of the LV, while the left ventricular outflow tract was excluded.

4.2.5 Histological analysis

Six canines enrolled in this study were terminated at their scheduled disease duration (0, 164, 435, 478, 686, and 690 days since the onset of RAP). Post-mortem tissue

specimens (approximately 1 cm × 1 cm × 1 cm in size) were extracted from mid-ventricle of the antero-lateral LV wall of excised hearts fixed in 10% buffered formalin. Tissues were processed according to standard pathology protocol (i.e., tissues fixed in formalin, embedded in paraffin blocks, and sectioned at 4-6 μm). On average, a total of 6-10 sections were prepared with Masson's Trichrome stain to quantify collagen volume fraction (CVF). In a consensus fashion, light-microscopic examination was performed by two experienced pathologists (ECH, RL), who were blinded to animal history, disease duration, and CMR results. The optimal histologic areas were identified visually by consensus, and the resulting digital images were captured using Infinity 2 microscope digital camera (Lumenera, Ottawa, Ontario, Canada) at 100× magnification. Each digital image was evaluated for CVF quantification using customized segmentation software. This software requires user input to learn the patterns, intensity, and color for inclusion (myocytes and interstitial fibrosis) and exclusion (red blood cells, blood vessels, and adipose tissue) elements. We used several training slides of LV tissues with Masson's Trichrome stain to establish the inclusion and exclusion classification criteria. After training, the software generates automatically a classification mask by detecting fibrosis and myocyte pixels based on the trained inclusion and exclusion classification criteria. The two pathologists then compared the resulting classification mask to the original digital Trichrome image, in order to visually confirm the accuracy of the software in identifying the appropriate elements. Finally, using the resulting classification mask (see Figure 4.2), CVF was calculated as the pixel count of fibrosis (blue) divided by that of myocytes (red).

4.2.6 Statistical analysis

For statistical analysis of temporal changes in CMR parameters, we examined the association between the repeated measurements of these parameters and disease duration using a linear-mixed-effect model (LMEM)(23) (N = 46). The exchangeable correlation structure was used to specify the correlation structure among the repeated measurements within each animal. This longitudinal study has an unbalanced distribution of repeated measurements for the different animals. We resolved this issue with LMEM, where the repeated measurements within each animal are treated as a cluster of observations. All LMEMs were fitted with the random intercept for each animal and disease duration as the fixed effect, where p-value < 0.05 was considered significant. Individual trajectories of CMR parameters were plotted over disease duration. For the temporal change analysis, myocardial and blood T_1 values were averaged over the basal and mid-ventricular short-axis planes. Apical short-axis plane results were excluded for the temporal change analysis, because they may be susceptible to partial volume averaging effects. We note that animals with only one data point (dogs 5, 9, 11, 13, 14, 16, 17) were excluded for the temporal change analysis (but included for other analyses).

For statistical analysis of post-mortem LV tissues, we examined the association between histologic quantification of CVF and disease duration using linear regression (N = 6), where p-value < 0.05 was considered significant.

We also performed the following secondary analyses. To investigate whether there are regional differences in T_1 measurements between 3 different short-axis planes, we performed analysis of variance (ANOVA) for native myocardial T_1, native blood T_1, post-contrast myocardial T_1, and post-contrast blood T_1 measurements. To investigate

whether the two different 3T MRI scanners produce different T_1 results, we performed a two-sample t-test (two-tailed) for native myocardial and blood T_1 measurements only, since the native T_1 measurements did not change significantly over disease duration and allows a comparison across different animals (see Table 4.2). To investigate whether electrical cardioversion induces myocardial edema, in 5 animals, we performed native T_1 mapping before and 1 hour after cardioversion and compared their native T_1 measurements. A paired t-test (two-tailed) was used to compare native myocardial T_1 between pre and post-cardioversion (N = 5), where p-value < 0.05 was considered significant.

4.3 Results

Figure 4.1 shows representative cardiac T_1 maps in three short-axis planes of a dog at 464 days since the onset of RAP, illustrating good data and contour tracing quality used in this study. Figure 4.2 shows post-mortem LV specimens of two different dogs with Masson's trichrome staining at baseline and 22 months after the onset of RAP, as well as their corresponding classification masks used to quantify CVF. These LV specimens and classification masks illustrate good data quality used in this study.

In 17 animals observed over disease duration ranging from 0-22 months (mean RAP = 205.8 ± 187 days), post-contrast myocardial T_1 decreased significantly from 872 to 698 ms (Fig. 4.3; $p < 0.001$), which corresponds to a 24.9% relative reduction. In contrast, ECV increased from 21.0 to 22.0% ($p = 0.38$), which corresponds to only a 4.5% relative increase. This discrepancy was partially investigated by histologic analysis of post-mortem LV tissues. In 6 different dogs sacrificed at different disease duration ranging

from 0-22 months, CVF quantified by histology increased from 0.9 to 1.9% (Fig. 4.3; slope = 0.044, bias = 1.2%, correlation coefficient = 0.30; $p = 0.56$), which agreed more with ECV than post-contrast myocardial T_1.

We examined other parameters to identify the cause for this discrepancy. Among cardiac T_1 data (native myocardial T_1, native blood T_1, post-contrast blood T_1), only post-contrast blood T_1 decreased significantly from 578 to 402 ms (Fig. 4.3; $p < 0.001$), which corresponds to a 43.8% relative reduction. Note that the temporal trends in post-contrast myocardial and blood T_1s are similar. Both native myocardial T_1 and native blood T_1 did not change significantly (Table 4.2). Among LV functional parameters (EDV, ESV, SV, LVEF, and LV mass), only LVEF decreased significantly from 46.1 to 33.6% ($p = 0.02$; Table 4.2), which corresponds to a 37.2% relative reduction, suggesting progressively worsening LV dysfunction.

The results from the secondary analyses (regional variations in T_1, inter-scanner variability of native T_1, comparison of native myocardial T_1 between pre and post-cardioversion) were as follows. In all animals, the mean native cardiac T_1, native blood T_1, post-contrast cardiac T_1, and post-contrast blood T_1 values were not different between basal, mid-ventricular, and apical short-axis planes (see Table 4.3 for the statistics). According to a two-sample t-test (two-tailed), only mid-ventricular and basal myocardial T_1 measurements were significantly different between two different 3T MRI scanners ($p < 0.05$; see Table 4.4), but note that the magnitude of the percent change was less than 4% for each parameter (i.e., negligible). In 5 animals, the mean native myocardial T_1 before (1374 ± 34 ms) and 1 hour after cardioversion (1399 ± 27 ms) was not different ($p = 0.36$), which corresponds to only a 1.8% relative increase.

4.4 Discussion

In this study, in canine models with chronic AF (0 - 22 months), we measured the temporal changes in post-contrast myocardial T_1 and myocardial ECV, both of which have been associated with interstitial fibrosis (4,7-12). In the observed canines, post-contrast myocardial T_1 decreased significantly over disease duration, whereas myocardial ECV did not. Histologic quantification of CVF in a subset of animals suggests a non-significant difference in CVF over disease duration, which agrees more with ECV than post-contrast myocardial T_1. We note that a more comprehensive study, including histologic, cardiac, and renal functional analyses, is warranted to test rigorously which CMR parameter (ECV or post-contrast myocardial T_1) agrees more with CVF. Interestingly, post-contrast blood T_1 decreased significantly over disease duration, suggesting that decreasing post-contrast myocardial T_1 may have been largely driven by decreasing post-contrast blood T_1. This observational study is the first report of conflicting findings between post-contrast myocardial T_1 and ECV in the context of a longitudinal study. The results of this study agrees with a prior cross-sectional study (9), which first reported a weak association between post-contrast myocardial T_1 and ECV in a sub-analysis.

This study also highlights the benefits of myocardial ECV over post-contrast myocardial T_1. In the 17 animals studied over disease duration ranging from 0-22 months with an identical AIR cardiac T_1 mapping protocol (MRI at exactly 15 min after administration of 0.15 mmol/kg of MultiHance), we observed decreasing trends in post-contrast myocardial T_1 and post-contrast blood T_1. These temporal trends suggest that decreasing post-contrast myocardial T_1 may have been largely driven by decreasing post-

contrast blood T_1. Our cine MRI data showed that LVEF decreased significantly with disease duration, and it is plausible that a reduced cardiac output could lead to higher concentration of contrast agent in the blood at 15 min after administration (i.e., since less blood is delivered to the kidney per unit time). We note that the separate longitudinal study design did not anticipate renal function to be influenced by chronic AF. Unfortunately, due to the nature of this study (retrospective analysis of data collected from a separate longitudinal study), we are unable to measure changes in renal function over disease duration. Consequently, we are unable to draw a conclusion on what caused the decreasing trend in post-contrast blood T_1 over disease duration. Despite the lack of renal functional data and limited histologic data, our study suggests that CVF agrees better with ECV than post-contrast myocardial T_1.

It should be noted that canine T_1 measurements reported in this pre-clinical study may not be translatable to other pre-clinical studies using different CMR protocols. A variety of factors, such as field strength, contrast agent type and dosage, specific delayed imaging time, pulse sequence type, heart rate and rhythm, may influence the accuracy of T_1 measurements. Therefore, CMR researchers must be careful when translating T_1 values presented in this preclinical study into their own studies.

4.5 Study Limitations

A limitation of this study is that the enrolled canines were part of a separate longitudinal study. Consequently, our animal data had an unbalanced distribution of repeated measurements (see Table 4.1). We used LMEM to account for the unbalanced distribution of repeated measurements. Another limitation of this study is that the

histologic analysis was performed for only 6 animals (N=6), which were sacrificed according to the study objectives of the separate longitudinal study. In addition, for each animal, we analyzed a post-mortem tissue specimen of approximately 1 cm × 1 cm × 1 cm in size from the mid-ventricle of the antero-lateral LV wall to represent the whole LV. While it would be more comprehensive to analyze tissues from multiple locations of the LV, this study did not have access to the rest of the heart. A more comprehensive histological evaluation (e.g., biopsy over disease duration) is warranted to confirm our CMR findings. However, we note that performing longitudinal biopsies would add considerable expense and procedural risk to the separate longitudinal study. Furthermore, biopsy samples of the right ventricular septum are small in size (~1-2 mm in length), thereby harder to process and sensitive to sampling errors. Another potential confounder is heart-rate variation in animals under anesthesia during MRI. We typically maintain a steady level of isoflurane during MRI, but the animals' heart rate varies within and across MRI sessions. Consequently, cardiac functional parameters may have been affected by variations in heart rate. Although we performed cine CMR at least one hour after cardioversion, cardiac functional parameters reported in this study may have been influenced by residual myocardial stunning.

4.6 Conclusions

This study shows that post-contrast myocardial T_1 and ECV may disagree in a longitudinal canine study. A more comprehensive study, including histologic, cardiac, and renal functional analyses, is warranted to test rigorously which CMR parameter (ECV or post-contrast myocardial T_1) agrees more with CVF.

4.7 References

1. Ling LH, Kistler PM, Ellims AH, Iles LM, Lee G, Hughes GL, Kalman JM, Kaye DM, Taylor AJ. Diffuse ventricular fibrosis in atrial fibrillation: noninvasive evaluation and relationships with aging and systolic dysfunction. J Am Coll Cardiol 2012;60(23):2402-2408.

2. de Leeuw N, Ruiter DJ, Balk AH, de Jonge N, Melchers WJ, Galama JM. Histopathologic findings in explanted heart tissue from patients with end-stage idiopathic dilated cardiomyopathy. Transplant International 2001;14(5):299-306.

3. Fontana M, White SK, Banypersad SM, Sado DM, Maestrini V, Flett AS, Piechnik SK, Neubauer S, Roberts N, Moon JC. Comparison of T1 mapping techniques for ECV quantification. Histological validation and reproducibility of ShMOLLI versus multibreath-hold T1 quantification equilibrium contrast CMR. J Cardiovasc Magn Reson 2012;14:88.

4. White SK, Sado DM, Fontana M, Banypersad SM, Maestrini V, Flett AS, Piechnik SK, Robson MD, Hausenloy DJ, Sheikh AM, Hawkins PN, Moon JC. T1 mapping for myocardial extracellular volume measurement by CMR: bolus only versus primed infusion technique. JACC Cardiovascular Imaging 2013;6(9):955-962.

5. Wong TC, Piehler KM, Kang IA, Kadakkal A, Kellman P, Schwartzman DS, Mulukutla SR, Simon MA, Shroff SG, Kuller LH, Schelbert EB. Myocardial extracellular volume fraction quantified by cardiovascular magnetic resonance is increased in diabetes and associated with mortality and incident heart failure admission. European Heart Journal 2013.

6. Broberg CS, Chugh SS, Conklin C, Sahn DJ, Jerosch-Herold M. Quantification of diffuse myocardial fibrosis and its association with myocardial dysfunction in congenital heart disease. Circ Cardiovasc Imaging 2010;3(6):727-734.

7. Iles L, Pfluger H, Phrommintikul A, Cherayath J, Aksit P, Gupta SN, Kaye DM, Taylor AJ. Evaluation of diffuse myocardial fibrosis in heart failure with cardiac magnetic resonance contrast-enhanced T1 mapping. J Am Coll Cardiol 2008;52(19):1574-1580.

8. Sibley CT, Noureldin RA, Gai N, Nacif MS, Liu S, Turkbey EB, Mudd JO, van der Geest RJ, Lima JA, Halushka MK, Bluemke DA. T1 mapping in cardiomyopathy at cardiac MR: comparison with endomyocardial biopsy. Radiology 2012;265(3):724-732.

9. Miller CA, Naish JH, Bishop P, Coutts G, Clark D, Zhao S, Ray SG, Yonan N, Williams SG, Flett AS, Moon JC, Greiser A, Parker GJ, Schmitt M. Comprehensive validation of cardiovascular magnetic resonance techniques for

the assessment of myocardial extracellular volume. Circ Cardiovasc Imaging 2013;6(3):373-383.

10. Flett AS, Hayward MP, Ashworth MT, Hansen MS, Taylor AM, Elliott PM, McGregor C, Moon JC. Equilibrium contrast cardiovascular magnetic resonance for the measurement of diffuse myocardial fibrosis: preliminary validation in humans. Circulation 2010;122(2):138-144.

11. Kehr E, Sono M, Chugh SS, Jerosch-Herold M. Gadolinium-enhanced magnetic resonance imaging for detection and quantification of fibrosis in human myocardium in vitro. Int J Cardiovasc Imaging 2008;24(1):61-68.

12. Jerosch-Herold M, Sheridan DC, Kushner JD, Nauman D, Burgess D, Dutton D, Alharethi R, Li D, Hershberger RE. Cardiac magnetic resonance imaging of myocardial contrast uptake and blood flow in patients affected with idiopathic or familial dilated cardiomyopathy. Am J Physiol Heart Circ Physiol 2008;295(3):H1234-H1242.

13. Arheden H, Saeed M, Higgins CB, Gao DW, Bremerich J, Wyttenbach R, Dae MW, Wendland MF. Measurement of the distribution volume of gadopentetate dimeglumine at echo-planar MR imaging to quantify myocardial infarction: comparison with 99mTc-DTPA autoradiography in rats. Radiology 1999;211(3):698-708.

14. Moon JC, Messroghli DR, Kellman P, Piechnik SK, Robson MD, Ugander M, Gatehouse PD, Arai AE, Friedrich MG, Neubauer S, Schulz-Menger J, Schelbert EB. Myocardial T1 mapping and extracellular volume quantification: a Society for Cardiovascular Magnetic Resonance (SCMR) and CMR Working Group of the European Society of Cardiology consensus statement. J Cardiovasc Magn Reson 2013;15:92.

15. Dosdall DJ, Ranjan R, Higuchi K, Kholmovski EG, Angel N, Li L, Macleod R, Norlund L, Olsen A, Davies CJ, Marrouche NF. Chronic atrial fibrillation causes left ventricular dysfunction in dogs but not goats: experience with dogs, goats, and pigs. Am J Physiol Heart Circ Physiol 2013.

16. Nishida K, Michael G, Dobrev D, Nattel S. Animal models for atrial fibrillation: clinical insights and scientific opportunities. Europace 2010;12(2):160-172.

17. Fitts M, Breton E, Kholmovski E, Dosdall D, Vijayakumar S, Hong K, Ranjan R, Marrouche N, Axel L, Kim D. Arrythmia insensitive rapid cardiac T1 mapping pulse sequence. Magn Reson Med 2013;70:1274-1282.

18. Schelbert EB, Testa SM, Meier CG, Ceyrolles WJ, Levenson JE, Blair AJ, Kellman P, Jones BL, Ludwig DR, Schwartzman D, Shroff SG, Wong TC. Myocardial extravascular extracellular volume fraction measurement by

gadolinium cardiovascular magnetic resonance in humans: slow infusion versus bolus. J Cardiovasc Magn Reson 2011;13:16.

19. Griswold MA, Jakob PM, Heidemann RM, Nittka M, Jellus V, Wang J, Kiefer B, Haase A. Generalized autocalibrating partially parallel acquisitions (GRAPPA). Magn Reson Med 2002;47(6):1202-1210.

20. Bieri O, Markl M, Scheffler K. Analysis and compensation of eddy currents in balanced SSFP. Magn Reson Med 2005;54(1):129-137.

21. Carr JC, Simonetti O, Bundy J, Li D, Pereles S, Finn JP. Cine MR angiography of the heart with segmented true fast imaging with steady-state precession. Radiology 2001;219(3):828-834.

22. Barkhausen J, Goyen M, Ruhm SG, Eggebrecht H, Debatin JF, Ladd ME. Assessment of ventricular function with single breath-hold real-time steady-state free precession cine MR imaging. AJR Am J Roentgenol 2002;178(3):731-735.

23. Diggle P, Diggle P. Analysis of longitudinal data. Oxford ; New York: Oxford University Press; 2002. xv, 379 p. p.

Table 4.1. Summary of animal gender, initial weight, and MRI date with respect to days since RAP. 0 day corresponds to before inducing RAP. Mean RAP = 205.8 ± 187 days.

Canine Number	Gender	Initial weight (kg)	MRI date, RAP (days)
1	F	24.0	443, 478
2	M	32.7	268, 331, 401, 464, 539, 616
3	M	30.0	152, 180, 215, 262, 334, 418, 663
4	M	31.1	167, 223, 286, 349, 423
5	F	26.0	33
6	F	24.0	0, 97, 203, 412
7	F	22.7	0, 130, 164, 352
8	F	19.0	0, 37, 135, 164
9	F	23.0	0
10	F	26.9	0, 109, 230
11	F	27.2	0
12	F	25.2	0, 113
13	M	30.8	0
14	M	25.2	0
15	F	28.2	27, 48
16	F	27.1	0
17	F	29.0	0

Table 4.2. LMEM statistics to estimate the temporal changes of CMR parameters. We note that the T_1 and ECV measurements are averaged over the basal and mid-ventricular short-axis planes. CI: confidence interval; SE: standard error. Mean RAP = 205.8 ± 187 days. For graphical displays of these parameters, see Figure 4.3. Percent change is defined as 100% × (final-initial)/initial.

CMR Variable	Estimated change per month (95% CI)	SE	*p*-value	*Percent Change*
Native myocardial T_1	0.44(-1.97, 2.86) ms	1.18	0.71	0.7 %
Native blood T_1	-1.17(-6.04, 3.96) ms	2.38	0.62	-1.3 %
Post-contrast myocardial T_1	-8.11 (-11.31, -4.92) ms	1.55	<0.001	-24.9 %
Post-contrast blood T_1	-7.89 (-10.98, -4.79) ms	1.50	<0.001	-43.8 %
ECV	0.049 (-0.064, 0.16) %	0.06	0.38	4.5 %
EDV	0.21 (-0.37, 0.78) ml	0.28	0.47	-37.2 %
ESV	0.55 (-0.08, 1.18) ml	0.31	0.09	5.5 %
SV	-0.18 (-0.56, 0.20) ml	0.19	0.34	22.2 %
LVEF	-0.58 (-1.05, -0.10) %	0.23	0.02	-12.2 %
LV Mass	-0.19 (-0.61, 0.22) g	0.20	0.34	-3.9 %

Table 4.3. Comparison of mean native myocardial T_1, native blood T_1, post-contrast myocardial T_1, and post-contrast blood T_1 values for the basal, mid-ventricular, and apical short-axis planes. According to ANOVA, all four T_1 measurements were not different among the three short-axis planes. Mean RAP = 205.8 ± 187 days.

CMR variable	Base	Mid	Apex	*p*-value
Native myocardial T_1	1383 ± 44 ms	1372 ± 47 ms	1390 ± 53 ms	0.19
Native Blood T_1	1725 ± 105 ms	1719 ± 104 ms	1692 ±89 ms	0.29
Post-contrast myocardial T_1	831 ± 74 ms	811 ± 82 ms	823 ± 81 ms	0.71
Post-contrast Blood T_1	527 ± 77 ms	521 ± 82 ms	534 ± 80 ms	0.54

Table 4.4. Comparison of mean native myocardial and blood T_1 values across two different 3T MRI scanners. According to a two-sample t-test (two-tailed), only mid-ventricular and basal myocardial T_1 measurements were significantly different ($p < 0.05$), but note that the magnitude of the percent change was less than 4% for each parameter (i.e., negligible). Percent change is defined as 100% × (Trio-Verio)/Verio.

CMR variable	Verio	Tim Trio	*p*-value	Percent change
Native apical myocardial T_1	1396 ± 57 ms	1379 ± 42 ms	0.35	-1.2 %
Native mid-ventricular myocardial T_1	1386 ± 43 ms	1340 ± 40 ms	0.002	-3.3 %
Native basal myocardial T_1	1399 ± 36 ms	1348 ± 42 ms	<0.001	-3.7 %
Native apical blood T_1	1689 ± 82 ms	1700 ± 106 ms	0.73	0.6 %
Native mid-ventricular blood T_1	1728 ± 108 ms	1700 ± 97 ms	0.41	-1.6 %
Native basal blood T_1	1730 ± 109 ms	1713 ± 100 ms	0.63	-1.0 %

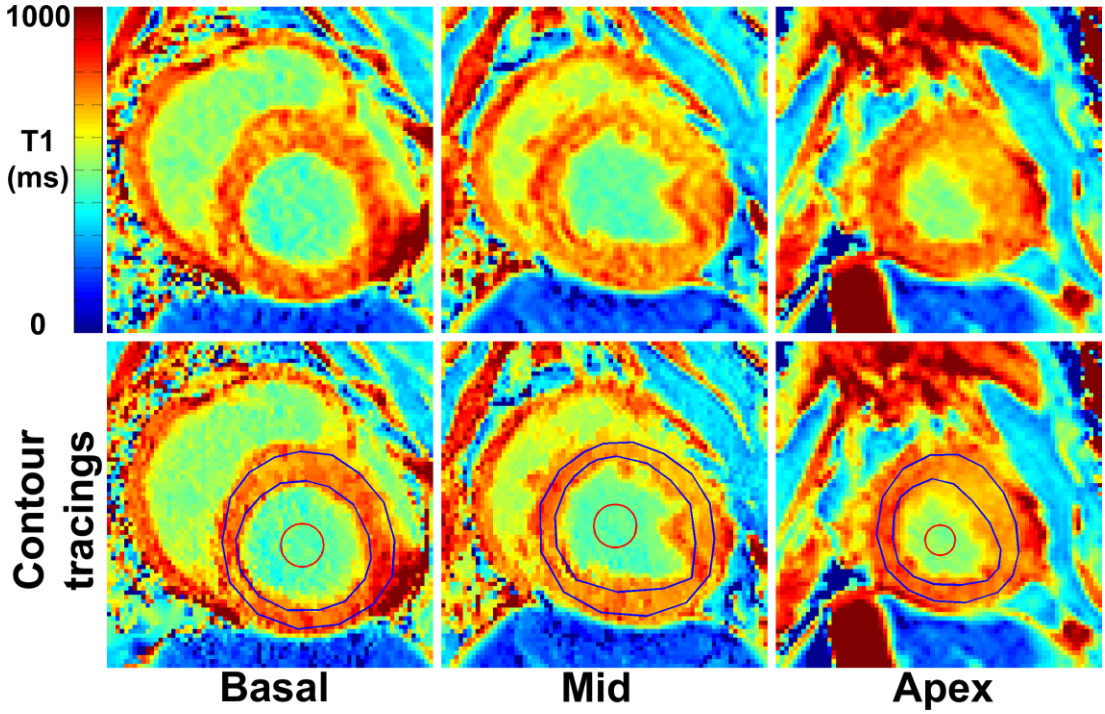

Figure 4.1. Representative post-contrast cardiac T_1 maps (top row) and the same maps with contour tracings (bottom row), illustrating good data and contour tracing quality used in this study: basal (left), mid-ventricular (middle), and apical (right) planes.

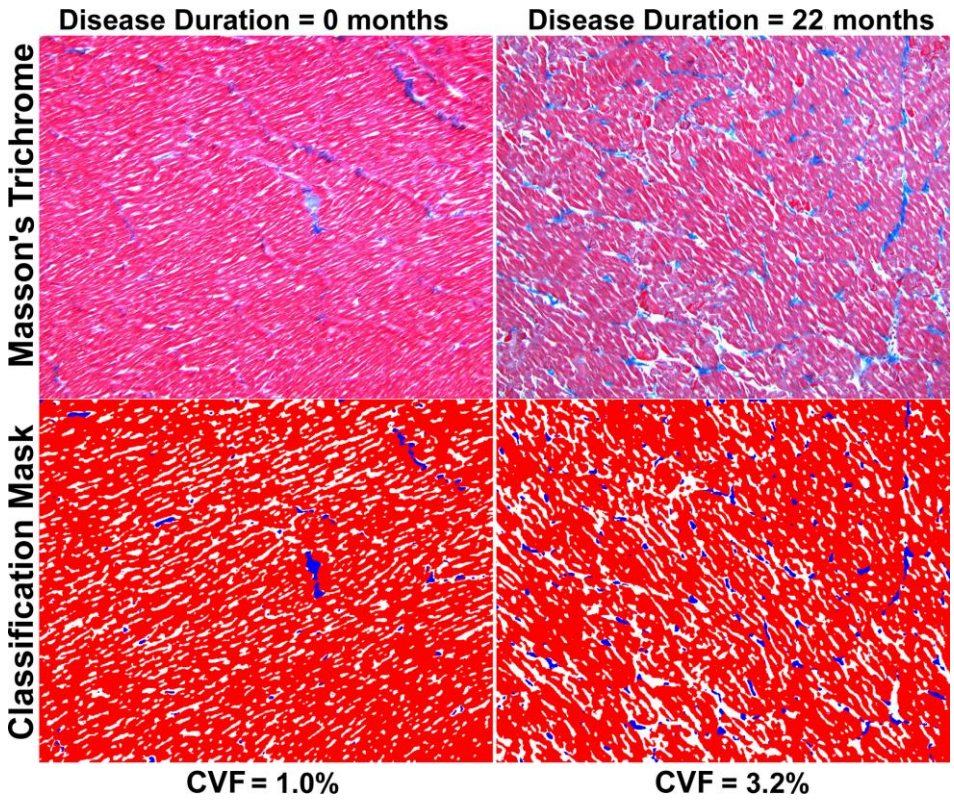

Figure 4.2. Post-mortem LV samples with Masson's trichrome stain (top row) and the resulting classification masks (bottom row) used to calculate CVF: RAP = 0 (left) and RAP = 22 months (right). All specimens displayed with 10× magnification. Red: myocyte; blue: interstitial fibrosis; white: interstitium (and additional artificial space introduced during histologic slide preparation).

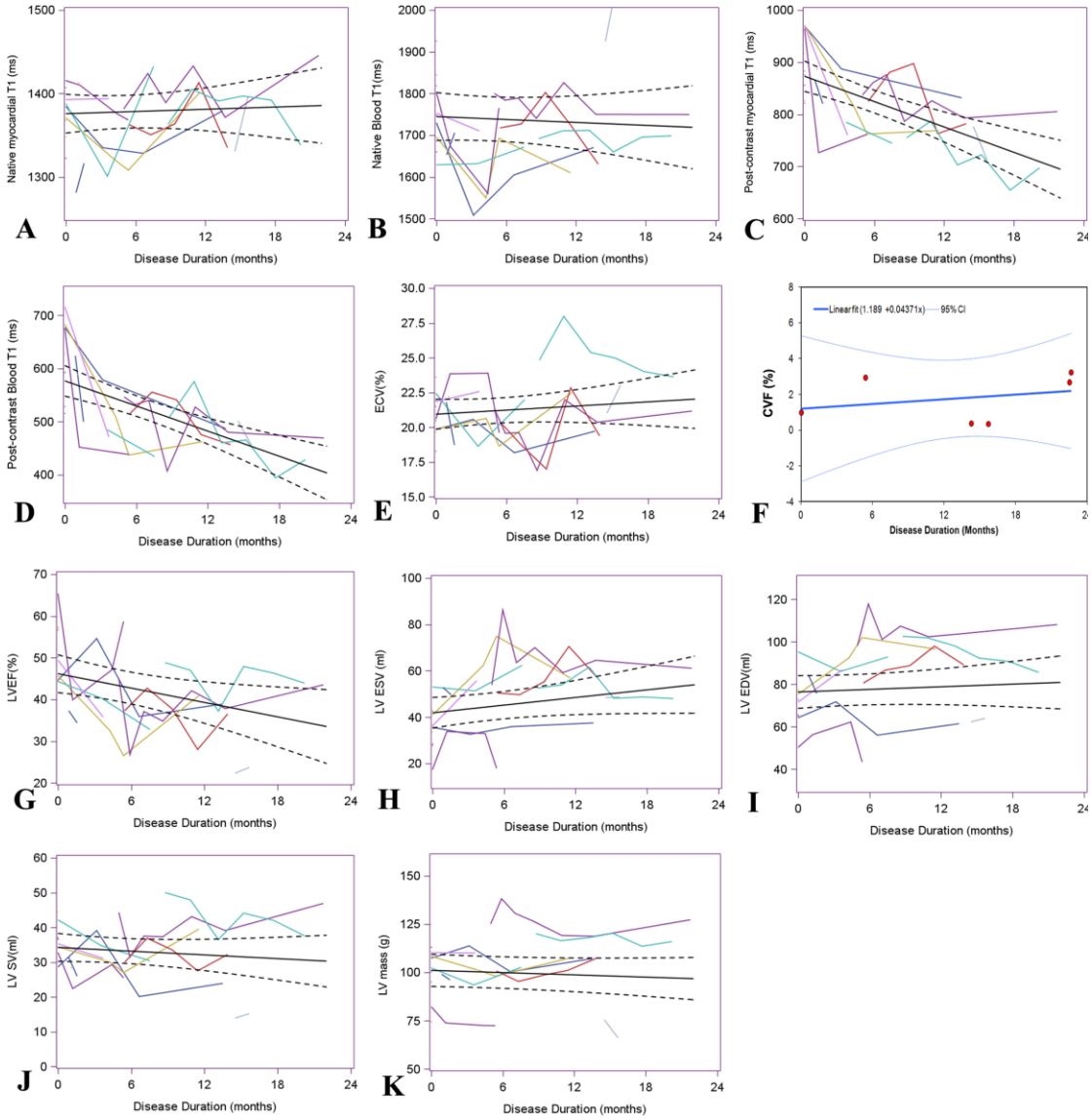

Figure 4.3. Plots of the estimated regression line (solid line), along with the 95% confidence intervals (dashed lines), describing the temporal changes in the following parameters: native myocardial T_1 (a), native blood T_1 (b), post-contrast myocardial T_1 (c), post-contrast blood T_1 (d), ECV (e), and histologic quantification of CVF (f), LVEF (g), ESV (h), EDV (i), SV (j), LV mass (k). For the statistics, see Table 4.2.

CHAPTER 5

COMPARISON OF AIR AND MOLLI CARDIAC T_1 MAPPING PULSE SEQUENCES

This chapter describes systematic differences between AIR and MOLLI cardiac T_1 mapping pulse sequences. This work was published in *"MOLLI and AIR T_1 mapping pulse sequences yield different myocardial T_1 and ECV measurements" NMR in Biomedicine 2014, Volume 27, Issue 11, Pages 1419-1426*. Reprinted with permission from Wiley Periodicals, Inc.

5.1 Introduction

Diffuse myocardial fibrosis is a marker of adverse structural remodeling in a variety of heart diseases. While myocardial biopsy is the current gold standard for assessment of diffuse cardiac fibrosis, it is rarely clinically indicated due to its associated non-negligible risk of complications and sensitivity to sampling errors. Cardiovascular magnetic resonance (CMR) is the only proven non-invasive modality for quantifying diffuse myocardial fibrosis. Both post-contrast myocardial T_1 (1-4) and myocardial extracellular volume (ECV) fraction (4-8), derived from native and post-contrast myocardial and blood T_1 measurements, have been associated with diffuse interstitial fibrosis burden. These promising developments and findings are establishing the foundation towards non-

invasive myocardial biopsy with CMR (9).

Among several different cardiac T_1 mapping pulse sequences reported in literature (10-19), modified Look-Locker Inversion-recovery (MOLLI)(10) is the most widely used and commercially available as a work-in-progress. While MOLLI has been an important development in CMR, it requires a long scan time (17 heart beats) and is known to be sensitive to rapid heart rate and arrhythmia (20,21), T_2 and magnetization transfer effects (19), and inversion pulse efficiency (22,23). These limitations are particularly concerning for imaging patients with irregular heart rhythm and/or rapid rates (e.g., atrial fibrillation). In response, we developed an arrhythmia-insensitive-rapid (AIR) cardiac T_1 mapping pulse sequence (15) based on transmit radio-frequency field (B_1+)-insensitive saturation-recovery of magnetization preparation (24), in order to enable accurate cardiac T_1 mapping in patients with rapid heart rate and/or arrhythmia. Because AIR cardiac T_1 mapping is relatively new, reports of its performance are limited to a few preliminary studies (15,25-27).

Recently, the CMR field is recognizing that post-contrast myocardial T_1 is sensitive to confounders such as renal function, hematocrit, magnetic field strength, contrast agent type and dosage, and specific delayed imaging time after administration of contrast agent. Hence, the CMR field is migrating towards ECV, because it is largely insensitive to such confounders. Several recent studies using MOLLI have reported ECV cutoff values to distinguish between normal and diseased myocardium (4,28-30). It is unclear if these cutoff values are translatable to different T_1 mapping pulse sequences such as AIR and others. This is especially important since other studies have reported that inversion-recovery based T_1 mapping pulse sequences produce lower accuracy but higher precision

than saturation-recovery based T_1 mapping pulse sequences (31). As an important step towards clinical and pre-clinical utility of AIR, it is necessary to determine whether AIR and MOLLI yield comparable myocardial ECV (i.e., determine if ECV cutoff values established by MOLLI are translatable to AIR). The purpose of this study was to evaluate, in well-controlled canine and pig experiments, the relative accuracy and precision, as well as intra- and inter-observer variability in data analysis, of ECV measured with AIR as compared with MOLLI.

5.2 Methods

5.2.1 MRI hardware

CMR was performed on two 3T whole-body MRI scanners (Verio and Tim Trio, Siemens Healthcare, Erlangen, Germany), each equipped with a gradient system capable of achieving a maximum gradient strength of 45 mT/m and a slew rate of 200 T/m/s. The radio-frequency excitation was performed using the body coil. The pig experiments were performed on the Tim Trio MRI scanner with standard receiver coil arrays (typically 12-elements total). Canine experiments were performed on the Verio MRI scanner with a 32-element cardiac coil array (RAPID MR International, Columbus, OH).

5.2.2 Pulse sequence

We used the MOLLI (Siemens WIP # 448) and AIR cardiac T_1 mapping pulse sequences with balanced steady-state of free precession (b-SSFP) readout and the following identical set of imaging parameters: field of view = 280 mm × 210 mm (phase-encoding), image acquisition matrix = 192 × 144 (phase-encoding), spatial resolution =

1.5 mm × 1.5 mm, slice thickness = 8 mm, generalized autocalibrating partially parallel acquisitions (GRAPPA)(32) acceleration factor 1.8, TR = 2.7 ms, TE = 1.1 ms, flip angle = 35º, receiver bandwidth = 930 Hz/pixel, saturation-recovery time delay (TD) = 600 ms, and temporal resolution = 217 ms.

Figure 5.1 shows pulse sequence diagrams of AIR and MOLLI. Briefly, AIR acquires one proton-density weighted image and one T_1 weighted image with breath-hold duration = 2-3 heart beats (depending on heart rate). MOLLI acquires 11 T_1 weighted images following three inversion pulse modules (3-3-5, as shown). In this study, for AIR, we used "paired" consecutive phase-encoding steps in centric k-space ordering to minimize b-SSFP artifacts arising from eddy currents (33). For MOLLI with breath-hold duration = 17 heart beats, we used the inversion times (i.e., 3-3-5) and flip angle of 35° as previously described (34).

5.2.3 Animal subjects

Animal MRI was performed in accordance with protocols approved by our Institutional Animal Care and Use Committee. We note that this CMR study was added onto separate canine and pig CMR experiments, and that cardiac tissues were not made available for histolic analysis. We note that pig experiments were conducted after the canine experiments were completed, in order to acquire additional data for analysis of precision (i.e., since repeated measurements were not made in canines). For both canine and pig experiments, animals were anesthetized with propofol (5-8 mg/kg, IV) for intubation and subsequently ventilated and maintained in a surgical plane of anesthesia with 1.5-3% isoflurane. Ventilation was controlled using a ventilator (DRE Premier XP

MRI-Compatible Veterinary Anesthesia Machine, DRE Veterinary, Louisville, KY). Breath-hold CMR image acquisitions were performed at end-expiration with the respirator suspended. Heart rate, core body temperature, blood pressure, end-tidal CO_2, and oxygen saturation were continuously monitored and maintained within normal ranges. Blood was drawn during the CMR exam for hematocrit calculation.

5.2.4 Experiment 1: Evaluation of relative accuracy in canines

We imaged 16 mongrel dogs with normal myocardium (8 males and 8 females; 29.9 ± 4.2 kg) to assess the agreement of myocardial T_1 and ECV measurements between MOLLI and AIR. In each dog, we performed native cardiac T_1 mapping and post-contrast cardiac T_1 mapping in a mid-ventricular short-axis plane during steady-state equilibrium of gadobenate dimeglumine (Gd-BOPTA)(Multihance, Bracco Diagnostics Inc., Princeton, NJ; ~45 min after slow infusion at 0.002 mmol/kg/min). This slow infusion rate was determined empirically based on our extensive experience with large animal (dogs, goats, pigs) CMR experiments. Note that steady-state equilibrium ensures identical concentration of Gd-BOPTA throughout repeated MRI measurements and allows for a fair comparison of post-contrast myocardial and blood T_1 measurements by two different pulse sequences. Furthermore, by performing CMR during equilibrium, the specific pulse sequence order was irrelevant.

5.2.5 Experiment 2: Evaluation of relative precision in pigs

Following the completion of separate canine experiments, we conducted an additional experiment to evaluate the precision of AIR compared with MOLLI. Specifically, we

imaged 6 female pigs (mean weight = 50 ± 1.4 kg) with normal myocardium to assess scan-to-scan repeatability of MOLLI and AIR. Similar to the canine experiment, in each pig, we performed native cardiac T_1 mapping and post-contrast cardiac T_1 mapping in a mid-ventricular short-axis plane during steady-state equilibrium of Gd-BOPTA. MOLLI and AIR T_1 mapping acquisitions were repeated to quantify scan-to-scan repeatability.

5.2.6 Image analysis

MOLLI T_1 maps were generated in-line on the MRI scanner (Siemens WIP # 448). AIR T_1 maps were generated off-line as described in reference (15). Customized software in MATLAB (R2009a, MathWorks, Inc., Natick, MA) was used to manually segment the myocardial contours and blood pools in the left ventricle for each data set separately. Care was taken to avoid partial volume averaging for each contour tracing. T_1 was calculated for AIR (15) and MOLLI (10) according to their corresponding equation. Myocardial and blood T_1 values were averaged within their respective region of interest. Myocardial ECV was calculated as (35):

$$\boldsymbol{ECV}\ (\%) = (\mathbf{1} - \boldsymbol{hematocrit}) \times \left(\Delta \boldsymbol{R_{1,m}} / \Delta \boldsymbol{R_{1,b}}\right) \times \mathbf{100}\%$$

where $R_{1,m}$ is $1/T_1$ of myocardium, and $R_{1,b}$ is $1/T_1$ of blood, and Δ is the difference between post-contrast and native.

To assess the impact of data quality on analysis, we assessed intra- and inter-observer variability in calculation of T_1 and ECV (canine data only). For assessment of intra-observer variability, one observer (K.H) repeated the image analysis, with at least two weeks of separation from the first analysis. For assessment of inter-observer variability,

the second observer (D.K) independently analyzed the data. The two observers were blinded to each other, pulse sequence type, and animal identity.

5.2.7 Statistical analysis

For canine data, we performed a pair-wise t-test to compare T_1 and ECV between MOLLI and AIR. We also performed linear regression, concordance correlation (which accounts for the intercept or additive bias), and Bland-Altman analyses on cardiac T_1 and ECV measurements to assess correlation and agreement between MOLLI and AIR data. For assessment of intra- and inter-observer variability, the Bland-Altman analysis was performed on T_1 and ECV measurements. A p-value < 0.05 was considered statistically significant.

For pig data, we performed Bland-Altman analysis on myocardial T_1 and ECV to calculate the coefficient of repeatability (CR), which is defined as 1.95 × standard deviation of the difference. To avoid confusion with terminology, we note that CR increases with variability in repeated measurements (i.e., lower agreement). All statistical analyses were performed using the Analyse-it software (Analyse-it Software, Ltd., Leeds, United Kingdom).

5.3 Results

5.3.1 Experiment 1: Evaluation of relative accuracy in canines

Figure 5.2 shows representative native and post-contrast MOLLI and AIR cardiac T_1 maps of one dog, illustrating typical image quality with both acquisitions. As expected, MOLLI T_1 maps derived from 11 images exhibited better overall signal-to-noise ratio

(SNR) than AIR T_1 maps derived from only 2 images. In this dog (heart rate = 95 bpm), MOLLI and AIR cardiac T_1 mapping pulse sequences yielded different T_1 and ECV values (see Figure 5.2 caption for more details).

In 16 dogs (mean heart rate = 98.8 ± 17.5 bpm; mean hematocrit = 0.42 ± 0.02), as expected, mean T_1 was significantly different ($p < 0.001$) between MOLLI (891 ± 373 ms) and AIR (1071 ± 503 ms), but, surprisingly, mean ECV between MOLLI (21.8 ± 2.1 %) and AIR (19.6 ± 2.4%) was also significantly different ($p < 0.001$). Pair-wise t-test revealed significant differences for all pairs ($p < 0.0001$), except for post-contrast blood T_1 ($p = 0.55$; Table 5.1). Figure 5.3 shows scatter plots representing the linear regression and Bland-Altman analyses on T_1 and ECV between MOLLI and AIR acquisitions. According to the linear regression and concordance correlation analyses, T_1 values were strongly correlated (Pearson's correlation coefficient = 0.99, slope = 1.33, bias = -117.6 ms, $p < 0.0001$; concordance correlation coefficient = 0.87). According to the Bland-Altman analysis, the mean difference in T_1 was 179 ms (± 95% confidential interval (CI) = 468/-109 ms), which corresponds to 18% of the mean T_1 value (981 ms). According to the linear regression analysis, ECV values were moderately correlated (Pearson's correlation coefficient = 0.65, slope = 0.77, bias = 2.8%, $p < 0.001$). According to the concordance correlation analysis, ECV values were weakly correlated (correlation coefficient = 0.43). According to the Bland-Altman analysis, the mean difference in ECV was -2.2% (± 95% CI = 1.5/-5.9%), which corresponds to 10.8% of the mean ECV value (20.7%).

5.3.2 Experiment 2: Evaluation of relative precision in pigs

Consistent with canine data, in 6 pigs (mean heart rate = 78.1 ± 12.1 bpm; mean hematocrit = 0.30 ± 0.04), mean T_1 was significantly different ($p < 0.01$) between MOLLI (899.0 ± 462.8 ms) and AIR (1051.2 ± 635.0 ms), and mean ECV was significantly different also ($p < 0.05$) between MOLLI (25.6 ± 3.1%) and AIR (20.7 ± 1.6%). CR of T_1 was considerably lower for MOLLI (32.5 ms) than AIR (82.3 ms), and CR of ECV was also lower for MOLLI (1.8%) than AIR (4.5%). Recall that, according to the Bland-Altman analysis, lower CR means lower variability (i.e., higher agreement).

5.3.3 Evaluation of intra- and inter-observer variability in analysis

For T_1 calculations (Figure 5.4), the intra-observer agreements for MOLLI and AIR data sets were 0.6 ms (upper/lower 95% limits of agreement = 5.3/-4.0 ms) and 0.4 ms (upper/lower 95% limits of agreement = 9.2/-8.5 ms), respectively. These correspond to CR of 4.7 and 8.8 ms for MOLLI and AIR, respectively. The corresponding inter-observer agreements for T_1 derived from MOLLI and AIR data sets were 0.009 ms (upper/lower 95% limits of agreement = 9.8/-9.8 ms) and 0.4 ms (upper/lower 95% limits of agreement = 22.7/-21.9 ms), respectively. These correspond to CR of 9.8 and 22.3 ms for MOLLI and AIR, respectively.

For ECV calculations (Figure 5.5), the intra-observer agreements for MOLLI and AIR data sets were -0.09% (upper/lower 95% limits of agreement = 0.5/-0.7%) and 0.02% (upper/lower 95% limits of agreement = 0.5/-0.4%), respectively. These correspond to CR of 0.6 and 0.5% for MOLLI and AIR, respectively. The corresponding inter-observer agreements for ECV derived from MOLLI and AIR data sets were -0.2%

(upper/lower 95% limits of agreement = 1.1/-1.6%) and -0.1% (upper/lower 95% limits of agreement = 1.4/-1.6%), respectively. These correspond to CR of 1.3 and 1.5% for MOLLI and AIR, respectively.

5.4 Discussion

In this study, we evaluated, in well-controlled canine and pig experiments, the relative accuracy and precision, as well as intra- and inter-observer variability in data analysis, of T_1 and ECV measured with AIR as compared with MOLLI. Canine experiments showed that MOLLI and AIR yield significantly different T_1 and ECV values ($p < 0.001$), which have important implications (see below). Both intra- and inter-observer agreements in T_1 calculations were higher for MOLLI than AIR, owing to the fact that MOLLI acquires 9 more images than AIR. Interestingly, both intra- and inter-observer agreements in ECV calculations were similar between MOLLI and AIR, possibly owing to off-setting errors when calculating ECV from multiple measurements (native and post-contrast myocardial and blood T_1s). Pig experiments showed that MOLLI yields higher precision than AIR, which was expected since AIR acquires 9 less images than MOLLI.

Our observation has important implications for the CMR community. Currently, there are several different variants of inversion-recovery (10,11) and saturation-recovery (12-14,16) based cardiac T_1 mapping pulse sequences, as well as a hybrid inversion- and saturation-recovery cardiac T_1 mapping pulse sequence (17) and the "TI" scout sequence (18), which is commonly used in conjunction with late gadolinium enhanced MRI (36,37). These different pulse sequences may yield not only different T_1 measurements

but also ECV measurements, as reported in this study. This implies that CMR researchers must consider the specific pulse sequence when translating published ECV cutoff values into their own studies. It also implies that the CMR community must work towards standardizing cardiac T_1 and ECV mapping protocols, in order to move the field forward and increase reproducibility. The 2013 Society for Cardiovascular Magnetic Resonance and CMR Working Group of the European Society of Cardiology consensus statement (38) is one important step in the right direction towards protocol standardization.

This study has several limitations worth noting. First, we did not test different variants of MOLLI (34,39), because our group has the most experience with the original version of MOLLI (i.e., 3-3-5) that was provided by Siemens. Another study is warranted to test the performance of different variants of MOLLI. Second, we did not compare other inversion-recovery and saturation-recovery based cardiac T_1 mapping pulse sequences (11-14,17,18,40). Therefore, our observations may not be directly applicable for other pulse sequences not evaluated in this study. Our study adds to the growing list of studies which compare the performances of different cardiac T_1 mapping pulse sequences (11,15,19,41,42). Third, the canines included in this study had a mean heart rate of 98.8 bpm, and pigs had a mean heart rate of 78.1 bpm. This implies that our observation may not be directly applicable for different heart rates and rhythm conditions. Fourth, the animals in this study did not have a prior history of heart disease (assumed to have normal myocardium and supported by ECV measurements). Therefore, our observations may not be directly applicable for hearts with focal and/or diffuse cardiac fibrosis, which changes post-contrast myocardial T_1 and ECV values. Fifth, this study did not compare the accuracy of ECV measurements by MOLLI and AIR to

histologic quantification of collagen volume fraction. A future study including comprehensive histologic evaluation is warranted to compare the accuracy of ECV measurements between MOLLI and AIR.

5.5 Conclusions

This study shows that MOLLI and AIR yield significantly different T_1 and ECV values in large animals and that MOLLI yields higher precision than AIR. Both intra- and inter-observer agreements in calculation of T_1 were higher for MOLLI than AIR, but intra- and inter-observer agreements in calculation of ECV were similar between MOLLI and AIR. Findings from this study suggest that CMR researchers must consider the specific pulse sequence when translating published ECV cutoff values into their own studies.

5.6 References

1. Iles L, Pfluger H, Phrommintikul A, Cherayath J, Aksit P, Gupta SN, Kaye DM, Taylor AJ. Evaluation of diffuse myocardial fibrosis in heart failure with cardiac magnetic resonance contrast-enhanced T1 mapping. J Am Coll Cardiol 2008;52(19):1574-1580.

2. Sibley CT, Noureldin RA, Gai N, Nacif MS, Liu S, Turkbey EB, Mudd JO, van der Geest RJ, Lima JA, Halushka MK, Bluemke DA. T1 mapping in cardiomyopathy at cardiac MR: comparison with endomyocardial biopsy. Radiology 2012;265(3):724-732.

3. Messroghli DR, Nordmeyer S, Dietrich T, Dirsch O, Kaschina E, Savvatis K, D Oh-I, Klein C, Berger F, Kuehne T. Assessment of diffuse myocardial fibrosis in rats using small-animal Look-Locker inversion recovery T1 mapping. Circ Cardiovasc Imaging 2011;4(6):636-640.

4. Miller CA, Naish JH, Bishop P, Coutts G, Clark D, Zhao S, Ray SG, Yonan N, Williams SG, Flett AS, Moon JC, Greiser A, Parker GJ, Schmitt M. Comprehensive validation of cardiovascular magnetic resonance techniques for

the assessment of myocardial extracellular volume. Circ Cardiovasc Imaging 2013;6(3):373-383.

5. Flett AS, Hayward MP, Ashworth MT, Hansen MS, Taylor AM, Elliott PM, McGregor C, Moon JC. Equilibrium contrast cardiovascular magnetic resonance for the measurement of diffuse myocardial fibrosis: preliminary validation in humans. Circulation 2010;122(2):138-144.

6. Kehr E, Sono M, Chugh SS, Jerosch-Herold M. Gadolinium-enhanced magnetic resonance imaging for detection and quantification of fibrosis in human myocardium in vitro. Int J Cardiovasc Imaging 2008;24(1):61-68.

7. Jerosch-Herold M, Sheridan DC, Kushner JD, Nauman D, Burgess D, Dutton D, Alharethi R, Li D, Hershberger RE. Cardiac magnetic resonance imaging of myocardial contrast uptake and blood flow in patients affected with idiopathic or familial dilated cardiomyopathy. Am J Physiol Heart Circ Physiol 2008;295(3):H1234-H1242.

8. White SK, Sado DM, Fontana M, Banypersad SM, Maestrini V, Flett AS, Piechnik SK, Robson MD, Hausenloy DJ, Sheikh AM, Hawkins PN, Moon JC. T1 mapping for myocardial extracellular volume measurement by CMR: bolus only versus primed infusion technique. JACC Cardiovascular Imaging 2013;6(9):955-962.

9. Kramer CM, Chandrashekhar Y, Narula J. T1 mapping by CMR in cardiomyopathy: a noninvasive myocardial biopsy? JACC Cardiovascular Imaging 2013;6(4):532-534.

10. Messroghli DR, Radjenovic A, Kozerke S, Higgins DM, Sivananthan MU, Ridgway JP. Modified Look-Locker inversion recovery (MOLLI) for high-resolution T1 mapping of the heart. Magn Reson Med 2004;52(1):141-146.

11. Piechnik SK, Ferreira VM, Dall'Armellina E, Cochlin LE, Greiser A, Neubauer S, Robson MD. Shortened Modified Look-Locker Inversion recovery (ShMOLLI) for clinical myocardial T1-mapping at 1.5 and 3 T within a 9 heartbeat breathhold. J Cardiovasc Magn Reson 2010;12:69.

12. Song T, Stainsby JA, Ho VB, Hood MN, Slavin GS. Flexible cardiac T1 mapping using a modified Look-Locker acquisition with saturation recovery. Magn Reson Med 2012;67(3):622-627.

13. Slavin GS HM, Ho VB, Stainsby JA. Breath-held myocardial T1 mapping using multiple single-point saturation recovery. In Proceedings of the 20th Annual Meeting of ISMRM, Melbourne, Australia, 2012. p. 1244.

14. Slavin G, Stainsby J. True T1 mapping with SMART1Map (saturation method using adaptive recovery times for cardiac T1 mapping): a comparison with MOLLI. In Proceedings of the 16th Annual Meeting of SCMR Scientific Sessions 2013, San Francisco, CA, USA. P3.

15. Fitts M, Breton E, Kholmovski EG, Dosdall DJ, Vijayakumar S, Hong KP, Ranjan R, Marrouche NF, Axel L, Kim D. Arrhythmia insensitive rapid cardiac T1 mapping pulse sequence. Magn Reson Med 2013;70(5):1274-1282.

16. Chow K, Flewitt JA, Green JD, Pagano JJ, Friedrich MG, Thompson RB. Saturation recovery single-shot acquisition (SASHA) for myocardial T1 mapping. Magn Reson Med 2013.

17. Weingartner S, Akcakaya M, Basha T, Kissinger KV, Goddu B, Berg S, Manning WJ, Nezafat R. Combined saturation/inversion recovery sequences for improved evaluation of scar and diffuse fibrosis in patients with arrhythmia or heart rate variability. Magn Reson Med 2013.

18. Gupta A, Lee VS, Chung YC, Babb JS, Simonetti OP. Myocardial infarction: optimization of inversion times at delayed contrast-enhanced MR imaging. Radiology 2004;233(3):921-926.

19. Robson MD, Piechnik SK, Tunnicliffe EM, Neubauer S. T1 measurements in the human myocardium: The effects of magnetization transfer on the SASHA and MOLLI sequences. Magn Reson Med 2013.

20. Gai N, Stehning C, Nacif M, Bluemke D. Modified Look-Locker T1 evaluation using Bloch simulations: human and phantom validation. Magn Reson Med 2012;DOI: 10.1002/mrm.24251.

21. Chow K, Flewitt JA, Pagano JJ, Green JD, Friedrich MG, Thompson RB. MOLLI T_1 values have systematic T_2 and inversion efficiency dependent errors. In Proceedings of the 20th Annual Meeting of ISMRM, Melbourne, Australia, 2012. p. 395.

22. Kellman P, Herzka DA, Hansen MS. Adiabatic inversion pulses for myocardial T1 mapping. Magn Reson Med 2014;71(4):1428-1434.

23. Kampf T, Helluy X, Gutjahr FT, Winter P, Meyer CB, Jakob PM, Bauer WR, Ziener CH. Myocardial perfusion quantification using the T1-based FAIR-ASL method: the influence of heart anatomy, cardiopulmonary blood flow and look-locker readout. Magn Reson Med 2014;71(5):1784-1797.

24. Kim D, Oesingmann N, McGorty K. Hybrid adiabatic-rectangular pulse train for effective saturation of magnetization within the whole heart at 3 T. Magn Reson Med 2009;62(6):1368-1378.

25. Hong K, Kholmovski EG, McGann CJ, Ranjan R, Kim D. Comparison of ECV measurements during equilibrium between IR- and SR-based cardiac T1 mapping. J Cardiovasc Magn Reson 2014;16(Suppl 1):P53.

26. Hong KP, Kholmovski EG, McGann CJ, Ranjan R, Kim D. Comparison of canine ECV measurements derived from CMR: bolus injection vs. slow infusion of Gd-BOPTA. J Cardiovasc Magn Reson 2014;16(Suppl 1):P64.

27. Koopmann M, Hong K, Kholmovski EG, Huang EC, Hu N, Ying J, Levenson R, Vijayakumar S, Dosdall DJ, Ranjan R, Kim D. Post-contrast myocardial T1 and ECV disagree in a longitudinal canine study. NMR Biomed 2014;27(8):988-995.

28. Kellman P, Wilson JR, Xue H, Bandettini WP, Shanbhag SM, Druey KM, Ugander M, Arai AE. Extracellular volume fraction mapping in the myocardium, part 2: initial clinical experience. J Cardiovasc Magn Reson 2012;14:64.

29. Ugander M, Oki AJ, Hsu LY, Kellman P, Greiser A, Aletras AH, Sibley CT, Chen MY, Bandettini WP, Arai AE. Extracellular volume imaging by magnetic resonance imaging provides insights into overt and sub-clinical myocardial pathology. Eur Heart J 2012;33(10):1268-1278.

30. Brouwer WP, Baars EN, Germans T, de Boer K, Beek AM, van der Velden J, van Rossum AC, Hofman MB. In-vivo T1 cardiovascular magnetic resonance study of diffuse myocardial fibrosis in hypertrophic cardiomyopathy. J Cardiovasc Magn Reson 2014;16(1):28.

31. Kellman P, Hansen MS. T1-mapping in the heart: accuracy and precision. J Cardiovasc Magn Reson 2014;16(1):2.

32. Griswold MA, Jakob PM, Heidemann RM, Nittka M, Jellus V, Wang J, Kiefer B, Haase A. Generalized autocalibrating partially parallel acquisitions (GRAPPA). Magn Reson Med 2002;47(6):1202-1210.

33. Bieri O, Markl M, Scheffler K. Analysis and compensation of eddy currents in balanced SSFP. Magn Reson Med 2005;54(1):129-137.

34. Messroghli DR, Greiser A, Frohlich M, Dietz R, Schulz-Menger J. Optimization and validation of a fully-integrated pulse sequence for modified look-locker inversion-recovery (MOLLI) T1 mapping of the heart. JMRI 2007;26(4):1081-1086.

35. Arheden H, Saeed M, Higgins CB, Gao DW, Bremerich J, Wyttenbach R, Dae MW, Wendland MF. Measurement of the distribution volume of gadopentetate dimeglumine at echo-planar MR imaging to quantify myocardial infarction: comparison with 99mTc-DTPA autoradiography in rats. Radiology 1999;211(3):698-708.

36. Kim RJ, Fieno DS, Parrish TB, Harris K, Chen EL, Simonetti O, Bundy J, Finn JP, Klocke FJ, Judd RM. Relationship of MRI delayed contrast enhancement to irreversible injury, infarct age, and contractile function. Circulation 1999;100(19):1992-2002.

37. Kim RJ, Wu E, Rafael A, Chen EL, Parker MA, Simonetti O, Klocke FJ, Bonow RO, Judd RM. The use of contrast-enhanced magnetic resonance imaging to identify reversible myocardial dysfunction. N Engl J Med 2000;343(20):1445-1453.

38. Moon JC, Messroghli DR, Kellman P, Piechnik SK, Robson MD, Ugander M, Gatehouse PD, Arai AE, Friedrich MG, Neubauer S, Schulz-Menger J, Schelbert EB. Myocardial T1 mapping and extracellular volume quantification: a Society for Cardiovascular Magnetic Resonance (SCMR) and CMR Working Group of the European Society of Cardiology consensus statement. J Cardiovasc Magn Reson 2013;15(1):92.

39. Kellman P, Wilson JR, Xue H, Ugander M, Arai AE. Extracellular volume fraction mapping in the myocardium, part 1: evaluation of an automated method. J Cardiovasc Magn Reson 2012;14:63.

40. Chow K, Flewitt JA, Green JD, Pagano JJ, Friedrich MG, Thompson RB. Saturation recovery single-shot acquisition (SASHA) for myocardial T1 mapping. Magn Reson Med 2014;71(6):2082-2095.

41. Nacif MS, Turkbey EB, Gai N, Nazarian S, van der Geest RJ, Noureldin RA, Sibley CT, Ugander M, Liu S, Arai AE, Lima JA, Bluemke DA. Myocardial T1 mapping with MRI: comparison of look-locker and MOLLI sequences. JMRI 2011;34(6):1367-1373.

42. Roujol S, Weingartner S, Foppa M, Chow K, Kawaji K, Ngo LH, Kellman P, Manning WJ, Thompson RB, Nezafat R. Accuracy, precision, and reproducibility of four T1 mapping sequences: a head-to-head comparison of MOLLI, ShMOLLI, SASHA, and SAPPHIRE. Radiology 2014:140296.

Table 5.1. Pair-wise t-test statistics comparing the different subgroups of T_1 derived from MOLLI and AIR cardiac T_1 mapping pulse sequences: native myocardial T_1, native blood T_1, post-contrast myocardial T_1, and post-contrast blood T_1. T_1 value represents mean ± standard deviation.

Tissue Type	MOLLI	AIR	*p*-value
Native myocardial T_1	1047.0 ± 21.3 ms	1345.2 ± 55.1 ms	< 0.0001
Native blood T_1	1407.7 ± 57.5 ms	1724.7 ± 68.5 ms	< 0.0001
Post-contrast myocardial T_1	659.0 ± 50.1 ms	768.0 ± 42.0 ms	< 0.0001
Post-contrast blood T_1	452.1 ± 64.1 ms	444.0 ± 41.1 ms	0.55

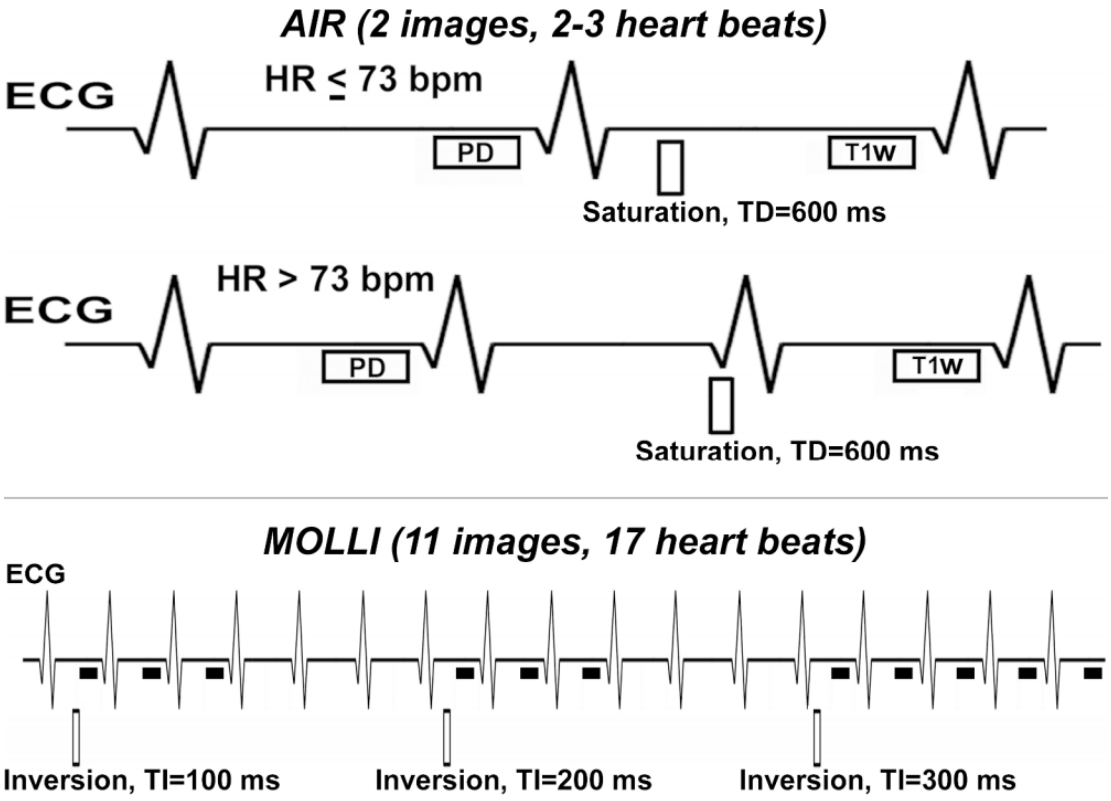

Figure 5.1. Schematic of AIR (top row) and (bottom) MOLLI cardiac T_1 mapping pulse sequences. AIR acquires one proton density and one T_1-weighted image in succession with scan time of 2-3 heart beats, depending on heart rate as shown. MOLLI acquires 11 images with scan time of 17 heart beats, following three inversion pulses as shown (i.e., 3-3-5).

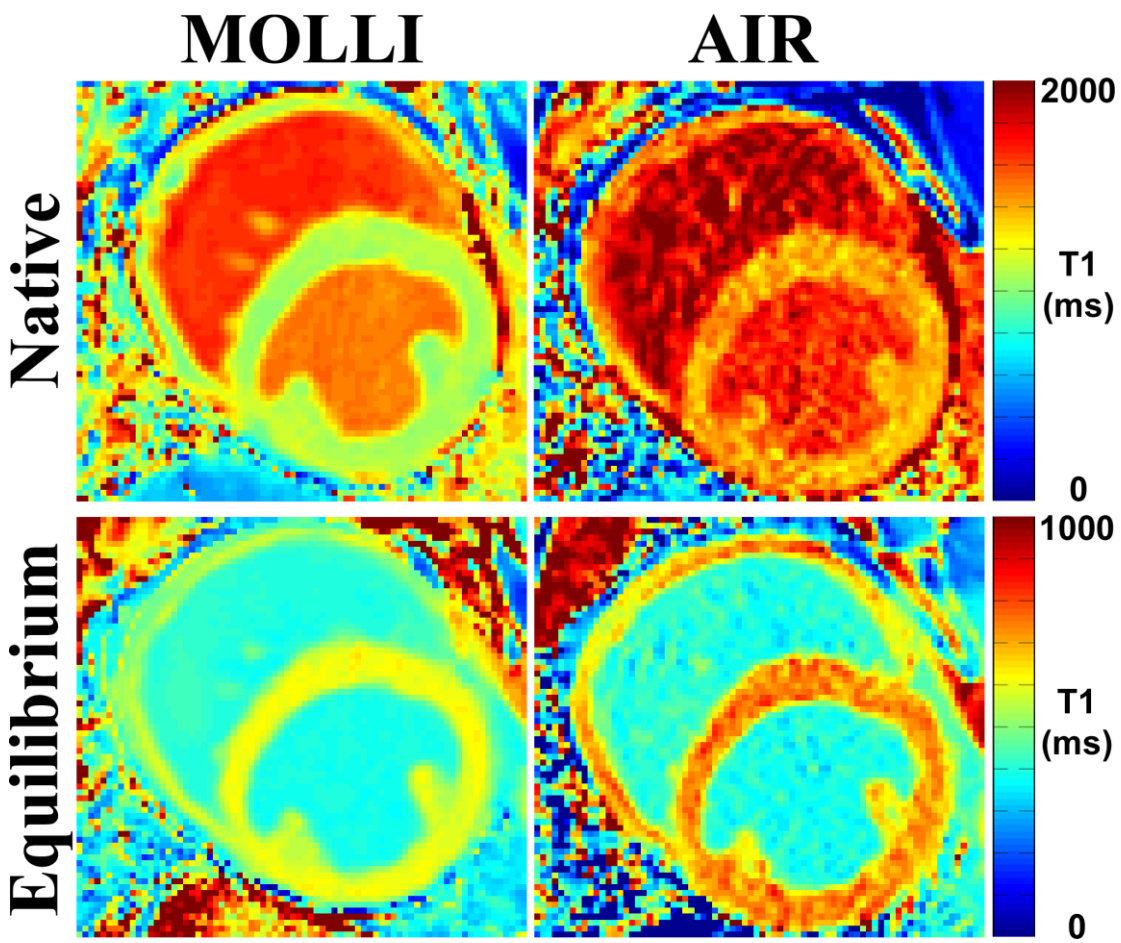

Figure 5.2. Representative cardiac T_1 maps of one dog (heart rate = 94.5 bpm) acquired with MOLLI (left) and AIR (right) cardiac T_1 mapping pulse sequences: native (top row) and post-contrast (bottom row). These examples illustrate typical image quality produced by MOLLI and AIR. Compared with AIR T_1 maps derived from only 2 images, MOLLI T_1 maps derived from 11 images exhibited higher overall SNR. Native myocardial and blood T_1 values were different (native myocardial T_1 was 1074.1 ms (MOLLI) and 1373.4 ms (AIR); native blood T_1 was 1492.7 ms (MOLLI) and 1692.9 ms (AIR). Post-contrast myocardial T_1 was also different (605.5 ms [MOLLI] and 724.5 ms [AIR]), but post-contrast blood T_1 was not different (389.2 ms [MOLLI] and 384.8 ms [AIR]). These differences in T_1 resulted in discordant ECV measurements (22.0% and 18.8% for MOLLI and AIR, respectively).

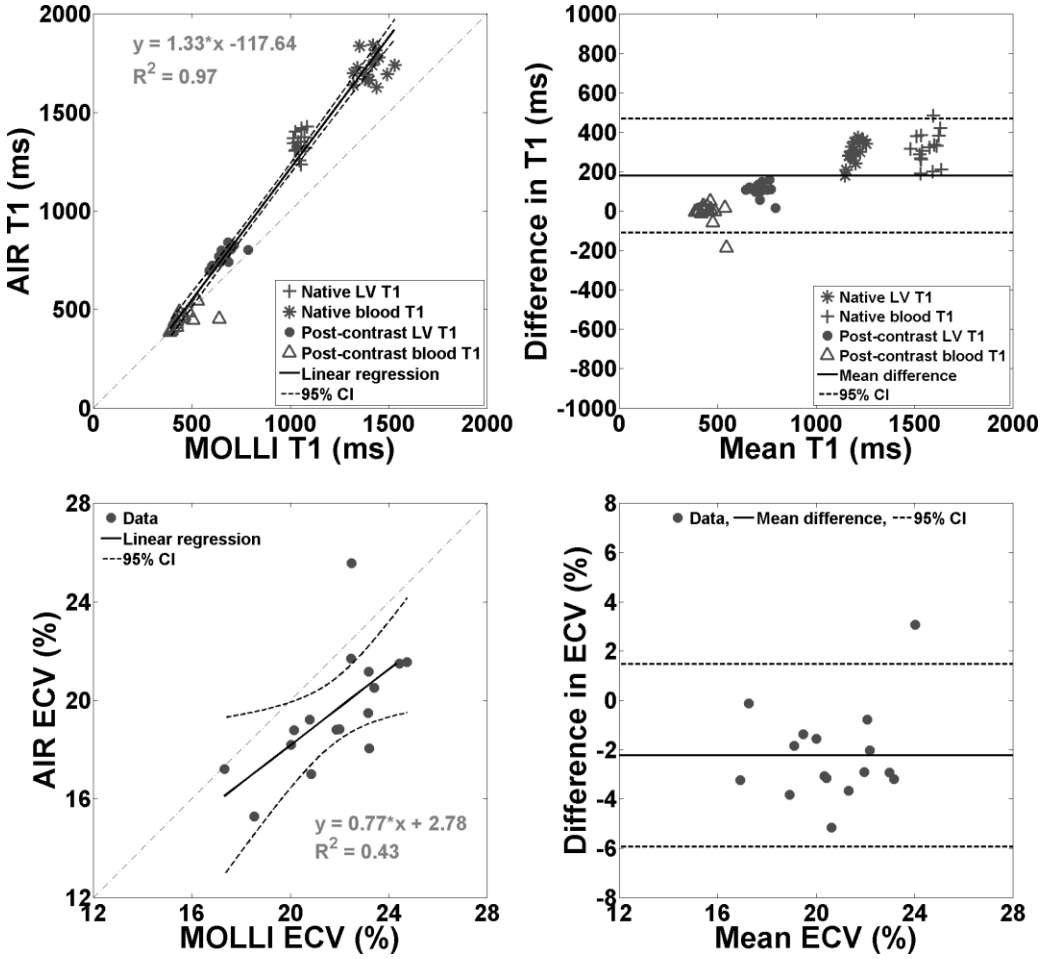

Figure 5.3. Scatter plots representing linear regression (left column) and Bland-Altman (right column) analyses: T_1 (top row) and ECV (bottom row) derived from MOLLI and AIR cardiac T_1 mapping pulse sequences in 16 dogs. According to the linear regression and concordance correlation analyses, T_1 values were strongly correlated (Pearson's correlation coefficient = 0.99, slope = 1.33, bias = -117.6 ms, $p <$ 0.0001; concordance correlation coefficient = 0.87). According to the Bland-Altman analysis, the mean difference in T_1 was 179 ms (± 95% confidential interval (CI) = 468/-109 ms), which corresponds to 18% of the mean T_1 value (981 ms). For ease of interpretation, the Bland-Altman plot for T_1 was displayed with y-axis ranging from -1000 to 1000 ms (i.e., approximately -100 to 100 % of the mean value of 981 ms). According to the linear regression analysis, ECV values derived were moderately correlated (Pearson's correlation coefficient = 0.65, slope = 0.77, bias = 2.8%, $p <$ 0.001). According to the concordance correlation analysis, ECV values were weakly correlated (correlation coefficient = 0.43). According to the Bland-Altman analysis, the mean difference in ECV was -2.2% (± 95% CI = 1.5/-5.9%), which corresponds to 10.8% of the mean ECV value (20.7%). For ease of interpretation, the Bland-Altman plot for ECV was displayed with y-axis ranging from -8 to 8% (i.e., approximately -40 to 40 % of the mean value of 20.7%). Difference defined as AIR - MOLLI.

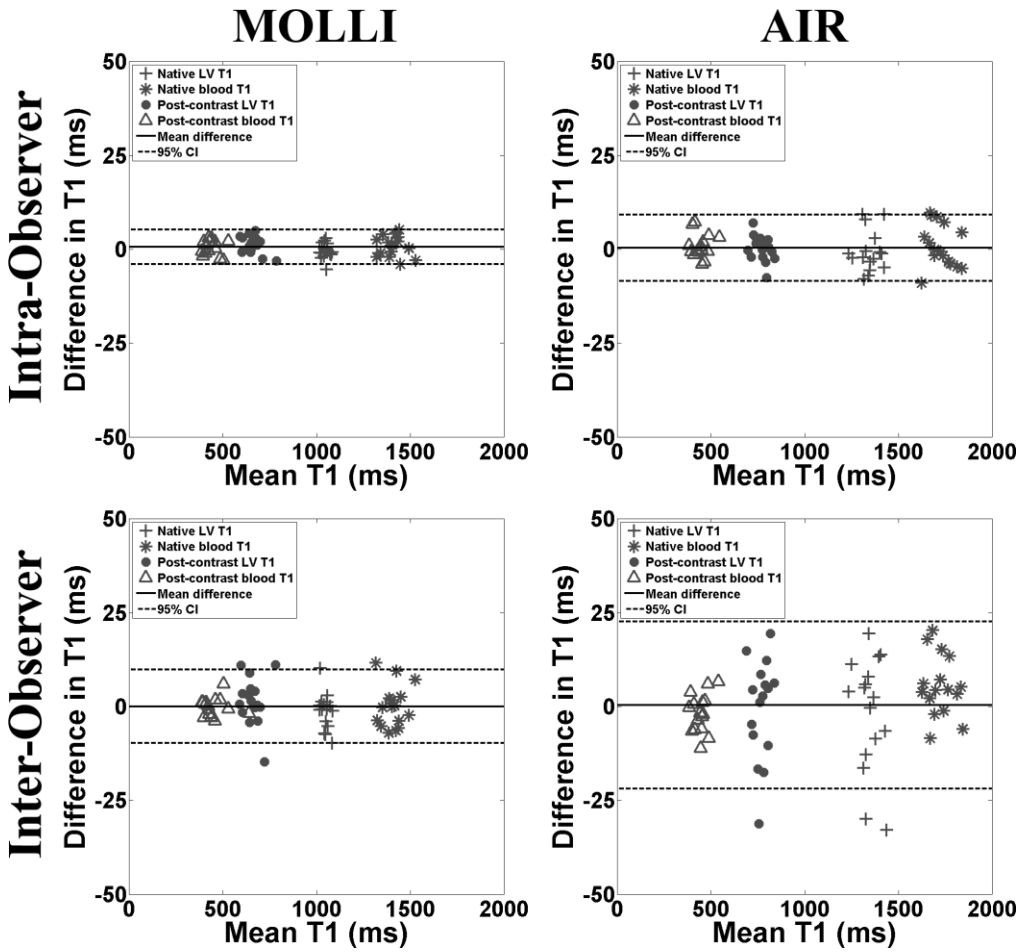

Figure 5.4. Scatter plots representing the intra- (top row) and inter-observer (bottom row) agreements in calculation of T_1 derived from MOLLI (left column) and AIR (right column) data sets. For intra-observer agreement, the mean difference in T_1 was 0.6 ms (upper/lower 95% limits of agreement = 5.3/-4.0 ms) and 0.4 ms (upper/lower 95% limits of agreement = 9.2/-8.5 ms) for MOLLI and AIR, respectively. For inter-observer agreement, the mean difference in T_1 was 0.009 ms (upper/lower 95% limits of agreement = 9.8/-9.8 ms) and 0.4 ms (upper/lower 95% limits of agreement = 22.7/-21.9 ms) for MOLLI and AIR, respectively. Note that CR was lower MOLLI than AIR, suggesting higher overall SNR for MOLLI than AIR. For ease of interpretation, the Bland-Altman plots were displayed with y-axis ranging from -50 to 50 ms (i.e., approximately -5 to 5 % of the mean value of 1000 ms). Solid and dotted lines represent the mean difference and 95% confidence intervals, respectively.

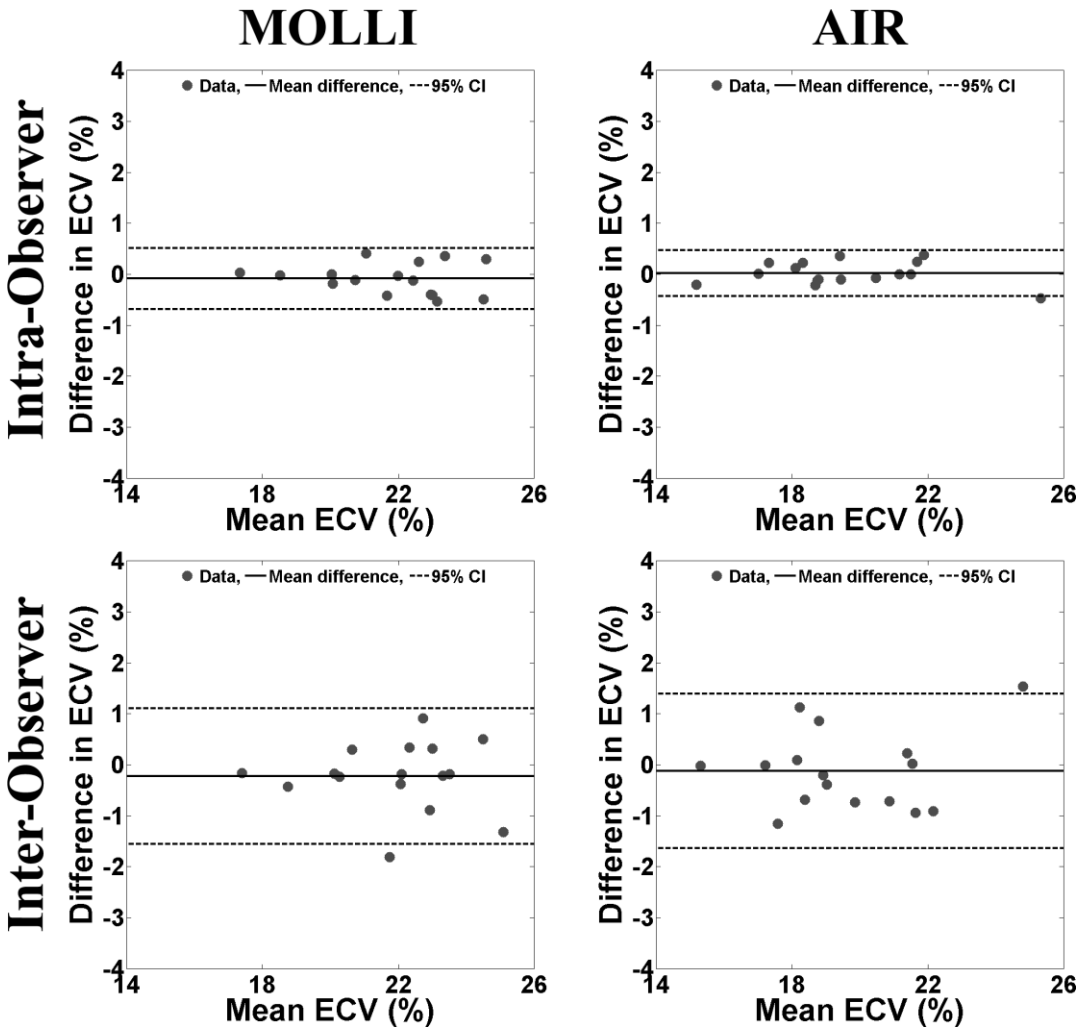

Figure 5.5. Scatter plots representing the intra- (top row) and inter-observer (bottom row) agreements in calculation of ECV derived from MOLLI (left column) and AIR (right column) data sets. For intra-observer agreement, the mean difference in ECV was -0.09% (upper/lower 95% limits of agreement = 0.5/-0.7%) and 0.02% (upper/lower 95% limits of agreement = 0.5/-0.4%) for MOLLI and AIR, respectively. For inter-observer agreement, the mean difference in ECV was -0.2% (upper/lower 95% limits of agreement = 1.1/-1.6%) and -0.1% (upper/lower 95% limits of agreement = 1.4/-1.6%) for MOLLI and AIR, respectively. Note that CR was similar between MOLLI and AIR, possibly due to off-setting errors from multiple measurements. For ease of interpretation, the Bland-Altman plots were displayed with y-axis ranging from -4 to 4% (i.e., approximately -20 to 20 % of the mean value of 20%). Solid and dotted lines represent the mean difference and 95% confidence intervals, respectively.

CHAPTER 6

WIDEBAND AIR CARDIAC T_1 MAPPING PULSE SEQUENCE

This chapter describes the development of a new wideband AIR cardiac T_1 mapping pulse sequence for imaging patients with an implantable defibrillator. This work was published in *"Wideband Arrhythmia-Insensitive-Rapid (AIR) Pulse Sequence for Cardiac T_1 Mapping without Image Artifacts Induced by an Implantable-Cardioverter-Defibrillator" Magnetic Resonance in Medicine 2015, Volume 74, Issue 2, Pages 336-345*. Reprinted with permission from Wiley Periodicals, Inc.

6.1 Introduction

Heart failure (HF) is a major healthcare problem that affects over 5 million Americans (1). Patients with advanced or end-stage HF (i.e., stage D according to the ACCF/AHA classification (2)) are characterized by marked symptoms at rest despite maximal medical therapy (3); consequently, they have a 1-year mortality rate of approximately 40-50% (4,5). While heart transplantation is a well-established treatment for improving both survival and quality of life for these patients (6), from healthcare's perspective, it is unsustainable due to a continuing shortage of donor hearts (7). To address this imbalance, the 2013 ACC/AHA guideline (2) recommends left ventricular (LV) assist device (LVAD)(8-11) as a destination therapy (12,13) in select patients.

Unfortunately, current clinical risk scores and profiles provide poor discrimination between responders and non-responders to LVAD therapy.

Cardiac fibrosis, as a marker of adverse structural remodeling, is a strong predictor of functional response to intervention (14). While myocardial biopsy is the current gold standard for assessment of fibrosis, it is rarely indicated due to its associated non-negligible risk of complications and susceptibility to sampling errors. MRI is emerging as a reliable non-invasive test for myocardial biopsy (15) using cardiac T_1 mapping (16-18) or extracellular volume (ECV) fraction (18-24) mapping pulse sequences. Unlike myocardial biopsy, these MRI methods provide a means to sample the whole heart non-invasively. In the context of HF induced by non-ischemic cardiomyopathy, cardiac T_1 and ECV fraction mapping pulse sequences may be better than late gadolinium-enhanced (LGE) MRI for quantification of myocardial fibrosis burden.

Because LVAD candidates (i.e., end-stage HF) typically have prophylactic implantable cardioverter-defibrillator (ICD) for prevention of sudden cardiac death and/or arrhythmia, a new pulse sequence needs to be developed to reduce measurement error due to ICD and/or arrhythmia. Despite the fact that MRI can be performed safely in most patients with cardiac devices at 1.5T (25,26), many patients who would derive benefit from MRI do not undergo MRI largely due to image artifacts arising from the ICD generator. Recently, the feasibility of wideband LGE MRI was demonstrated for assessment of focal fibrosis in patients with ICD (27-29), where "wideband" refers to the modified hyperbolic secant radio-frequency (RF) pulse used to invert the magnetization in the presence of ICD. To our knowledge, no other study has reported successful cardiac T_1 mapping without image artifacts induced by ICD.

Among the different cardiac T_1 mapping pulse sequences, an arrhythmia-insensitive-rapid (AIR) cardiac T_1 mapping pulse sequence (30) with a short scan time (~2-3 heart beats) is well suited for imaging patients with advanced HF, because they often have rapid heart rates and/or irregular heart rhythm and/or limited breath-hold capacity. In this study, we will extend AIR cardiac T_1 mapping to be insensitive to ICD, by incorporating a saturation RF pulse with wide frequency bandwidth to achieve uniform T_1 weighting in the heart with ICD. We demonstrate the feasibility of wideband AIR cardiac T_1 mapping and evaluate its relative accuracy in phantom and human experiments at 1.5T.

6.2 Methods

6.2.1 Saturation pulse modules

As previously described in (30), the original AIR cardiac T_1 mapping pulse sequence was implemented with balanced steady-state free precession (b-SSFP) readout. This pulse sequence acquires two single-shot images, T_1-weighted and proton density (PD), within a scan time of 2-3 cardiac cycles, depending on heart rate. To minimize image artifacts induced by ICD and enable successful imaging of patients with ICD implantation, we modified the original AIR pulse sequence to use ultra-fast gradient echo (TurboFLASH in Siemens; FastSPGR in GE; TFE in Philips) readout. We used the vendor's saturation pulse module for original AIR, which is comprised of three 90° rectangular pulses with 0.5 ms duration for each rectangular RF pulse (see Figure 1A in (31)). We used this modified AIR pulse sequence (i.e., TurboFLASH readout + vendor saturation pulse module) as a reference to compare the wideband AIR pulse sequence described below. For clarity, we refer to this modified AIR as original AIR throughout this report.

ICD generator is typically implanted on the patient's left shoulder, approximately 5-10 cm away from the heart. This distance will induce a center frequency shift as large as 2-6 kHz (27). Standard saturation pulse modules have relatively low frequency bandwidth and, therefore, are unsuitable for complete saturation of magnetization in the presence of ICD. This means that an effective saturation RF pulse for wideband AIR cardiac T_1 mapping in patients with ICD should have a frequency bandwidth greater than 6 kHz to achieve uniform T_1 weighting. One promising RF pulse module that can effectively saturate the magnetization over a wide range of frequencies is RF field (B_1) insensitive train to obliterate signal (BISTRO)(32), which was originally developed for outer volume suppression in inhomogeneous B_1. The primary concept behind BISTRO is to not meet the adiabatic condition on purpose for each individual inversion RF pulse (i.e., < 180° excitation per pulse), but ultimately fully rotate the longitudinal magnetization (M_z) onto the transverse plane (i.e., net excitation equal to 90°) with a train of sub-optimal inversion RF pulses, where key design considerations are the number of pulses, frequency bandwidth, total pulse duration, and specific absorption rate (SAR). Figure 6.1 shows the pulse sequence diagram of BISTRO that was incorporated into AIR. See Appendix for more details on our implementation of BISTRO. For clarity, AIR with BISTRO is referred to as wideband AIR throughout this report.

6.2.2 Calculation of RF energy deposition by the saturation pulse modules

Using the pulse sequence simulator (IDEA, Siemens Healthcare, Erlangen, Germany), we calculated the transmit RF energy for each saturation pulse module, assuming that the RF voltage needed to achieve B_1+ (normalized by gyromagnetic ratio)

of 500 Hz is 300-350 V. This RF calibration assumption at 1.5T is consistent with results reported in (33). Nominal B_1+ (normalized by gyromagnetic ratio) is 500 Hz (300-350 V) for the original saturation pulse module, whereas nominal B_1+ (normalized by gyromagnetic ratio) is 926 Hz (556-648 V) for the wideband saturation pulse module. Note the RF amplifier of our Siemens Espree system delivers a maximum voltage of 949 V. At these settings, theoretically calculated transmit RF energy of original and wideband saturation pulse modules was 3.7 and 101.0 J, respectively. These energy deposition values translate to whole-body SAR of approximately 0.125 and 0.5 W/kg for original and wideband AIR T_1 mapping acquisitions, respectively, depending on subject size. We note that this SAR calculation includes saturation pulse and RF excitations for PD and T_1-weighted image acquisitions. This theoretical analysis confirms that whole-body SAR induced by wideband AIR is 3-4 times lower than the safe limits (1.5-2 W/kg) recommended by established pacemaker/ICD MRI protocols at 1.5T (25,26).

6.2.3 Calculation of frequency bandwidth of the saturation pulse modules

We determined empirically, in a phantom positioned near magnet isocenter, frequency bandwidth of the original and wideband saturation pulse modules. Compared with original AIR, wideband AIR had 256% higher frequency bandwidth (full width at half maximum [FWHM] = 2.5 kHz and 8.9 kHz for original and wideband, respectively). For more details on the methods and results, see 6.5 Supplementary Materials and Figure 6.2A. This experimental analysis confirms that wideband AIR is insensitive to center frequency shift expected with ICD located 5-10 cm away from the heart.

6.2.4 MRI protocol

The original and wideband AIR cardiac T_1 mapping pulse sequences were implemented on a 1.5T whole-body MRI scanner (Espree, Siemens Healthcare, Erlangen, Germany), equipped with a gradient system capable of achieving a maximum gradient strength of 33 mT/m and a slew rate of 100 T/m/s. RF excitation was performed using the body coil, and an 8-element coil array was used for signal reception.

Both original and wideband AIR pulse sequences used the following relevant imaging parameters: field of view = 360 mm × 270 mm (phase-encoding), acquisition matrix = 128 × 96 (phase-encoding), in-plane resolution = 2.8 mm × 2.8 mm, slice thickness = 8 mm, echo time (TE) = 1.1 ms (asymmetric readout), repetition time (TR) = 2.2 ms, receiver bandwidth = 1000 Hz/pixel, center-out k-space ordering, readout duration = 132 ms, saturation-recovery time delay (TD) = 600 ms, flip angle = 10°, breath-hold duration = 2-3 heart beats, and generalized autocalibrating partially parallel acquisitions (GRAPPA)(34) with an acceleration factor = 1.6 (including reference lines). Note that in center-out k-space ordering the first RF excitation is used to acquire the origin of k-space. This acquisition scheme minimizes the sensitivity to excitation angle variation (35,36) and enables straight-forward calculation of T_1 using the Bloch equation describing ideal saturation-recovery, as previously described (30).

6.2.5 Experiment 1: Evaluation of sensitivity to ICD and intracardiac leads in phantom

We evaluated the performance of original and wideband AIR pulse sequences with and without an ICD generator (Vitality AVT Model A155, GUIDANT Boston Scientific, Natick, Massachusetts) taped to one side of the phantom as shown in Figure 6.3. We

performed T_1 mapping in a coronal plane with the ICD in the plane, in order to visualize the effectiveness of the saturation pulse modules as a function of ICD distance. We also performed a static magnetic field (B_0) mapping acquisition (i.e., double echo with TE difference = 4.76 ms) with matching spatial resolution as T_1 mapping. For cases with ICD, the B_0 maps were generated after performing phase unwrapping based on network programming (37). The same experiment was repeated with intracardiac leads attached to the same location. In this experiment, original AIR cardiac T_1 mapping without ICD was used as the control.

6.2.6 Experiment 2: Evaluation of accuracy in $MnCl_2$ phantoms with ICD

We tested the performance of original and wideband AIR cardiac T_1 mapping pulse sequences in phantoms with clinically relevant T_1 and T_2 values positioned near magnet isocenter. Specifically, we imaged five phantoms with different concentrations of manganese (II) chloride ($MnCl_2$) in distilled water (see Table 1 for the concentration and reference T_1 and T_2 values). $MnCl_2$ was chosen because it has $T_1/T_2 \approx 10$ at 1.5 T (38), which is comparable to that of tissues.

Reference T_1 values were measured using an inversion-recovery fast spin echo (IR-FSE) pulse sequence; the resulting data were analyzed using a 2-parameter fit of the mono-exponential signal relaxation, solving for equilibrium signal amplitude and T_1. The relevant imaging parameters for IR-FSE include: same spatial resolution as AIR, excitation flip angle = 90º, refocusing flip angle = 180°, TE = 6 ms, TR = 20 s (> 5 T_1s), receiver bandwidth = 501 Hz/pixel, turbo factor = 7, and number of images = 16. The inversion times were 100, 200, 300, 400, 500, 600, 700, 800, 1000, 1100, 1200, 1500,

1800, 2300, 2700, and 20000 ms.

For comparison, we also performed 3-3-5 modified Look-Locker inversion recovery (MOLLI)(39) with b-SSFP readout and heart rate simulated to 60 beats per minute. The relevant imaging parameters for 3-3-5 MOLLI include: same spatial resolution as AIR, scan time = 17 heart beats, flip angle = 35º, TE = 1.1 ms, TR = 2.6 ms, receiver bandwidth = 930 Hz/pixel, and inversion times and linear k-space ordering as previously described (39).

Reference T_2 values were measured using a multi-echo fast spin echo (ME-FSE) pulse sequence (40); the resulting data were analyzed using a 3-parameter fit of the mono-exponential signal relaxation, solving for initial signal amplitude, T_2, mean background noise. The relevant imaging parameters for ME-FSE include: same spatial resolution as AIR, excitation flip angle = 90º, refocusing flip angle = 180°, TR = 20 s (> 5 T_1s), receiver bandwidth = 501 Hz/pixel, turbo factor = 2, inter-echo spacing = 4.7 ms, inter-image spacing = 9.4 ms, and number of images = 12. The image echo times were 9.4, 19, 28, 38, 47, 57, 66, 76, 85, 95, 104, and 113 ms.

For each phantom vial, with the ICD generator taped 10 cm away from the phantom vial (through-plane direction), we performed original and wideband AIR T_1 mapping acquisitions. This experiment was repeated without ICD for completeness.

6.2.7 Experiment 3: Evaluation of accuracy in $MnCl_2$ phantoms as a function of center frequency shift

We evaluated the performance of original and wideband AIR in phantoms (same as Experiment 2) as a function of center frequency shift (same setup as the *Frequency*

Bandwidth experiment; see 6.5 Supplementary Materials).

6.2.8 Experiment 4: Evaluation of accuracy in human subjects with ICD

Human imaging was conducted in accordance with protocols approved by our institutional Review Board and the Health Insurance Portability and Accountability Act; all subjects provided written informed consent.

We evaluated the performance of original and wideband AIR cardiac T_1 mapping pulse sequences in 11 human volunteers (10 males, 1 female, mean age = 30.0 ± 6.0 years) without prior history of heart disease. In each subject, we conducted T_1 mapping in 2-chamber and short-axis planes of the left ventricle, without administration of contrast agent (i.e., native T_1 mapping). To mimic image artifacts induced by ICD, we taped the ICD generator on each subject's left shoulder, approximately 5-10 cm superior to the left nipple, and performed original and wideband AIR cardiac T_1 mapping acquisitions. This mimicking approach (taping an ICD on left shoulder) was first established by Rashid et al. at 1.5T (27) and verified by our group at 3T (29). In human experiments, original AIR cardiac T_1 mapping without ICD was used as the control (see phantom results in Table 6.1 for justification).

In one male volunteer (age = 37), we performed native and post-contrast (15 and 35 min after administration of 0.15 mmol/kg of MultiHance) cardiac T_1 mapping in a 2-chamber plane of the left ventricle. This experiment was conducted to verify insensitivity to clinically relevant T_2. For each time point (baseline and 15 and 35 min after administration of MultiHance), we performed original and wideband AIR T_1 mapping with and without ICD, for a total of 4 AIR T_1 mapping acquisitions (original AIR,

original AIR with ICD, wideband AIR, and wideband AIR with ICD) per time point. For each time point, we first randomized the ICD presence, and then randomized the pulse sequence order. To further reduce the impact of contrast agent washout effects, we streamlined the protocol to perform 4 T_1 mapping acquisitions per time point in 1 min (including breathing instructions), while making sure to allow full magnetization recovery between acquisitions (i.e., wait time > 5 T_1s). To maintain the same ICD position throughout MRI at different time points, we drew the contour of the ICD on the volunteer's chest for repeatable taping and removal.

6.2.9 Image analysis

To achieve noise reduction during post-processing, which is important since low signal-to-noise ratio is expected with ultra-fast gradient echo readout and 10° flip angle, we applied a modified Hanning window to the k-space representation of each image. To estimate the blurring effects of the Hanning window, we calculated its point spread function (PSF) as the inverse Fourier transform of the window. We then calculated the FWHM with subpixel precision using linear interpolation. The resulting FWHM was 1.5 and 1.3 pixel in the frequency-encoding and phase-encoding directions, respectively. Note that FWHM of an ideal PSF is 1 pixel.

For calculation of T_1, the T_1-weighted image was divided by the corresponding PD image on a pixel-by-pixel basis, and the ratio was used to calculate T_1 based on the Bloch equation describing T_1 relaxation in ideal saturation-recovery, as previously described (30). For the phantom experiments, we generated a mask defining the phantom boundary based on intensity thresholding to remove the background and include only the whole

phantom. For cardiac data analysis, endo- and epi-cardial contours were manually drawn to segment the myocardium, and another region-of-interest (ROI) was drawn to encircle the LV cavity. Care was taken to avoid partial volume averaging for each contour tracing (see Figure 6.4). All image processing was conducted using customized software programmed in Matlab (R2009a, The MathWorks, Inc., Natick, MA).

6.2.10 Statistical analysis

For statistical analysis of human data from 11 subjects, for each measurement type (native blood, native myocardium) per cardiac plane (short-axis, 2-chamber view), the mean T_1 value within an ROI (blood or myocardium) was pooled and averaged over 11 subjects. For each measurement type per cardiac plane, a single-factor analysis of variance was used to compare the mean T_1 values between four groups (original AIR without ICD, original AIR with ICD, wideband AIR without ICD, and wideband AIR with ICD), and Bonferroni correction was used to compare the mean values between the control (original AIR without ICD) and other three groups (original AIR with ICD, wideband AIR without ICD, and wideband AIR with ICD). A $p < 0.05$ was considered to be significant. All statistical analyses were performed using the Analyse-it software (Analyse-it Software, Ltd., Leeds, United Kingdom).

6.3 Results

6.3.1 Experiment 1: Evaluation of sensitivity to ICD and intracardiac leads in phantom

Figure 6.3 shows coronal T_1 maps of a phantom with ICD taped on one side of the phantom as shown. A T_1 map acquired with original AIR without ICD is also shown as the reference. Original AIR with ICD yielded considerable image artifacts, whereas wideband AIR with ICD suppressed image artifacts in regions as shown. Figure 6.3 also shows the corresponding T_1 maps with intracardiac leads attached to the same location as ICD. Note that both original and wideband AIR were insensitive to intracardiac leads.

6.3.2 Experiment 2: Evaluation of accuracy in $MnCl_2$ phantoms with ICD

In 5 phantoms with different concentrations of $MnCl_2$, compared with the control T_1 values derived from IR-FSE without ICD, the corresponding T_1 values were considerably lower for original AIR with ICD, whereas the T_1 values were similar for wideband AIR with ICD. For completeness, see the corresponding T_1 results for original and wideband AIR and MOLLI without ICD (Table 6.1). We note that the standard deviation per phantom is considerably higher for original AIR with ICD than wideband AIR with ICD, implying higher sensitivity to ICD for original AIR.

6.3.3 Experiment 3: Evaluation of accuracy in $MnCl_2$ phantoms as a function of center frequency shift

Figure 6.2B shows plots of T_1 as a function of center frequency shift. Consistent with the frequency bandwidth experiment, wideband AIR produced consistent T_1 results over

8.9 kHz, whereas original AIR produced consistent T_1 results over 2.5 kHz.

6.3.4 Experiment 4: Evaluation of accuracy in human subjects with ICD

Figure 6.4 shows representative native T_1 maps in short-axis and long-axis planes of the heart of two different volunteers. Compared with original AIR without ICD as the control, original AIR with ICD produced less accurate T_1 results, whereas wideband AIR with ICD produced more accurate T_1 results. For completeness, see the corresponding T_1 results for original and wideband AIR without ICD (Table 6.S1 in 6.5 Supplementary Materials). We note that the standard deviation per ROI is considerably higher for original AIR with ICD than wideband AIR with ICD, implying higher sensitivity to ICD for original AIR.

Averaging the results over 11 human subjects, the mean myocardial and blood T_1 measurements were significantly different between the four groups (Table 6.2; $p < 0.001$). Compared with original AIR without ICD as the control, only original AIR with ICD was significantly different in both imaging planes ($p < 0.05$). We note that native T_1 measurements (myocardial T_1 ~ 1,100 ms; blood T_1 ~ 1,500 ms) made with original AIR without ICD and wideband AIR with and without ICD are comparable to ex-vivo (41) and in vivo (42) myocardial and blood T_1 measurements at 1.5T reported in literature.

Figure 6.5 shows native and post-contrast T_1 maps of another volunteer. Similar to the results shown in Figure 6.4 and data summarized in Table 6.1, compared with original AIR without ICD, original AIR with ICD produced less accurate T_1 results, whereas wideband AIR with ICD produced more accurate T_1 results. For completeness, see the corresponding T_1 results for original and wideband AIR without ICD (Table 6.S2 in 6.5

Supplementary Materials). Consistent with phantom and native cardiac T_1 results, the standard deviation per ROI is considerably higher for original AIR with ICD than wideband AIR with ICD, implying higher sensitivity to ICD for original AIR.

6.4 Discussion

This study demonstrates the feasibility of a wideband pulse sequence for cardiac T_1 mapping without significant image artifacts induced by ICD at 1.5T. In both phantom and human experiments, compared with control T_1 measurements without ICD, original AIR with ICD produced less accurate T_1 results, whereas wideband AIR with ICD produced more accurate T_1 results.

This study has several points that warrant discussion. First, to our knowledge, this is the first study reporting successful cardiac T_1 mapping without significant image artifacts induced by ICD. Future studies include evaluation of diffuse myocardial fibrosis burden in patients with ICD implantation. Second, in addition to the image artifacts that cause T_1 error, ICD may also cause severe image distortion, spatial shifts, and signal loss due to intravoxel dephasing, all of which may be a problem when registering different MR images which have different sensitivities. These effects can be minimized by using a readout with short echo time such as ultra-short TE pulse sequences. Third, compared with original AIR, wideband AIR deposits more energy per unit time (i.e., higher SAR). However, in the context of wideband AIR cardiac T_1 mapping (one PD image acquisition without saturation pulse and one T_1-weighted image acquisition with saturation pulse, each acquisition with TurboFLASH readout), we were able to perform wideband AIR safely; it produces whole-body SAR of 0.5 W/kg, which is 3-4 times lower than the safe

limits (1.5-2 W/kg) recommended by established pacemaker/ICD MRI protocols at 1.5T (25,26). Therefore, it is highly unlikely that wideband AIR will cause significant lead tip heating. Nevertheless, a future comprehensive study is warranted to measure RF-induced lead tip heating with wideband AIR, similar to (43,44). Fourth, this study did not test other investigational cardiac T_1 mapping pulse sequences in the presence of ICD. Other investigational cardiac T_1 mapping pulse sequences (MOLLI (39) and ShMOLLI (45) using a standard hyperbolic secant adiabatic inversion RF pulse; SASHA (42) and MLLSR (46) using a standard saturation pulse) are likely to be sensitive to ICD and produce inaccurate T_1 results, because the frequency bandwidth of the aforementioned RF pulse modules is not wide enough to handle the large center frequency shift induced by ICD. In addition, MOLLI, ShMOLLI, MLLSR, and SASHA all use b-SSFP, so the readout will also generate image artifacts induced by ICD. Therefore, we did not compare wideband AIR with MOLLI, ShMOLLI, MLLSR, and SASHA, since their wideband counterparts are currently unavailable. A head-to-head comparison between wideband AIR to wideband versions of MOLLI, ShMOLLI, MLLSR, and SASHA (which currently do not exist) is beyond the scope of this study. Fifth, we note that both original (FWHM = 2.5 kHz) and wideband (FWHM = 8.9 kHz) saturation pulse modules are insensitive to typical static magnetic field inhomogeneity in the heart at 1.5T (~ 100 Hz, largely due to the heart-lung interface and/or cardiac veins)(47). Sixth, while duration of the wideband pulse module is 151 ms, the total RF time is only 46 ms, whereas the remaining time is used to play crusher and spoiler magnetic field gradients. We note that in the context of saturation of magnetization, T_2 relaxation during the RF time is a benefit, whereas in the context of inversion of magnetization T_2 relaxation is a detriment. Therefore, BISTRO is

insensitive to T_2 in the context of saturation recovery of magnetization (see Table 6.1 and Figure 6.5).

This study has three limitations that warrant discussion. First, as a technical development work, we did not include patients with ICD implantation. A thorough investigation of safety and effectiveness in patients with ICD implantation is beyond the scope of this work. As such, we are unable to definitively claim that wideband AIR is insensitive to implanted ICD including intracardiac leads. Our phantom study (see Figure 6.3) shows that intra-cardiac leads do not produce significant image artifacts. Furthermore, our experience with LGE MRI (with a standard hyperbolic secant inversion pulse with frequency bandwidth ~ 1 kHz) in patients with ICDs suggests that the center frequency shift induced by intracardiac leads is not high enough to influence the efficacy of a standard hyperbolic secant inversion pulse. Our experience is consistent with wideband LGE MRI results reported by Rashid et al. (27). The mimicking approach (taping an ICD generator on the subject's left shoulder) was first established by Rashid et al. at 1.5T (27) and verified by our group at 3T (29). Thus, results from this study are likely to translate to patients with ICD implantation. Not testing the performance of wideband AIR cardiac T_1 mapping in patients with ICD implantation is a limitation of this study; on the other hand, the proposed study design, with original AIR T_1 mapping without ICD as the control, allows reference measurements and repeated measurements without safety concerns associated with lead tip heating. This technical development work may set the foundation for future studies aim at evaluating both the effectiveness and safety of wideband AIR cardiac T_1 mapping in patients with implanted cardiac devices. Second, in this study we used a protocol to produce nominal spatial resolution of

2.8 mm × 2.8 mm (4.2 mm × 3.6 mm accounting for the additional blurring caused by Hanning window), in order to compensate for low signal-to-noise ratio. Compared with 3-3-5 MOLLI, wideband AIR is expected to produce lower signal-to-noise ratio (see standard deviation values in Table 6.1) due to the following factors: b-SSFP (MOLLI) vs. TurboFLASH (wideband AIR), inversion recovery (MOLLI) vs. saturation recovery (wideband AIR), and 11 images (MOLLI) vs. 2 images (wideband AIR). The resolution used in this study will be sensitive to partial volume effects and introduce errors when quantifying T_1 from small myocardial lesions. Fortunately, the spatial resolution reported in this study may be adequate for quantifying diffuse cardiac fibrosis in patients with non-ischemic cardiomyopathy. Potential approaches to improve the spatial resolution include the use of dedicated cardiac coil array and image denoising with nonlinear iterative method such as non-local means (49). Third, this study included only one subject with contrast agent administration. Consistent with BISTRO characteristics (see 6.5 Supplementary Materials), our phantom study (see Table 6.1) shows that wideband saturation pulse module is insensitive to T_2. While both theoretical and in vitro results suggest insensitivity to T_2, additional human subjects with contrast agent administration need to be examined to verify that wideband is insensitive to clinically relevant T_2.

In summary, this study demonstrates the feasibility of wideband AIR pulse sequence for cardiac T_1 mapping without significant image artifacts induced by ICD. A future study of a high number of patients with ICD implantation is warranted to evaluate the clinical utility of wideband AIR cardiac T_1 mapping for assessment of myocardial fibrosis burden without image artifacts induced by ICD. This new cardiac-device-insensitive MRI pulse sequence may have a broad impact on cardiac imaging, because it

has the potential to activate new clinical studies aimed at advancing other cardiac devices such as biventricular pacemaker.

6.5 Supplementary Materials

6.5.1 BISTRO implementation details

We implemented BISTRO as a train of 15 hyperbolic secant adiabatic inversion RF pulses, with crusher gradients in between RF pulses to minimize stimulated echoes, and spoiler gradients before the first RF pulse and after the last RF pulse to dephase the transverse magnetization (see Figure 6.1). We decreased the duration from the first to last set of crusher gradients to suppress stimulated echoes. The total duration, including crusher and spoiler gradients, was 151 ms. Each hyperbolic secant inversion pulse (frequency modulation parameter β = 750 radians/s, phase modulation parameter μ= 10 [dimensionless]) was 3.07 ms long and its nominal transmit B_1+ (normalized by gyromagnetic ratio) calibrated by the transmit body coil was 926 Hz. The number of pulses and nominal B_1+ (i.e., amplitude) for each pulse were empirically determined in a preliminary phantom experiment, where we systematically adjusted the number of RF pulses and nominal B_1+ to consistently achieve effective saturation of magnetization (i.e., residual M_z immediately after the last RF pulse in the module is less than 5% of equilibrium magnetization (M_0)).

6.5.2 Calculation of frequency bandwidth of the saturation pulse modules

We determined empirically, in a phantom positioned near magnet isocenter, the frequency bandwidth of the original and wideband saturation modules. Using the

approach described in (31,48,50), we quantified the residual M_z immediately after the saturation pulse module, by normalizing the saturation-no-recovery image (i.e., TD = 3 ms, which is the duration of the spoiler gradients) with the PD image (i.e., M_0) and calculating the residual M_z as a fraction of M_0 (0 to 1). Note that residual M_z of 0 corresponds to complete saturation of magnetization, whereas residual M_z of 1 corresponds to no rotation. The experiment was repeated by adjusting the center frequency offset of the saturation pulse module from -6 to 6 kHz (variable steps). We then plotted the residual M_z (as a fraction of M_0) as a function of center frequency shift to calculate the FWHM, which is by definition the frequency bandwidth of the saturation pulse module. As shown in Figure 6.2, the residual M_z curve for original saturation pulse module had side lobes. This observation is consistent with the fact that original saturation pulse module is comprised of 3 rectangular RF pulses (i.e., Fourier transform of a rectangular function is a sinc; see Figure 6.2).

6.5.3 Supporting information

See Table 6.S1.

See Table 6.S2.

See Figure 6.S1.

6.6 Clinical Testing in Patients with a Defibrillator

As a follow-up to the development of the wideband AIR cardiac T_1 mapping pulse sequence, we tested its performance in several patients with implantable defibrillators. Figure 6.6 shows two representative cases which compare the original and wideband AIR

post-contrast T_1 maps, where wideband AIR produced considerably lower image artifacts than original AIR.

6.7 References

1. Go AS, Mozaffarian D, Roger VL, Benjamin EJ, Berry JD, Borden WB, Bravata DM, Dai S, Ford ES, Fox CS, Franco S, Fullerton HJ, Gillespie C, Hailpern SM, Heit JA, Howard VJ, Huffman MD, Kissela BM, Kittner SJ, Lackland DT, Lichtman JH, Lisabeth LD, Magid D, Marcus GM, Marelli A, Matchar DB, McGuire DK, Mohler ER, Moy CS, Mussolino ME, Nichol G, Paynter NP, Schreiner PJ, Sorlie PD, Stein J, Turan TN, Virani SS, Wong ND, Woo D, Turner MB. Heart disease and stroke statistics--2013 update: a report from the American Heart Association. Circulation 2013;127(1):e6-e245.

2. Yancy CW, Jessup M, Bozkurt B, Butler J, Casey DE, Drazner MH, Fonarow GC, Geraci SA, Horwich T, Januzzi JL, Johnson MR, Kasper EK, Levy WC, Masoudi FA, McBride PE, McMurray JJV, Mitchell JE, Peterson PN, Riegel B, Sam F, Stevenson LW, Tang WHW, Tsai EJ, Wilkoff BL. 2013 ACCF/AHA guideline for the management of heart failure: a report of the American College of Cardiology Foundation/American Heart Association Task Force on practice guidelines. J Am Coll Cardiol 2013;62(16):e147-e239.

3. Simmons A, Tofts PS, Barker GJ, Arridge SR. Sources of intensity nonuniformity in spin echo images at 1.5 T. Magn Reson Med 1994;32(1):121-128.

4. Greenman RL, Shirosky JE, Mulkern RV, Rofsky NM. Double inversion black-blood fast spin-echo imaging of the human heart: a comparison between 1.5T and 3.0T. JMRI 2003;17(6):648-655.

5. Hunt SA, Abraham WT, Chin MH, Feldman AM, Francis GS, Ganiats TG, Jessup M, Konstam MA, Mancini DM, Michl K, Oates JA, Rahko PS, Silver MA, Stevenson LW, Yancy CW. 2009 Focused update incorporated into the ACC/AHA 2005 Guidelines for the Diagnosis and Management of Heart Failure in Adults A Report of the American College of Cardiology Foundation/American Heart Association Task Force on Practice Guidelines Developed in Collaboration With the International Society for Heart and Lung Transplantation. J Am Coll Cardiol 2009;53(15):e1-e90.

6. Mann DL, Barger PM, Burkhoff D. Myocardial recovery and the failing heart: myth, magic, or molecular target? J Am Coll Cardiol 2012;60(24):2465-2472.

7. Taylor DO, Edwards LB, Aurora P, Christie JD, Dobbels F, Kirk R, Rahmel AO, Kucheryavaya AY, Hertz MI. Registry of the International Society for Heart and

Lung Transplantation: twenty-fifth official adult heart transplant report--2008. The Journal of Heart and Lung Transplantation 2008;27(9):943-956.

8. Zafeiridis A, Jeevanandam V, Houser SR, Margulies KB. Regression of cellular hypertrophy after left ventricular assist device support. Circulation 1998;98(7):656-662.

9. Slaughter MS, Rogers JG, Milano CA, Russell SD, Conte JV, Feldman D, Sun B, Tatooles AJ, Delgado RM, 3rd, Long JW, Wozniak TC, Ghumman W, Farrar DJ, Frazier OH. Advanced heart failure treated with continuous-flow left ventricular assist device. N Engl J Med 2009;361(23):2241-2251.

10. Russo MJ, Hong KN, Davies RR, Chen JM, Sorabella RA, Ascheim DD, Williams MR, Gelijns AC, Stewart AS, Argenziano M, Naka Y. Posttransplant survival is not diminished in heart transplant recipients bridged with implantable left ventricular assist devices. J Thorac Cardiovasc Surg 2009;138(6):1425-1432 e1421-1423.

11. Miller LW, Pagani FD, Russell SD, John R, Boyle AJ, Aaronson KD, Conte JV, Naka Y, Mancini D, Delgado RM, MacGillivray TE, Farrar DJ, Frazier OH. Use of a continuous-flow device in patients awaiting heart transplantation. N Engl J Med 2007;357(9):885-896.

12. Rose EA, Gelijns AC, Moskowitz AJ, Heitjan DF, Stevenson LW, Dembitsky W, Long JW, Ascheim DD, Tierney AR, Levitan RG, Watson JT, Meier P, Ronan NS, Shapiro PA, Lazar RM, Miller LW, Gupta L, Frazier OH, Desvigne-Nickens P, Oz MC, Poirier VL. Long-term use of a left ventricular assist device for end-stage heart failure. N Engl J Med 2001;345(20):1435-1443.

13. Holman WL, Kormos RL, Naftel DC, Miller MA, Pagani FD, Blume E, Cleeton T, Koenig SC, Edwards L, Kirklin JK. Predictors of death and transplant in patients with a mechanical circulatory support device: a multi-institutional study. The Journal of Heart and Lung Transplantation 2009;28(1):44-50.

14. Kim RJ, Wu E, Rafael A, Chen EL, Parker MA, Simonetti O, Klocke FJ, Bonow RO, Judd RM. The use of contrast-enhanced magnetic resonance imaging to identify reversible myocardial dysfunction. N Engl J Med 2000;343(20):1445-1453.

15. Kramer CM, Chandrashekhar Y, Narula J. T1 mapping by CMR in cardiomyopathy: a noninvasive myocardial biopsy? JACC Cardiovascular Imaging 2013;6(4):532-534.

16. Iles L, Pfluger H, Phrommintikul A, Cherayath J, Aksit P, Gupta SN, Kaye DM, Taylor AJ. Evaluation of diffuse myocardial fibrosis in heart failure with cardiac magnetic resonance contrast-enhanced T1 mapping. J Am Coll Cardiol

2008;52(19):1574-1580.

17. Sibley CT, Noureldin RA, Gai N, Nacif MS, Liu S, Turkbey EB, Mudd JO, van der Geest RJ, Lima JA, Halushka MK, Bluemke DA. T1 Mapping in cardiomyopathy at cardiac MR: comparison with endomyocardial biopsy. Radiology 2012;265(3):724-732.

18. Miller CA, Naish JH, Bishop P, Coutts G, Clark D, Zhao S, Ray SG, Yonan N, Williams SG, Flett AS, Moon JC, Greiser A, Parker GJ, Schmitt M. Comprehensive validation of cardiovascular magnetic resonance techniques for the assessment of myocardial extracellular volume. Circ Cardiovasc Imaging 2013;6(3):373-383.

19. Flett AS, Hayward MP, Ashworth MT, Hansen MS, Taylor AM, Elliott PM, McGregor C, Moon JC. Equilibrium contrast cardiovascular magnetic resonance for the measurement of diffuse myocardial fibrosis: preliminary validation in humans. Circulation 2010;122(2):138-144.

20. Kehr E, Sono M, Chugh SS, Jerosch-Herold M. Gadolinium-enhanced magnetic resonance imaging for detection and quantification of fibrosis in human myocardium in vitro. Int J Cardiovasc Imaging 2008;24(1):61-68.

21. Jerosch-Herold M, Sheridan DC, Kushner JD, Nauman D, Burgess D, Dutton D, Alharethi R, Li D, Hershberger RE. Cardiac magnetic resonance imaging of myocardial contrast uptake and blood flow in patients affected with idiopathic or familial dilated cardiomyopathy. American Journal of Physiology Heart and Circulatory Physiology 2008;295(3):H1234-H1242.

22. White SK, Sado DM, Fontana M, Banypersad SM, Maestrini V, Flett AS, Piechnik SK, Robson MD, Hausenloy DJ, Sheikh AM, Hawkins PN, Moon JC. T1 mapping for myocardial extracellular volume measurement by CMR: bolus only versus primed infusion technique. JACC Cardiovascular Imaging 2013;6(9):955-962.

23. Arheden H, Saeed M, Higgins CB, Gao DW, Bremerich J, Wyttenbach R, Dae MW, Wendland MF. Measurement of the distribution volume of gadopentetate dimeglumine at echo-planar MR imaging to quantify myocardial infarction: comparison with 99mTc-DTPA autoradiography in rats. Radiology 1999;211(3):698-708.

24. Moon JC, Messroghli DR, Kellman P, Piechnik SK, Robson MD, Ugander M, Gatehouse PD, Arai AE, Friedrich MG, Neubauer S, Schulz-Menger J, Schelbert EB. Myocardial T1 mapping and extracellular volume quantification: a Society for Cardiovascular Magnetic Resonance (SCMR) and CMR Working Group of the European Society of Cardiology consensus statement. J Cardiovasc Magn Reson 2013;15(1):92.

25. Sommer T, Naehle CP, Yang A, Zeijlemaker V, Hackenbroch M, Schmiedel A, Meyer C, Strach K, Skowasch D, Vahlhaus C, Litt H, Schild H. Strategy for safe performance of extrathoracic magnetic resonance imaging at 1.5 tesla in the presence of cardiac pacemakers in non-pacemaker-dependent patients: a prospective study with 115 examinations. Circulation 2006;114(12):1285-1292.

26. Nazarian S, Roguin A, Zviman MM, Lardo AC, Dickfeld TL, Calkins H, Weiss RG, Berger RD, Bluemke DA, Halperin HR. Clinical utility and safety of a protocol for noncardiac and cardiac magnetic resonance imaging of patients with permanent pacemakers and implantable-cardioverter defibrillators at 1.5 tesla. Circulation 2006;114(12):1277-1284.

27. Rashid S, Rapacchi S, Vaseghi M, Tung R, Shivkumar K, Finn JP, Hu P. Improved late gadolinium enhancement MR imaging for patients with implanted cardiac devices. Radiology 2014;270(1):269-274.

28. Stevens SM, Tung R, Rashid S, Gima J, Cote S, Pavez G, Khan S, Ennis DB, Finn JP, Boyle N, Shivkumar K, Hu P. Device artifact reduction for magnetic resonance imaging of patients with implantable cardioverter-defibrillators and ventricular tachycardia: late gadolinium enhancement correlation with electroanatomic mapping. Heart Rhythm 2014;11(2):289-298.

29. Ranjan R, McGann CJ, Jeong EK, Hong K, Kholmovski EG, Blauer J, Wilson BD, Marrouche NF, Kim D. Wideband late gadolinium enhanced magnetic resonance imaging for imaging myocardial scar without image artefacts induced by implantable cardioverter-defibrillator: a feasibility study at 3 T. Europace 2014.

30. Fitts M, Breton E, Kholmovski EG, Dosdall DJ, Vijayakumar S, Hong KP, Ranjan R, Marrouche NF, Axel L, Kim D. Arrhythmia insensitive rapid cardiac T1 mapping pulse sequence. Magn Reson Med 2013;70(5):1274-1282.

31. Kim D, Oesingmann N, McGorty K. Hybrid adiabatic-rectangular pulse train for effective saturation of magnetization within the whole heart at 3 T. Magn Reson Med 2009;62(6):1368-1378.

.

32. Luo Y, de Graaf RA, DelaBarre L, Tannus A, Garwood M. BISTRO: an outer-volume suppression method that tolerates RF field inhomogeneity. Magn Reson Med 2001;45(6):1095-1102.

33. Kellman P, Herzka DA, Hansen MS. Adiabatic inversion pulses for myocardial T1 mapping. Magn Reson Med 2014;71(4):1428-1434.

34. Griswold MA, Jakob PM, Heidemann RM, Nittka M, Jellus V, Wang J, Kiefer B, Haase A. Generalized autocalibrating partially parallel acquisitions (GRAPPA).

Magn Reson Med 2002;47(6):1202-1210.

35. Breton E, Kim D, Chung S, Axel L. Quantitative contrast-enhanced first-pass cardiac perfusion MRI at 3 tesla with accurate arterial input function and myocardial wall enhancement. JMRI 2011;34(3):676-684.

36. Chung S, Kim D, Breton E, Axel L. Rapid B1+ mapping using a preconditioning RF pulse with TurboFLASH readout. Magn Reson Med 2010;64(2):439-446.

37. Costantini M. A novel phase unwrapping method based on network programming. IEEE Transactions on Geoscience and Remote Sensing 1998;36(3):813-821.

38. Ulmer JL, Mathews VP, Hamilton CA, Elster AD, Moran PR. Magnetization transfer or spin-lock? An investigation of off-resonance saturation pulse imaging with varying frequency offsets. American Journal of Neuroradiology 1996;17(5):805-819.

39. Messroghli DR, Radjenovic A, Kozerke S, Higgins DM, Sivananthan MU, Ridgway JP. Modified Look-Locker inversion recovery (MOLLI) for high-resolution T1 mapping of the heart. Magn Reson Med 2004;52(1):141-146.

40. Kim D, Jensen JH, Wu EX, Sheth SS, Brittenham GM. Breathhold multiecho fast spin-echo pulse sequence for accurate R2 measurement in the heart and liver. Magn Reson Med 2009;62(2):300-306.

41. Stanisz GJ, Odrobina EE, Pun J, Escaravage M, Graham SJ, Bronskill MJ, Henkelman RM. T1, T2 relaxation and magnetization transfer in tissue at 3T. Magn Reson Med 2005;54(3):507-512.

42. Chow K, Flewitt JA, Green JD, Pagano JJ, Friedrich MG, Thompson RB. Saturation recovery single-shot acquisition (SASHA) for myocardial T(1) mapping. Magn Reson Med 2014;71(6):2082-2095.

43. Buckland JR, Huntley JM, Turner SRE. Unwrapping noisy phase maps by use of a minimum-cost-matching algorithm. Appl Opt 1995;34(23):5100-5108.

44. Nordbeck P, Fidler F, Friedrich MT, Weiss I, Warmuth M, Gensler D, Herold V, Geistert W, Jakob PM, Ertl G, Ritter O, Ladd ME, Bauer WR, Quick HH. Reducing RF-related heating of cardiac pacemaker leads in MRI: implementation and experimental verification of practical design changes. Magn Reson Med 2012;68(6):1963-1972.

45. Piechnik SK, Ferreira VM, Dall'Armellina E, Cochlin LE, Greiser A, Neubauer S, Robson MD. Shortened Modified Look-Locker Inversion recovery (ShMOLLI) for clinical myocardial T1-mapping at 1.5 and 3 T within a 9 heartbeat breathhold. J Cardiovasc Magn Reson 2010;12:69.

46. Song T, Stainsby JA, Ho VB, Hood MN, Slavin GS. Flexible cardiac T1 mapping using a modified Look-Locker acquisition with saturation recovery. Magn Reson Med 2012;67(3):622-627.

47. Reeder SB, Faranesh AZ, Boxerman JL, McVeigh ER. In vivo measurement of T*2 and field inhomogeneity maps in the human heart at 1.5 T. Magn Reson Med 1998;39(6):988-998.

48. Kim D, Cernicanu A, Axel L. B(0) and B(1)-insensitive uniform T(1)-weighting for quantitative, first-pass myocardial perfusion magnetic resonance imaging. Magn Reson Med 2005;54(6):1423-1429.

49. Coupe P, Yger P, Barillot C. Fast non local means denoising for 3D MR images. MICCAI International Conference on Medical Image Computing and Computer-Assisted Intervention 2006;9(Pt 2):33-40.

50. Kim D, Gonen O, Oesingmann N, Axel L. Comparison of the effectiveness of saturation pulses in the heart at 3T. Magn Reson Med 2008;59(1):209-215.

Table 6.1. Summary of T_1 measurements of five $MnCl_2$ phantoms representing native myocardium (1,174 ms) and blood (1,550 ms) and post-contrast (500, 549, and 755 ms) blood/tissue T_1 values. Values represent mean ± standard deviation within an ROI. Percent error (relative to IR-FSE without ICD) is reported in parenthesis. Note that the standard deviation within an ROI is larger for original AIR with ICD than the other three AIR acquisitions (original AIR without ICD, wideband AIR without ICD, and wideband AIR with ICD).

$MnCl_2$ (mM)	T_2 (ms)	IR-FSE (ms)	3-3-5 MOLLI (ms)	Original AIR (ms)	Wideband AIR (ms)	Original AIR with ICD (ms)	Wideband AIR with ICD (ms)
0.036	294	1550 ± 20	1503 ± 13 (-3.1%)	1525 ± 78 (-1.7%)	1493 ± 79 (-3.7%)	743 ± 265 (-52.1%)	1546 ± 88 (-0.3%)
0.063	184	1174 ± 15	1160 ± 10 (-1.2%)	1197 ± 52 (1.9%)	1158 ± 59 (-1.3%)	643 ± 198 (-45.2%)	1142 ± 55 (-2.8%)
0.120	101	755 ± 11	761 ± 9 (0.8%)	752 ± 31 (-0.4%)	740 ± 27 (-2.0%)	479 ± 120 (-36.6%)	760 ± 29 (0.6%)
0.183	69	549 ± 9	545 ± 13 (-0.8%)	547 ± 25 (-0.5%)	525 ± 26 (-4.4%)	385 ± 83 (-30.0%)	551 ± 25 (0.2%)
0.200	62	500 ± 7	497 ± 6 (-0.5%)	495 ± 23 (-1.0%)	479 ± 20 (-4.1%)	355 ± 65 (-29.0%)	475 ± 24 (-4.9%)

Table 6.2. Summary of mean myocardial and blood T_1 measurements over 11 human subjects. These T_1 measurements were made with original AIR without ICD, wideband AIR without ICD, original AIR with ICD, and wideband AIR with ICD. Values represent mean ± standard deviation over 11 subjects. Percent error (relative to original AIR without ICD) is reported in parenthesis. Myocardial T_1 was significantly ($p < 0.001$) different between four acquisitions in 2-chamber and short-axis planes. Compared with original AIR without ICD as the control, only original AIR with ICD was significantly different in both imaging planes ($p < 0.05$). The same trends were observed for blood T_1 (ANOVA; $p < 0.001$), where only original AIR with ICD was significantly different from original AIR without ICD in both imaging planes ($p < 0.05$). We regret that the Analyse-it software does not report the adjusted p values for the Bonferroni paired-wise test. 2-CH: 2-chamber view; SAX: short-axis view.
*$p < 0.05$ with respect to original AIR without ICD as the control.

Tissue Type	Original (ms)	Wideband (ms)	Original with ICD (ms)	Wideband with ICD (ms)
2-CH, Myocardium	1093.6 ± 42.1	1158.8 ± 44.5 (6.0%)	*884.8 ± 84.8 (-19.1%)	1114.9 ± 68.8 (2.0%)
SAX, Myocardium	1069.8 ± 29.3	1137.7 ± 28.6 (6.4%)	*837.9 ± 115.8 (-21.7%)	1091.4 ± 82.7 (2.0%)
2-CH, Blood	1470.0 ± 75.3	1498.3 ± 57.6 (1.9%)	*1321.6 ± 124.7 (-10.1%)	1489.7 ± 60.8 (1.3%)
SAX, Blood	1473.9 ± 89.2	1522.5 ± 52.3 (3.3%)	*1241.0 ± 268.9 (-15.8%)	1496.6 ± 58.3 (1.5%)

Table 6.S1. Summary of myocardial and blood T_1 measured by original AIR without ICD, wideband AIR without ICD, original AIR with ICD, and wideband AIR with ICD, for two representative volunteers shown in Figure 6.4. V1: volunteer 1; V2: volunteer 2; 2-CH: 2-chamber view; SAX: short-axis view. Values represent mean ± standard deviation within ROI. Percent error (relative to original AIR without ICD) is reported in parenthesis. Note that the standard deviation is larger for original AIR with ICD than the other three AIR acquisitions.

Tissue Type	Original (ms)	Wideband (ms)	Original with ICD (ms)	Wideband with ICD (ms)
V1, 2-CH myocardium	1131.1 ± 94.0	1170.0 ± 102.5 (3.4%)	931.5 ± 249.0 (-17.6%)	1115.0 ± 153.4 (-1.4%)
V1, SAX myocardium	1114.0 ± 67.5	1131.9 ± 63.3 (1.6%)	838.6 ± 262.3 (-24.7%)	1093.6 ± 66.6 (-1.8%)
V1, 2-CH blood	1514.9 ± 89.6	1471.4 ± 79.9 (-2.9%)	1424.6 ± 132.9 (-6.0%)	1466.3 ± 100.4 (-3.2%)
V1, SAX blood	1533.8 ± 86.6	1508.0 ± 65.8 (-1.7%)	1322.3 ± 205.0 (-13.8%)	1467.4 ± 94.7 (-4.3%)
V2, 2-CH myocardium	1094.2 ± 100.7	1173.6 ± 132.1 (7.3%)	769.6 ± 302.2 (-29.7%)	1076.5 ± 156.5 (-1.6%)
V2, SAX myocardium	1113.2 ± 110.0	1120.7 ± 113.6 (0.7%)	634.5 ± 264.6 (-43.0%)	1137.2 ± 101.5 (2.2%)
V2, 2-CH blood	1499.3 ± 103.0	1501.4 ± 101.7 (0.1%)	1129.7 ± 283.2 (-24.6%)	1499.3 ± 113.8 (0.0%)
V2, SAX blood	1568.4 ± 95.9	1574.3 ± 67.7 (0.4%)	1290.3 ± 127.3 (-17.7%)	1541.6 ± 122.6 (-1.7%)

Table 6.S2. Summary of native and post-contrast myocardial and blood T_1 measurements of 1 volunteer (see Figure 6.5). These T_1 measurements were made by original AIR without ICD, wideband AIR without ICD, original AIR with ICD, and wideband AIR with ICD. Values represent mean ± standard deviation within ROI. Percent error (relative to original AIR without ICD) is reported in parenthesis. Note that the standard deviation is larger for original AIR with ICD than the other three AIR acquisitions.

Measurement Type	Original (ms)	Wideband (ms)	Original with ICD (ms)	Wideband with ICD (ms)
Native, myocardium	1101.4 ± 87.8	1174.9 ± 98.4 (6.7%)	950.7 ± 240.6 (-13.7%)	1156.2 ± 77.1 (5.0%)
15 min, myocardium	457.6 ± 35.6	456.9 ± 43.4 (-0.2%)	408.8 ± 72.5 (-10.7%)	455.8 ± 44.0 (-0.4%)
35 min, myocardium	511.5 ± 38.4	527.3 ± 33.8 (3.1%)	476.0 ± 80.8 (-6.9%)	520.7 ± 48.5 (1.8%)
Native, blood	1488.2 ± 102.2	1529.1 ± 100.8 (2.7%)	1336.5 ± 182.3 (-10.2%)	1498.0 ± 99.5 (0.7%)
15 min, blood	225.3 ± 34.7	212.8 ± 29.0 (-5.6%)	212.9 ± 39.3 (-5.5%)	219.9 ± 30.5 (-2.4%)
35 min, blood	295.5 ± 24.8	296.2 ± 28.9 (0.2%)	285.5 ± 31.7 (-3.4%)	293.9 ± 27.8 (-0.6%)

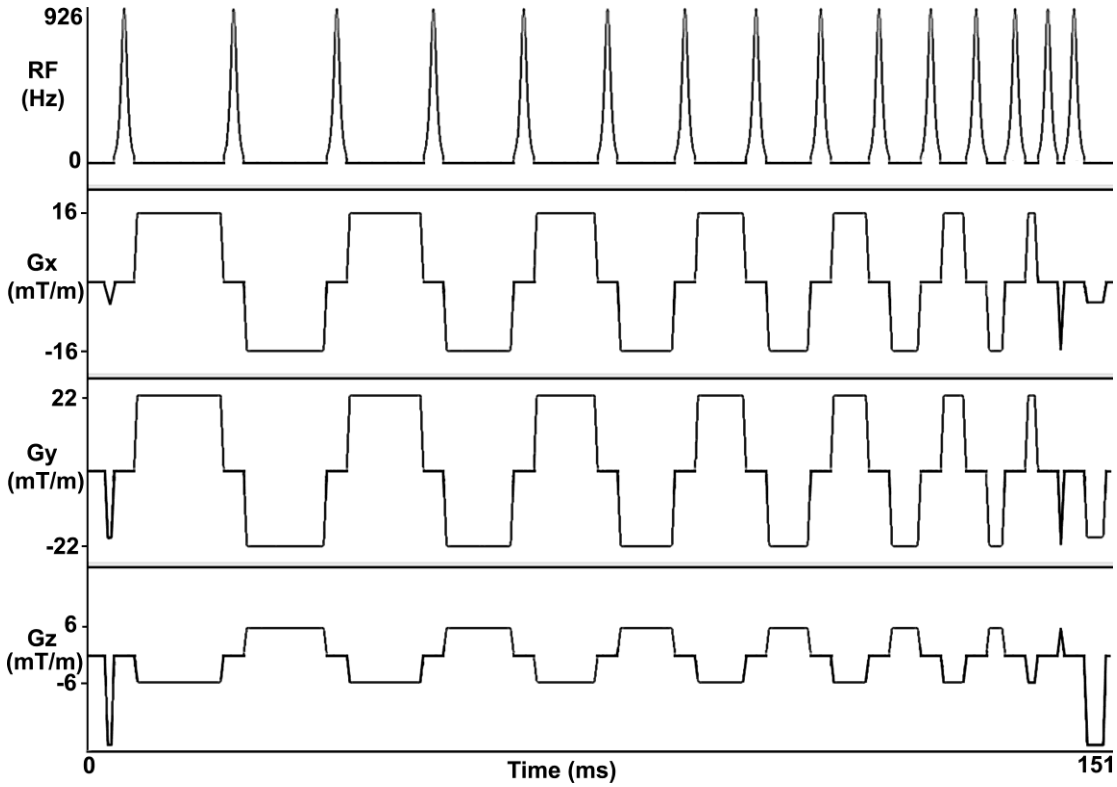

Figure 6.1. Pulse sequence diagram of a wideband saturation pulse module (BISTRO), which is comprised of 15 hyperbolic secant inversion RF pulses that do not meet the adiabatic condition on purpose. The spoiler gradients are applied before the first RF pulse and after the last RF pulse to dephase the transverse magnetization. The crusher gradients in between RF pulses are played to minimize stimulated echoes. While duration of the wideband saturation pulse module is 151 ms, the total RF time is only 46.05 ms, whereas the remaining time is used to play crusher and spoiler magnetic field gradients. These diagrams are drawn to approximate proportions but not to exact scale. G_z: slice-select gradient; G_y: phase-encoding gradient; G_x: frequency-encoding gradient.

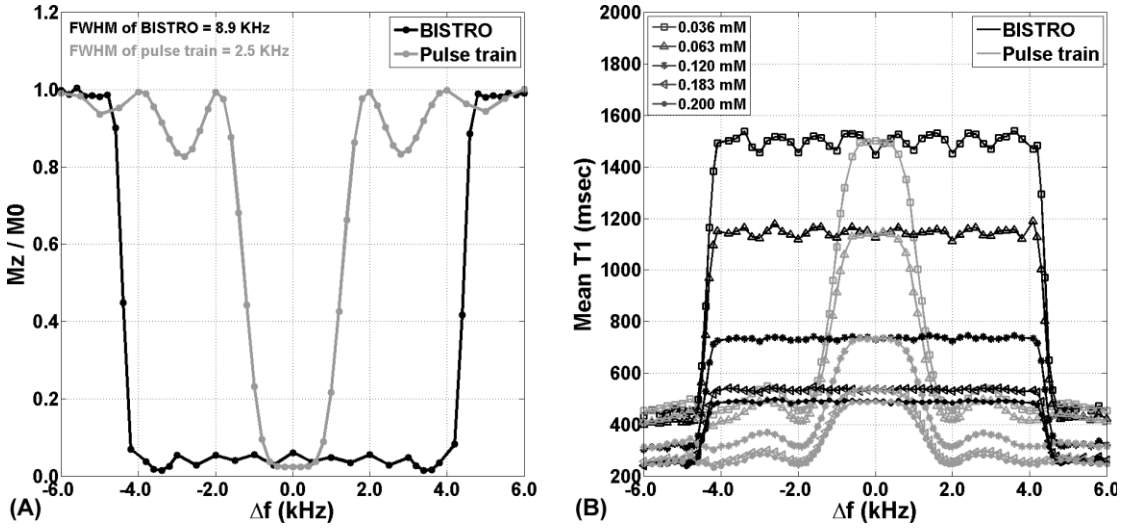

Figure 6.2. (A) Plots of residual M_z (as a fraction of M_0) as a function of center frequency shift. Note that residual M_z = 0 corresponds to complete saturation of magnetization, whereas residual M_z = 1 corresponds to no saturation. Compared with the original saturation pulse module (gray line), wideband pulse module (black line) had 256% higher frequency bandwidth (FWHM = 2.5 kHz and 8.9 kHz for original and wideband, respectively). Δf = center frequency shift. (B) Plots of T_1 as a function of center frequency shift. Consistent with the frequency bandwidth experiment, wideband AIR (black line) produced consistent T_1 results over 8.9 kHz, whereas original AIR (gray line) produced consistent T_1 results over 2.5 kHz.

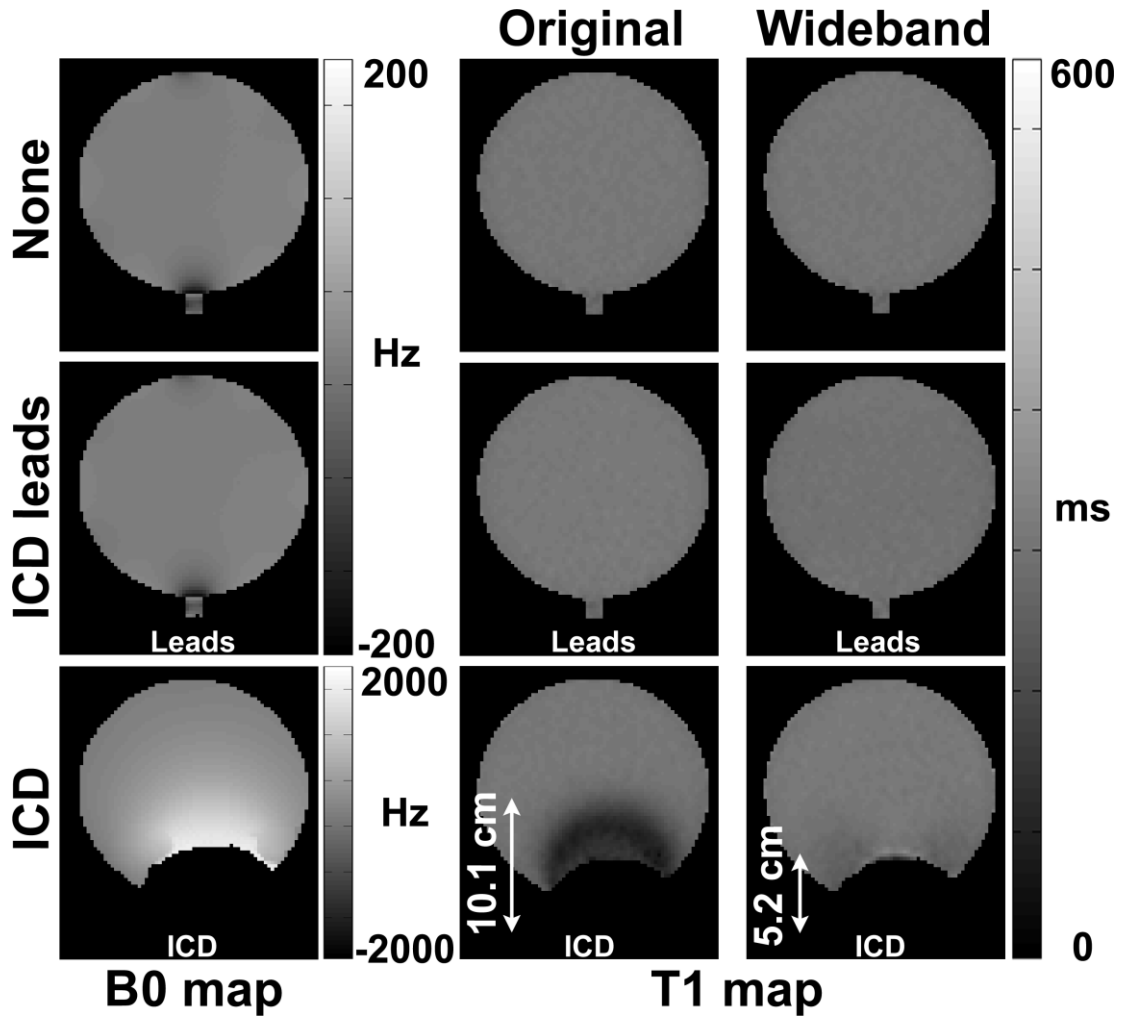

Figure 6.3. Coronal T_1 maps of a phantom acquired with original AIR (left column) and wideband AIR (right column): without anything taped (top row), with ICD leads (middle row), and with ICD taped on one side of the phantom as shown (bottom row). Arrows display the distance between ICD and outer boundary of the contaminated region.

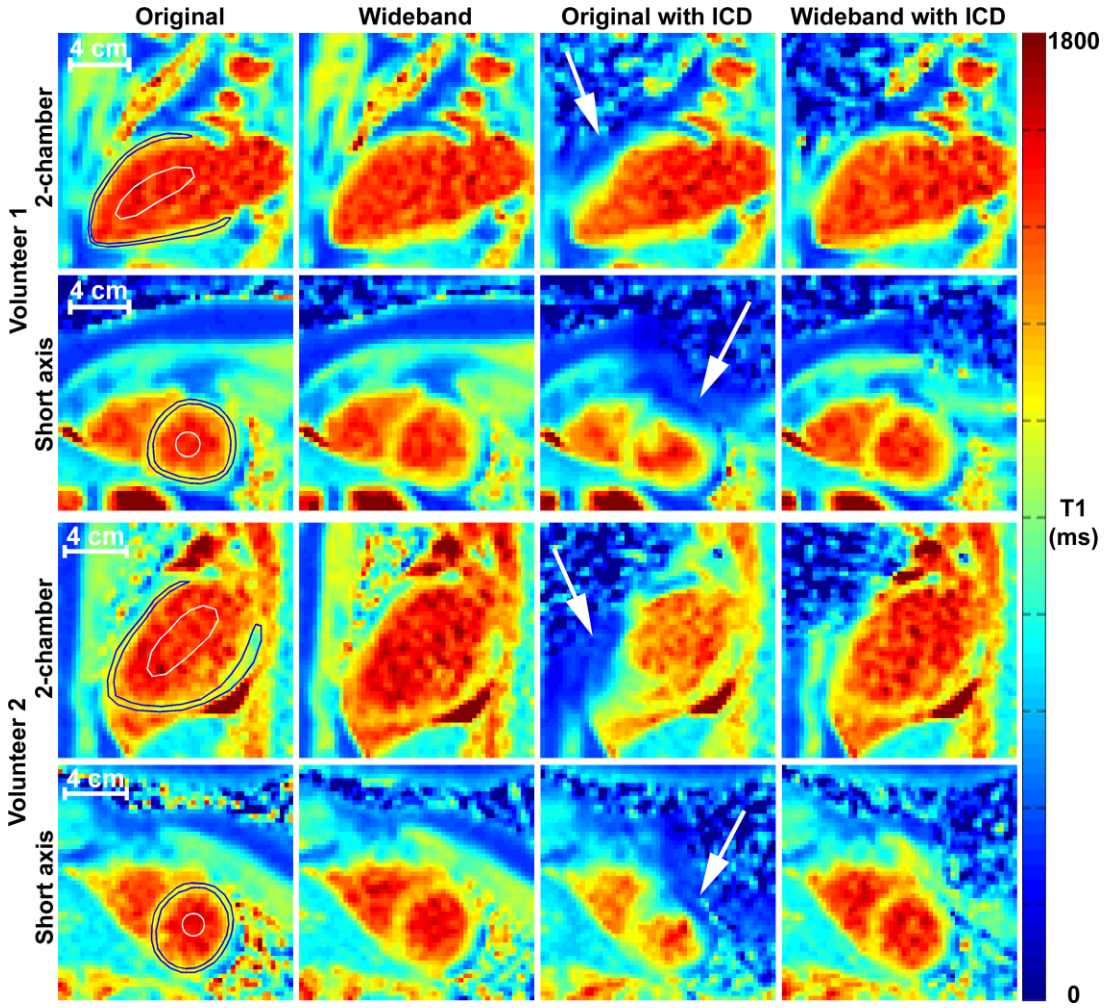

Figure 6.4. Representative native T_1 maps in short-axis (rows 2 and 4) and long-axis (rows 1 and 3) planes of the heart of two different volunteers with and without ICD taped on their left shoulder (~5-10 cm from the heart): original AIR without ICD (column 1), wideband AIR without ICD (column 2), original AIR with ICD (column 3), and wideband AIR with ICD (column 4). Compared with original AIR without ICD as the control, original AIR with ICD produced less accurate T_1 results, whereas wideband AIR with ICD produced more accurate T_1 results. White arrows point to cardiac regions compromised by ICD. Blood and cardiac contours superimposed on the left column only. See Table 6.S1 in 6.5 Supplementary Materials for the corresponding T_1 values.

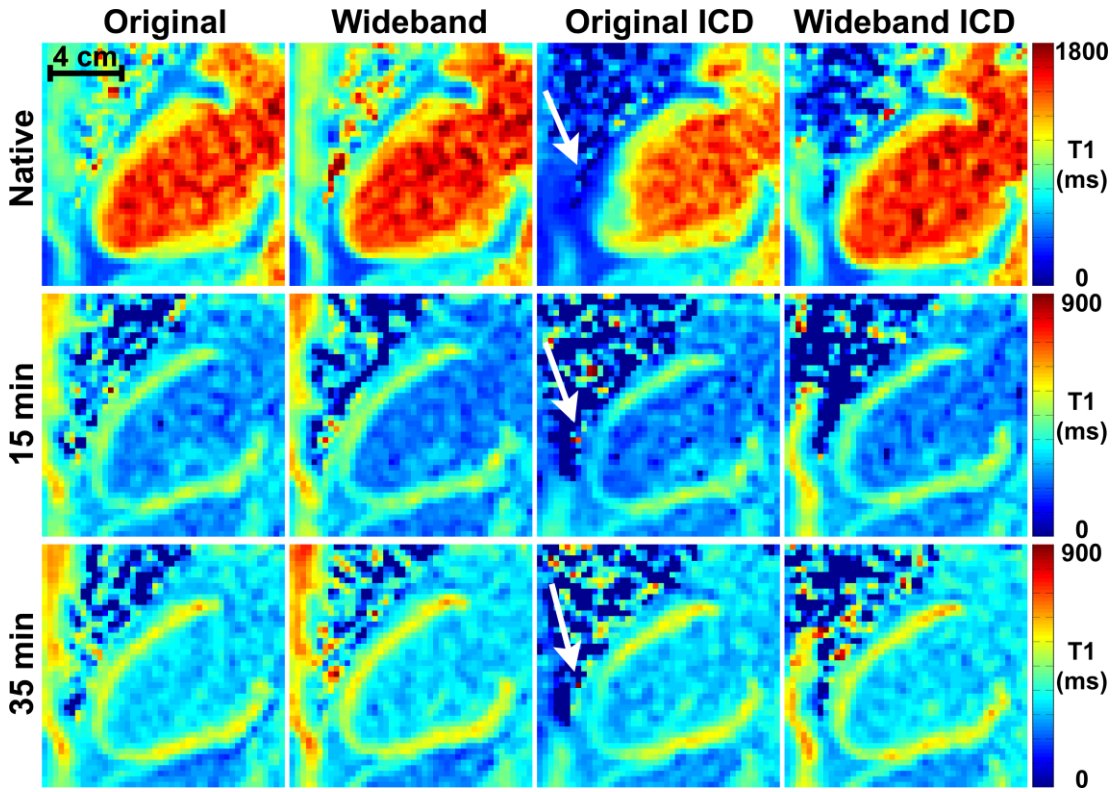

Figure 6.5. Representative native and post-contrast (15 and 35 min after MultiHance administration) T_1 maps in a 2-chamber plane of the heart acquired with and without ICD taped on his left shoulder (~5-10 cm from the heart): original AIR without ICD (column 1), wideband AIR without ICD (column 2), original AIR with ICD (column 3), and wideband AIR with ICD (column 4). Compared with original AIR without ICD as the control, original AIR with ICD produced less accurate T_1 results, whereas wideband AIR with ICD produced more accurate T_1 results. White arrows point to cardiac regions compromised by ICD. See Table 6.S2 in 6.5 Supplementary Materials for the corresponding T_1 values.

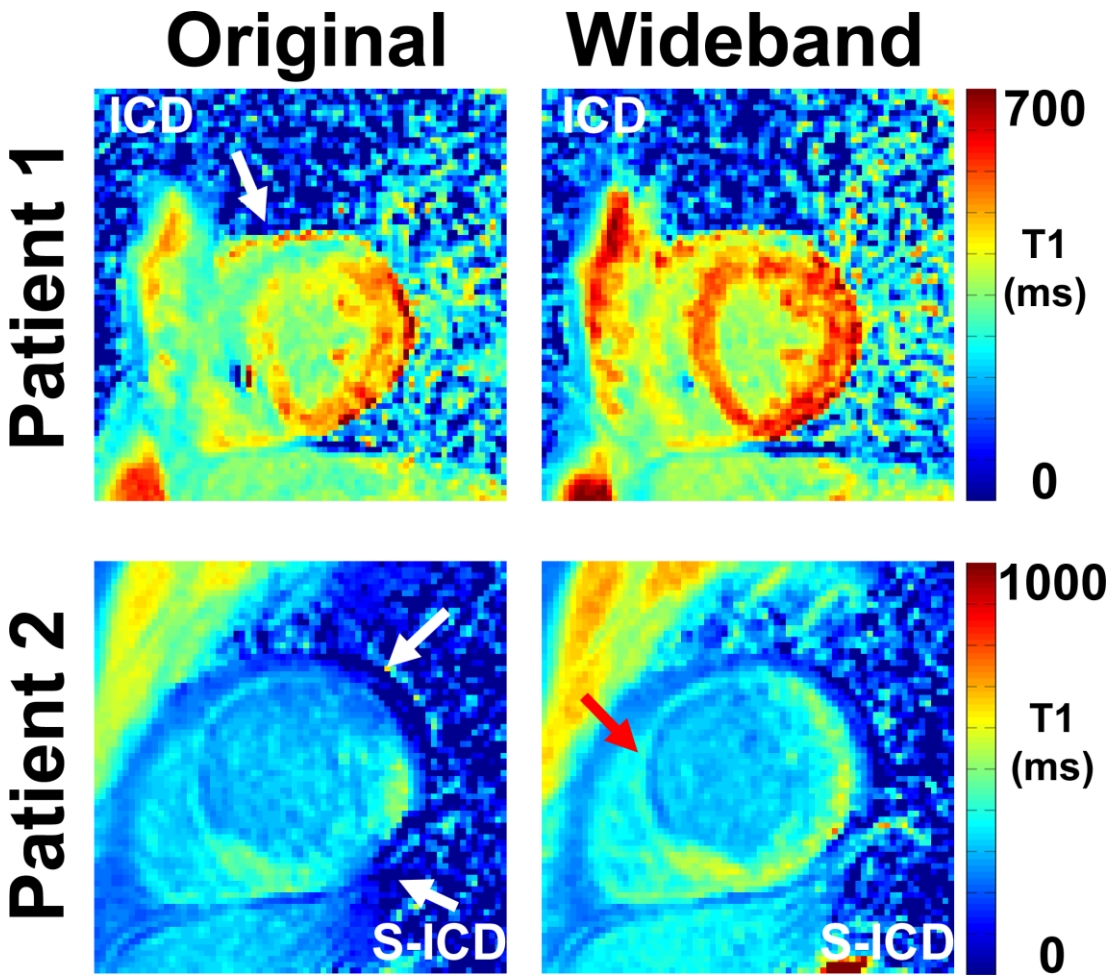

Figure 6.6. Original (left column) and wideband (right column) AIR post-contrast T_1 maps in patient 1 with an ICD (top row) and patient 2 with a subcutaneous ICD (S-ICD)(bottom row). White arrows point to image artifacts. Red arrow points to scar.

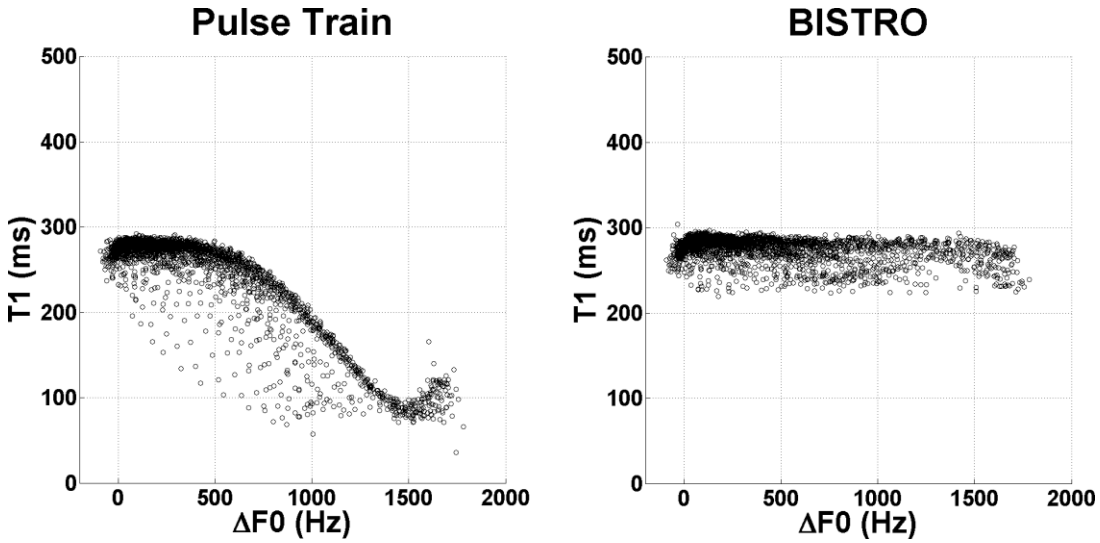

Figure 6.S1. Plots of T1 as a function of center frequency offset, corresponding to results shown in Figure 6.3: original AIR (left) and wideband AIR (right). Each point corresponds to a single pixel.

CHAPTER 7

CONCLUSION

This dissertation described advanced cardiac T_1 mapping pulse sequences for quantification of diffuse myocardial fibrosis in LVAD candidates. Our new methods addressed three major obstacles for successful MRI in LVAD candidates: arrhythmia, limited breath-hold capacity, and implantable defibrillators.

7.1 Summary of Work

Novel cardiac T_1 mapping methods have been developed and evaluated for quantification of diffuse myocardial fibrosis in LVAD candidates. First, to overcome arrhythmia and limited breath-hold capacity, an AIR cardiac T_1 mapping pulse sequence was developed (Chapter 3), validated against histology (Chapter 4), and compared with MOLLI (Chapter 5). Second, to overcome the challenge of suppressing image artifacts induced by implantable defibrillators, a wideband AIR cardiac T_1 mapping pulse sequence was developed and tested in healthy volunteers and patients with a device (Chapter 6).

7.2 Future Work

As part of Dr. Kim's research sponsored by the NIH (R01HL123003-01A1), we will continue to optimize AIR cardiac T_1 mapping beyond what is described in this dissertation. We will also take additional steps to examine whether pre-existing myocardial fibrosis predicts poor LV functional recovery following LVAD implantation.

First, we will develop a free-breathing method applicable to both the original and wideband AIR cardiac T_1 mapping pulse sequences. Leveraging the simple imaging strategy of the AIR method, one proton-density image and multiple T_1-weighted images can be consecutively acquired during a free-breathing examination, until good registration between them is achieved (1). In conjunction with the free-breathing method, image post-processing techniques such as diffeomorphic registration (2) can be used as a complementary approach (3).

Second, we will improve the reliability of the original and wideband AIR cardiac T_1 mapping pulse sequences. Through pulse sequence optimizations, these pulse sequences can achieve superior precision and performance. For example, "centric-pair" *k*-space ordering and high flip angles will improve precision in the AIR method and achieve similar repeatability as MOLLI (article in press (4)). Optimization of the wideband RF pulse will improve the homogeneity of the RF field and minimize SAR (5), improving the reliability of T_1 measurements with the wideband AIR method.

Third, we will investigate whether pre-existing myocardial fibrosis predicts poor LV functional recovery following LVAD-induced unloading. In each LVAD candidate with non-ischemic cardiomyopathy, we will conduct a CMR scan for quantification of pre-existing myocardial fibrosis and also measure the heart function as a baseline before

LVAD surgery. Six months after starting the LVAD-induced mechanical unloading (6), each patient will undergo a repeat test for measuring the heart function, in order to determine the degree of cardiac functional improvement compared to baseline. In addition, we will validate the wideband AIR cardiac T_1 mapping pulse sequence against histology, because the apical myocardium can be sampled during LVAD surgery.

7.3 References

1. DiBella E, Bassett E, Hong K, Adluru G, Likhite D, Suksaranjit P, Wilson B, McGann C, Kim D. Rapid ungated free-breathing cardiac MRI protocol. Program No 4578, Proc [Abstract] ISMRM 2015.

2. Avants BB, Epstein CL, Grossman M, Gee JC. Symmetric diffeomorphic image registration with cross-correlation: evaluating automated labeling of elderly and neurodegenerative brain. Med Image Anal 2008;12(1):26-41.

3. Hong K, Adluru G, Dibella E, Kim D. Ungated, free-breathing arrhythmia-insensitive-rapid (AIR) cardiac T1 mapping with motion corrected registration. Program No 4532, Proc [Abstract] ISMRM 2015.

4. Hong K, Collins J, Lee D, Wilcox J, Markl M, Carr J, Kim D. Optimized AIR and investigational MOLLI cardiac T1 mapping pulse sequences produce similar intra-scan repeatability in patients at 3T. NMR Biomed (in press).

5. Hong K, Kim D. Wideband Ccardiac MR perfusion pulse sequence for imaging patients with implantable cardioverter defibrillator. Program no 3133, Proc [Abstract] ISMRM 2016.

6. Drakos SG, Wever-Pinzon O, Selzman CH, Gilbert EM, Alharethi R, Reid BB, Saidi A, Diakos NA, Stoker S, Davis ES, Movsesian M, Li DY, Stehlik J, Kfoury AG. Magnitude and time course of changes induced by continuous-flow left ventricular assist device unloading in chronic heart failure: insights into cardiac recovery. J Am Coll Cardiol 2013;61(19):1985-1994.